TECHNISCHE
UNIVERSITÄT
WIEN
Vienna University of Technology

# MASTERARBEIT

# Toward a quantum switch for light

Ausgeführt am

Atominstitut

der Technischen Universität Wien

unter der Anleitung von

Univ. Prof. Dr. Arno Rauschenbeutel und Dr. Jürgen Volz

durch

Michael Scheucher

Zentagasse 28 / 7-8

1050 Wien

7.September 2013
Datum

Unterschrift

**Abstract**

This thesis describes the resent steps toward the realization of a quantum switch for light. In such a switch, the internal state of a quantum system, i.g. a single atom, routes the incoming light field into one of two possible output states. In our experiment this is realized in the regime of cavity quantum electrodynamics, by strongly coupling a single atom delivered by an atomic fountain to our bottle microresonator, a novel type of whispering-gallery-mode resonators. This atom-resonator system is interrogated by a tapered nanofiber in the vicinity of the evanescent field of the resonator. In this thesis a new atom-resonator examination scheme is developed, based on the fact that an atom coupled to a resonator significantly changes the polarization of the light transmitted by the coupling fiber. First measurements show that the presence of the atom rotates the polarization by 65° compared to the case when no atom couples. This demonstrates a first realization of an optical polarization switch controlled by a single atom. To implement quantum switching capability we have to perform coherent manipulations on the switch, i.e. the atom. For this purpose an ultrafast atomic state manipulation setup based on acousto-optical modulators was designed. This setup is capable of delivering light to the atom via the resonator on command with a delay of approximately 100 nanoseconds and at the same time provides an on/off extinction ratio of more than ten orders of magnitude, which is required by our experiment. The work presented in this thesis completes the tool set required for realizing and demonstrating the basic functionality of a quantum switch for light.

**Abstract**

(Deutsch)

Diese Arbeit beschreibt die unternommenen Schritte hin zur Realisierung eines quantenmechanischen Schalters für Licht. Ein solcher Apparat schaltet Licht zwischen zwei Ausgängen hin und her, in Abhängigkeit vom Zustand eines einzelnen Quantensystems, wir z.B. eines einzelnen Atoms. Die Realisierung eines solchen Schalters in unserem Experiment basiert auf der Resonator-Quantenelektrodynamik, wobei wir einzelne Atome, aus einem Springbrunnen, stark an einen Flüstergaleriemoden-Flaschenresonators koppeln. Mit Hilfe einer Nanofaser die an das evaneszente Feld des Resonators koppelt, können wir dabei auf das Atom-Resonator System zugreifen und dieses untersuchen. Im Rahmen dieser Arbeit wird eine neue Methode zur Untersuchung der Atom-Resonator-Wechselwirkung vorgestellt, welche darauf beruht, dass ein an den Resonator gekoppeltes Atom großen Einfluss auf die Polarisation des durch die Nanofaser transmittieren Lichts hat. Mit Hilfe dieses Effekts kann die Polarisation des Lichts das durch die Faser läuft gedreht werden. Erste Messungen zeigen eine Drehung der Polarisation um einen Winkle von 65° wenn ein Atom an den Resonator koppelt, im Vergleich zum Fall ohne Atom. Diese Ergebnisse demonstrieren die erste experimentelle Realisierung eines Polarisationsschalters, der von einem einzelnen Atom gesteuert wird. Um quantenmechanisches Schalten möglich zu machen, müssen wir den atomaren Zustand kontrollieren können. Dafür wurde ein Aufbau zur ultraschnellen Zustandsmanipulation, basierend auf akustooptische Modulatoren, entwickelt. Dieser schaltet Licht mit dem wir die Atome treiben wollen mit einer Verzögerung von nur einigen hundert Nanosekunden. Gleichzeitig weist das Setup eine hohe Unterdrückung des Lichts im ausgeschalteten Zustand auf, die benötigt wird weil wir Atome über die Resonator Moden treiben wollen. Mit den im Laufe dieser Arbeit entwickelten Komponenten steht nun alles für die Realisierung des quantenmechanischen Switch zur Verfügung.

# Contents

# Chapter 1

# Introduction

The nature of the interaction between light and matter was a central question from the early days of quantum mechanics onwards, culminating one of the most successful physical theories in history: quantum electrodynamics (QED). As predicted by this theory, the atom-light interaction can be changed drastically when introducing boundary conditions to the electromagnetic field. Already in 1946, Purcell predicted a change in the emission properties of an atom, when it is placed insight a resonator [1]. The latter can be realized by two mirrors which reflect the electromagnetic wave back and forth such that only certain modes can exist. The modification of the atom-light dynamics in a resonator is described in the frame-work of the fully quantized Jaynes Cummings model [2], where a single two level atom interacts with a single light mode. This model forms the foundations of cavity quantum electrodynamics (CQED). However, it is only in the last three decades that laboratory experiments have been able to realize this idealized example. The experimental investigation of this situation implies that all dissipative processes take place much slower than the dynamics of the coupled system. This regime is known as strong coupling, where already a single photon and/or a single atom in the resonator has a large impact on the dynamics of the system. The first experimental examination of CQED effects have been performed in the microwave regime using Rydberg atoms [3]. Due to the advances in experimental techniques and manufacturing processes, the non-classical phenomena of CQED can also be studied in the visible spectrum of light, using optical microresonators [4, 5].

In this field, where atoms are coupled to the light field of the resonator, high-finesse Fabry-Perot resonators have proven their value, enabling the investigation of fundamental physics [6, 7], as well as demonstrations of quantum information, computing and communication protocols [8, 9, 10]. However, the mirror losses in such resonators limit the in-out coupling efficiency of light to a few 10%. This restricts the applicability of such resonators in many cases to proof-of-principle demonstrations, because realistic applications require significantly higher in- and out-coupling efficiencies. A possible solution for this problem

is to use so-called whispering-gallery-mode (WGM) microresonators. These resonators confine light by continuous total internal reflection at the boundary between two dielectric materials. Thus, the light travels along the circumference of the structure. Contrary to other resonator types, light can be coupled into and out of these WGM resonators with almost no losses via frustrated total internal reflection using tapered fiber couplers [11]. Whispering-gallery-mode resonators have been realized in microspheres [12], microtoroids [13] or, in our case, in so-called bottle microresonators [14], demonstrating extremely high quality factors (Q-factors) exceeding $10^8$ and small mode volumes, compatible with strong coupling. Thus, high-Q WGM microresonators are well suited for applications where photon losses are critical.

In the experiment presented in this thesis, a whispering-gallery-mode bottle microresonator (WGMBR) is used. Compared to other WGM resonators, the bottle resonator has the advantage of being fully tunable [15, 16] and allows one to couple two independent nanofibers to the same resonator mode [17]. In order to study the interaction between single atoms and the light in the resonator, an atomic fountain is employed for delivering laser-cooled rubidium atoms to the evanescent field of the resonator. Since these atoms are not trapped, the transit time through the resonator mode of several microseconds sets the time scale of the experiment. Using this apparatus, strong coupling between the atoms and the resonator field was demonstrated [18]. Furthermore, it was shown that the presence of a longitudinal polarization component in the evanescent field prevents the formation of uncoupled standing wave mode which was previously thought to be a major limitation of WGM systems [18]. Furthermore, an all-optical switch operated by a single atom has been demonstrated [19].

The next experimental goal is to implement so-called quantum switching [20], where the atom is prepared in a coherent superposition state. This concurrently would put the field in a coherent superposition of the two distinct output fields. Such a state, where a small quantum system (single atom) is entangled with a macroscopic system (light field containing many photons) is called Schrödinger cat state [21]. These non-classical cat states have been realized in different systems, e.g., with trapped ions [22] and microwave photons in high-Q resonators [23, 24]. Our low-loss WGMBR-based system should be well suited for a deterministic generation of Schrödinger cat states in the optical domain, where an incident light pulse is routed into one out of two possible outputs.

This thesis describes first steps taken toward the realization of a quantum switch for light. In chapter 2, the basic theory of the atom-resonator system is presented. The first part describes the light-confining properties of our WGMBR, focusing on the polarization in the evanescent fields in these modes. Then, the Jaynes Cummings model which can be used to describe the interaction between light and matter is introduced. This model is then generalized to describe the quantum mechanical interaction between a rubidium atom and

the modes of our bottle resonator, taking into account the longitudinal polarizations of the evanescent field. It will later be employed to obtain an deeper understanding of our measurements.

The existing experimental apparatus is briefly discussed in chapter 3 and the experimental methods for investigating the atom-resonator interaction are introduced. Moreover, the recent achievements using this setup are summarized and a possible realization of a quantum switch is described.

In chapter 4, a new atom-resonator interrogation scheme, based on polarization rotation, is presented. The advantages of this method for the real-time detection of atoms in the vicinity of the resonator are derived and experimentally demonstrated. Furthermore, first steps toward an optical switch based on this scheme are performed and discussed in detail. In order to implement a quantum switching scheme, a coherent state manipulation of the atom is required. Chapter 5 describes possible methods that can be applied for this manipulation. An optical setup developed for this purpose is characterized and the design for magnetic bias field coils is presented. In the last chapter, a summary of the results and a short outline of the perspectives of the experiment are given.

# Chapter 2

# Theoretical framework

## 2.1 Whispering-gallery-mode microresonators

Optical microresonators confine light in a small volume. Due to the resulting enhanced field strength, such resonators are well suited for experiments in cavity quantum electrodynamics (CQED), where atoms are strongly coupled to single resonator modes. However, optical microresonators are also found in other areas, such as telecommunication or biochemistry, where they are used as filters [25] or for sensing [26]. Optical microresonators are characterized by two key parameters. The first is the quality factor $Q$, which is defined as the photon lifetime $\tau$ inside the resonator, multiplied with the angular frequency of the light $\omega$

$$Q = \tau \, \omega \, . \tag{2.1}$$

The second is the mode volume, which quantifies the spatial extension of the resonator mode

$$V = \int_{\mathbb{R}} d^3r \, n^2(\vec{r}) \frac{I(\vec{r})}{I_{max}} \, , \tag{2.2}$$

where we have introduced the local refractive index $n(\vec{r})$ and intensity $I(\vec{r})$ and the maximum intensity $I_{max}$. These two parameters are especially important, when coupling atoms to the resonator modes, since the coupling strength of the interaction is inversely proportional to $\sqrt{V}$, and $Q$ defines how long light can coherently interact with an atom.

There are numerous types of microresonators used for different applications. For example, Fabry-Perot microresonators [27] or photonic crystal resonators [28] are widely used. In our experiment we employ a bottle microresonator [14], which is a novel type of whispering-gallery-mode (WGM) microresonator. In such a WGM resonator, the light is guided near the surface by continuous total internal reflection. Compared to other resonator types, WGM microresonators combine very high atom-light coupling strengths and low coupling losses when using tapered fiber couplers. This renders this type of mi-
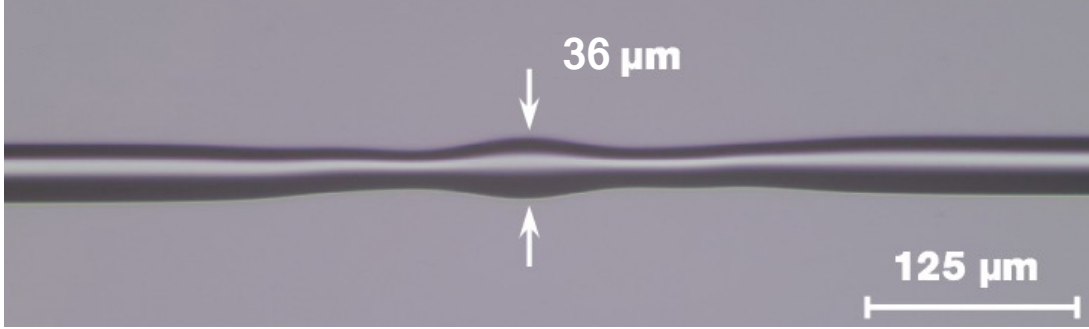
**Figure 2.1:** Micrograph showing the bottle microresonator, in between the two microtapers. Adapted from [19].

croresonator a powerful tool for applications in CQED. In the following, the fundamental properties of our bottle microresonators will be discussed.

## 2.1.1 The bottle microresonator

In our experiment we use whispering-gallery modes, formed inside a so-called bottle microresonator. Both, the bottle microresonator as well as the tapered fibers which are used to couple light into the WGM of the resonator, are made in our group from commercial optical fibers using a heat and pull process [17]. In order to obtain the bottle shape which is required for confining the light in axial direction, the fiber diameter is first reduced to around 30-40 $\mu$m, in a first pulling process. Then the taper is locally heated at two spots, using a focused $CO_2$-laser while slightly stretching the fiber, thus forming the resonator. The bottle resonators used in our experiment, has a central diameter of 36 $\mu m$ and a curvature of the resonator profile of $\Delta k \approx 0.014$ $\mu$m$^{-1}$, as depicted in Fig. 2.1. The curvature of the bottle shape causes a harmonic potential for the light in axial direction (see Fig. 2.2). Radially, the light is confined by continuous total internal reflection and guided along the circumference [29].

A very important feature of resonators, that support WGM inside a dielectric structure is that there exists a so-called evanescent field outside the dielectric structure which decays exponentially with increasing distance. These evanescent fields offer the opportunity to couple light with almost 100% efficiency into and out of the resonator using coupling prisms or tapered fibers . At the same time, atoms that come close enough to the resonator surface can be coupled to the evanescent field. Both techniques are employed in our experiment, as I will discuss later.

In the next section, the coupling of light into and out of the resonator using tapered optical fibers is briefly discussed.
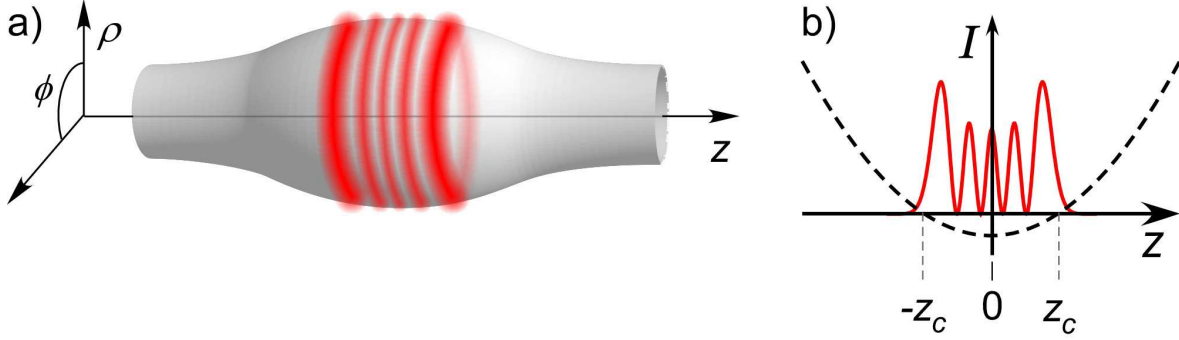
**Figure 2.2:** a) Schematic of the bottle resonator with a $q = 4$ mode (red). b) The weak curvature of the bottle resonator causes a parabolic potential for the light, providing axial confinement between the two caustics at $\pm z_c$. Adapted from [19].

## 2.1.2 Coupling light into the bottle microresonator

In our experimental setup, two tapered optical nanofibers are used to couple light into and out of the bottle resonator.

The coupling between the resonator mode and the mode guided in the coupling fiber can be characterized by introducing the coupling rate $\kappa_e$. In addition, the loss rate $\kappa_0$ has to be considered, corresponding to the intrinsic losses of the resonator caused by surface roughness or coupling to other modes. The coupling rate $\kappa_e$ strongly depends on the size of the gap $x$ between the fiber and the resonator and the phase matching, between the light guided in the fiber and the resonator. The latter means that the propagation constant of the light, guided in the resonator and the coupling fiber, should be identical. When sending light which is resonant with the resonator through the coupling fiber, its steady state transmission is given by [30]

$$T(x) = \left| \frac{a_{\text{in}}}{a_{\text{out}}} \right|^2 = \left( \frac{\kappa_e(x) - \kappa_0}{\kappa_e(x) + \kappa_0} \right)^2, \tag{2.3}$$

where $a_{\text{in}}$ and $a_{\text{out}}$ correspond to the amplitudes of the incident and transmitted field, as shown in Fig. 2.3a. The transmission can be divided into two regimes, as depicted in Fig. 2.3b [31, 32]. For large distances, the coupling between the resonator and the tapered fiber is weak and most of the light stays in the fiber. This is called the under-coupled regime where $\kappa_e < \kappa_0$. At a certain distance, $\kappa_e = \kappa_0$ and all the light is coupled from the fiber to the resonator and is dissipated therein. For this so-called critical coupling, the light stored in the resonator adjusts such that the light coupled out of the resonator has the same amplitude as the light in the coupling fiber. Due to the phase shift of $\pi$ of the out-coupled light, full destructive interference occurs and the transmission of the coupling fiber drops to zero. When the fiber further approaches the resonator, some light is coupled out of the resonator, before it is dissipated, causing the fiber transmission to
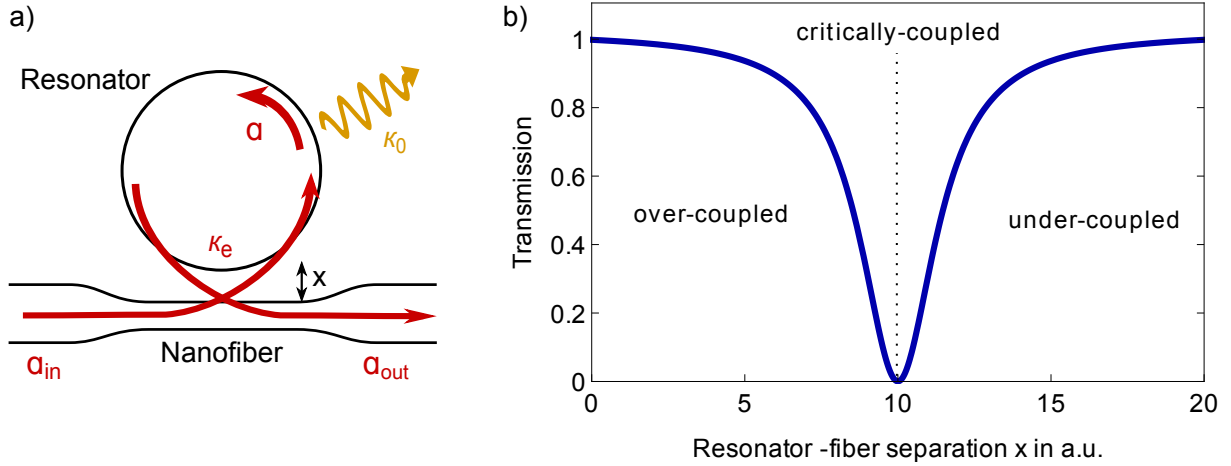
**Figure 2.3:** a) Sketch of the evanescent coupling process between a nanofiber and a bottle microresonator, where $a$ is the amplitude of the resonator mode, $a_{in}(a_{out})$ the amplitude of the in(out)-coupling fiber mode, $\kappa_0$ is the rate of the intrinsic losses of the resonator and $\kappa_e$ the coupling rate between the fiber mode and the resonator mode. b) The fiber transmission as a function of the distance between the coupling fiber and the resonator, around the point of critical coupling.

rise again. This is called the over-coupled regime, where $\kappa_e > \kappa_0$.

The fact that it is straightforward to change the coupling rate $\kappa_e$ by changing the fiber-resonator distance is a significant advantage over conventional Fabry-Perot resonators. For these types of resonators this would require a mirror with tunable reflectivity, which is not feasible up to now.

### 2.1.3   Calculation of the bottle modes

In this section, the mode structure that forms inside a bottle resonator will be discussed, following the description introduced in [30, 29].

Due to the cylindrical symmetry of our bottle resonator, the description will be performed in cylindrical coordinates $(\rho, \phi, z)$, as indicated in Fig. 2.2. The small curvature of the bottle resonator in axial direction has several simplifying consequences that will help us to calculate the mode structure. First of all, the curvature can be well approximated by a parabolic profile along the z-axis

$$R(z) \approx R_{z=0}\left(1 - \frac{(\Delta k \cdot z)^2}{2}\right) , \tag{2.4}$$

with the central radius $R_{z=0}$ and a curvature $\Delta k$. Since we only consider small variation of the resonator radius and modes that are located close to the surface, the radial component of the wave vector can be neglected. The cylindrical symmetry of the resonator also implies

that the projection of the angular momentum of the light on the $z$ axis is conserved and that the z-component of the wave vector $k_z$ vanishes at the resonator caustic $(z_c)$. Thus, the azimuthal component $k_\phi$ varies between its minimum at the center of the bottle and its maximum at the caustic, leading to a $z$-dependency, which can be expressed as

$$k_\phi(z) = k\, \frac{R_{z=z_c}}{R(z)} \; . \tag{2.5}$$

If we now assume an adiabatic variation of the resonator radius, we can also neglect the weak z-dependence of $k_\phi$. This makes it possible to separate the solution of the vector wave equation

$$(\nabla^2 + k^2)\vec{\psi} = 0 \quad \text{into} \quad \vec{\psi} = \mathcal{R}(\rho)\Phi(\phi)\mathcal{Z}(z) \; , \tag{2.6}$$

where $\vec{\psi}$ corresponds to the electric and magnetic field vectors. Due to the cylindrical symmetry, the azimuthal solution is given by $\Phi(\phi) = \exp(im\phi)$, where the mode number $m$ counts the number of wavelengths around the circumference. For counterpropagating waves, the sign of the argument changes. The radial part resembles the Bessel equation which is solved by Bessel functions. The axial wave equation reduces to an harmonic oscillator and thus the solutions are given by Hermit polynomials $H_q$ (see Fig. 2.2b). The axial quantum number $q$ corresponds to the number of intensity nodes along the resonator axis. These considerations give rise to a large number of possible modes for such a resonator geometry, which can be seen, e.g., in a typical experimental spectrum, as shown in Fig. 2.4. The frequency difference between two adjacent modes is called free spectral range and can be approximated for axial and azimuthal modes by

$$\Delta\nu_q \approx \frac{c\Delta k}{2\pi n} \qquad \Delta\nu_m \approx \frac{c}{2\pi n R_{z=0}} \; . \tag{2.7}$$

For our bottle resonator geometry this gives $\Delta\nu_q \approx 0.4$ THz and $\Delta\nu_m \approx 1.9$ THz.

A very beneficial feature of our bottle resonator is that its resonance frequency can be tuned elasto-optically, by applying strain to the fiber using a piezo element. This strain will affect the resonator's refractive index $n$ and diameter $D$ and thus causes a fractional change in frequency according to

$$\frac{\Delta\nu}{\nu_0} \approx -\frac{\Delta n}{n} - \frac{\Delta D}{D} \; . \tag{2.8}$$

This enables us to tune the resonance frequency of the bottle resonator over a range of several hundred GHz [14, 17]. This is an important advantage over most other WGM microresonator experiments, where the tuning can only be realized by changing the temperature [33, 34].
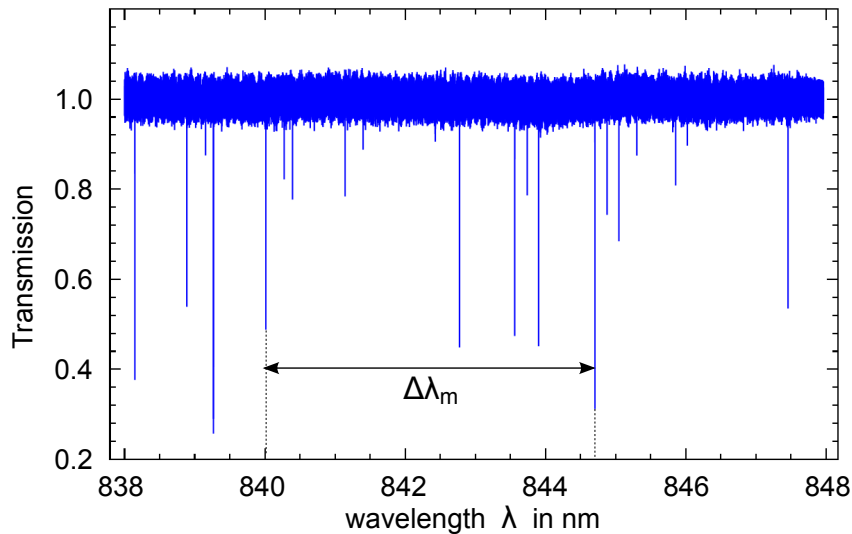
**Figure 2.4:** Transmission spectrum of our bottle microresonator. The scan covers a more than a free spectral range $\Delta\lambda_m = 4.62$ nm or $\Delta\nu_m = 1.96$ THz. This is in good agreement with the estimation given by Equ. 2.7.

## 2.1.4 Polarization of the TM and TE bottle modes

In this section, we will take a closer look at the polarization of the light in WGMs. For this, we will first discuss the principles of total internal reflection, for the case that the incoming light strikes a plane dielectric interface.

When a plane wave, propagating through a dielectric medium of high refractive index $n_1$, encounters an interface with a medium of lower refractive index $n_2$, it undergoes total internal reflection for incident angles $\theta$ greater than the critical angle $\theta_c = \arcsin(n_2/n_1)$. Although the field is entirely reflected, there still exists a field beyond the interface. This so-called evanescent field exponentially decays with increasing distance $y$ from the interface. Its penetration depth $d = \lambda/4\pi\sqrt{n_1^2\sin^2\theta - n_2^2}$, is typically on the order of the wavelength $\lambda$. The amplitude of the evanescent field depends on the angle $\theta$ and on the incident polarization. We have to distinguish between polarization perpendicular and parallel to the plane of incidence ($x$-$y$ plane). Only for the case of perpendicular polarized light, the evanescent field's polarization is exclusively transversal to the plane of propagation. Contrary, for light polarized parallel to the plane of incident, in addition to a component perpendicular to the interface $\vec{E}_y$, we also get a longitudinal component $\vec{E}_x$, oscillating in propagation direction, as depicted in Fig. 2.5. These two electric field components are $\pi/2$ out of phase and the ratio of their field amplitudes is given by

$$\frac{E_x}{E_y} = i\sqrt{1 - \frac{1}{\sin^2\theta}\left(\frac{n_2}{n_1}\right)^2} \;.$$
(2.9)

11
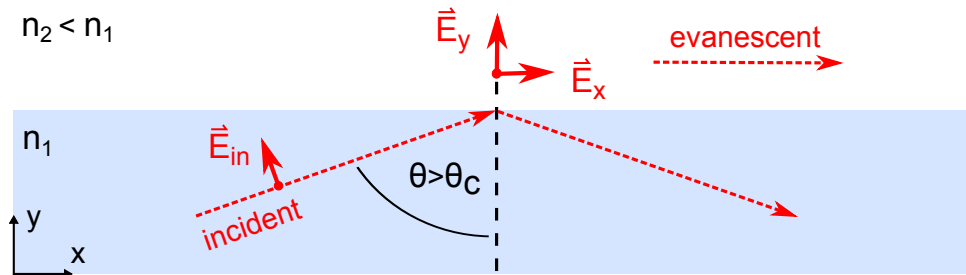
**Figure 2.5:** For $n_2 < n_1$ and angles larger than the critical angle $\theta_c$, the light is totally internally reflected. Nevertheless, an evanescent field is formed beyond the interface, which decays exponentially. For incoming light, which is polarized parallel to the plane of incidence, the evanescent field has both, a transversal field component $\vec{E}_y$ and a longitudinal field component $\vec{E}_x$. That means the evanescent field also oscillates in the direction of the wave vector (indicated by a dashed arrow).

The ratio can never become one, thus the evanescent field is always elliptically polarized. These effects are commonly applied to study molecular and cellular interfaces [35].

A WGM bottle resonator also supports modes of different polarization. Their resonance frequencies are, due to the high birefringence of the resonator, separated by hundreds of GHz. Again, we distinguish between modes where the electric field oscillates parallel to the resonator axis (i.e., perpendicular to the plane of incidence) and those perpendicular to the resonator axis (i.e., parallel to the plane of incidence). For the former, the electric field is parallel to the resonator axis and one therefore speaks of transverse electric (TE) modes. For transverse magnetic (TM) modes, the only non-vanishing magnetic field component is parallel to the resonator axis.

Transverse electric WGMs are almost exclusively transversely polarized, i.e., their electric field vector is perpendicular to their wave vector, at any position of the mode (see Fig. 2.7a). Figure 2.6a shows the decay of the electric field amplitude for this case. The electric fields of two counterpropagating TE-waves in WGM resonators, oscillate in the same direction. This makes interference between counterpropagating modes possible and thus enables the formation of standing waves.

In qualitative contrast, due to the physics of total internal reflection, TM modes have two electric field components $\vec{E}_r$ and $\vec{E}_\phi$, and thus are non-transversely polarized. This means that the electric field vector has a non-vanishing component along the propagation direction. The total electric field is given by

$$\vec{E}_{\mathrm{TM}}^{\pm} = \vec{E}_r \pm i\vec{E}_\phi \; , \tag{2.10}$$

where the $+$ $(-)$ sign follows from Fresnel equations for the clockwise (counter-clockwise) propagation of the mode with respect to the $z$ axis. The relative strength of these com-
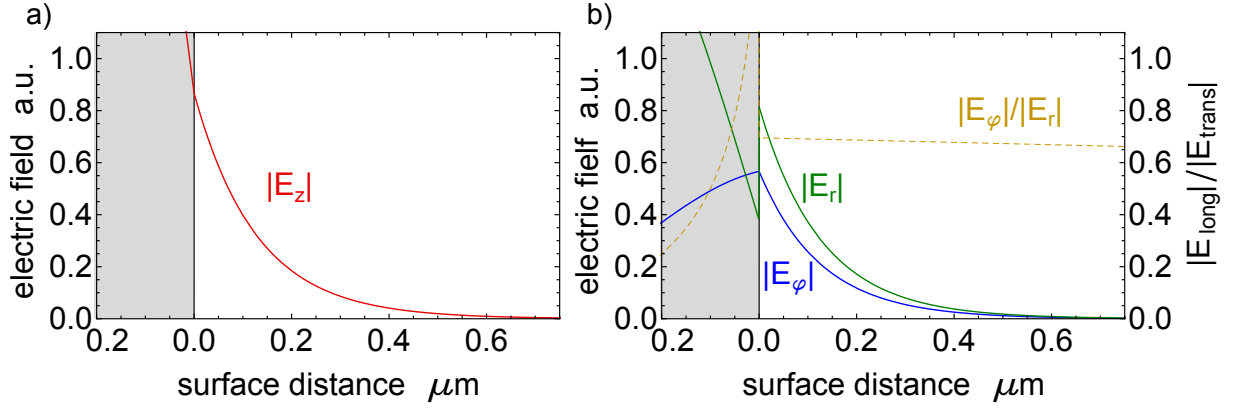
**Figure 2.6:** a) Transversal field component $|E_z|$ of a TE mode as a function of the distance to the resonator. b) In the case of TM modes a longitudinal $|E_\phi|$ and a transversal $|E_r|$ electric field component occur. Their ratio is almost independent of the distance from the resonator surface. The fields are calculated for parameters corresponding to the bottle microresonator used in our experiment.

ponents can be calculated with Equ. 2.9. Since we are only interested in modes close to the surface, we can assume $\theta \rightarrow 90°$, yielding $|\vec{E}_\phi|/|\vec{E}_r| \approx 0.7$, for $n_1 = 1.45$ and $n_2 = 1$. This is in good agreement with exact calculations, as depicted in Fig. 2.6b. Due to the relative phase of $90°$ between the two components, the light is nearly circularly polarized. The overlap with ideally circular polarization, defined as the normalized unit vector $\vec{e}_{\sigma_\pm}$, gives

$$\frac{|\vec{E}_{\mathrm{TM}}^\pm \cdot \vec{e}_{\sigma_\pm}^*|^2}{|\vec{E}_{\mathrm{TM}}^\pm|^2} > 0.96 \ . \tag{2.11}$$

This overlap is almost independent of mode number and resonator size. The high overlap allows us to treat light in TM modes as circularly polarized light and the two counter-propagating modes ($\mathrm{TM}^+$ and $\mathrm{TM}^-$) are almost perfectly orthogonally polarized. Thus, superimposing two counterpropagating TM waves will not yield a standing wave, but a polarization gradient, where at each point of the circumference the field has a well defined, linear polarization and a non-zero amplitude.

When taking a closer look at the polarization of a propagating photon along the circumference of the resonator, the polarization vector resembles the tip of the rotor of a horizontally flying helicopter, which describes a cycloid (see Fig. 2.7b).
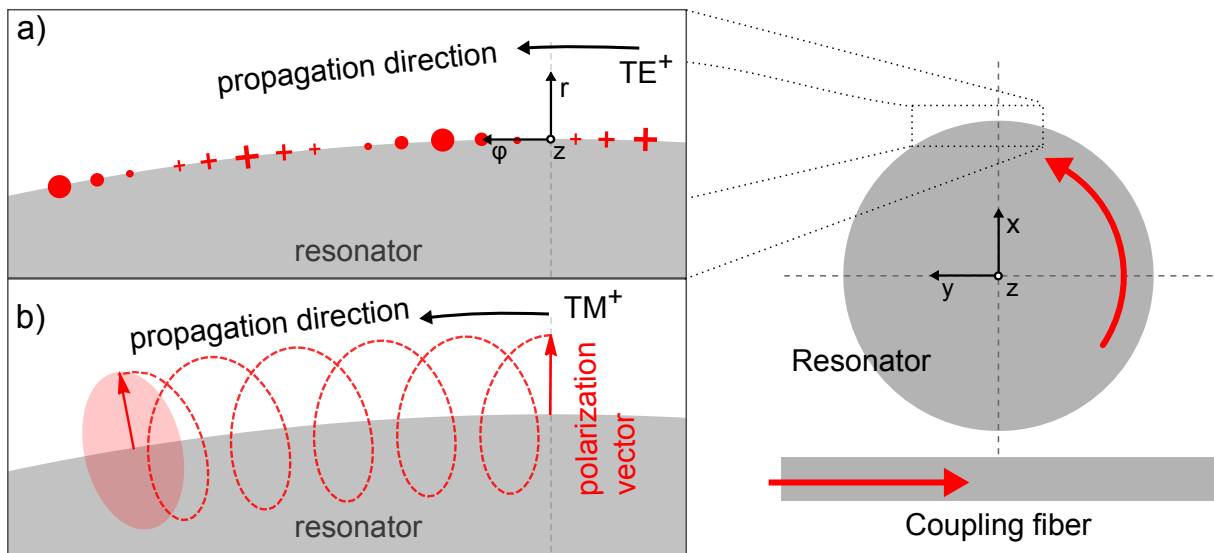
**Figure 2.7:** a) Snap-shot of a TE-polarized traveling mode, where (•) corresponds to a field amplitude pointing in positive and (+) in the negative z-direction. b) Trajectory of the polarization vector of a traveling TM photon.

## 2.2 Light-matter interaction

In this section, the basic theoretical description of atom-light interaction will be introduced and applied to our bottleresonator system. This will allow us to get a deeper understanding of our system's behavior.

### 2.2.1 Jaynes-Cummings Model

The interaction of a single two-level atom with a single light mode is described by the Jaynes-Cummings model [36]. The Hamiltonian of a quantized single mode light field is given by

$$\hat{H}_L = \hbar\omega_L \hat{a}^\dagger \hat{a} \,, \tag{2.12}$$

where the ground state energy has been set to zero. The operators $\hat{a}^\dagger$ and $\hat{a}$ correspond to the photon creation and annihilation operator, which act on a Fock state $|n\rangle$ and have to fulfill the Bose commutation relation. The frequency of the light is $\omega_L$. The Hamiltonian of the free atom can be written as

$$\hat{H}_A = \frac{1}{2}\hbar\omega_A \hat{\sigma}_3 \,, \tag{2.13}$$

where the transition frequency $\hbar\omega_A$ is the energy difference between the atomic ground state $|g\rangle$ and excited state $|e\rangle$ and $\hat{\sigma}_3 = |e\rangle\langle e| - |g\rangle\langle g|$ is the inversion operator. The interaction between the atom and the field in rotating wave approximation (RWA) is described by

$$\hat{H}_I = \hbar\,g\,(\hat{a}^\dagger \hat{\sigma}_- + \hat{a}\hat{\sigma}_+) \,. \tag{2.14}$$

Here, the atomic raising $\hat{\sigma}_+ = |e\rangle\langle g|$ and lowering operator $\hat{\sigma}_- = |g\rangle\langle e|$ are introduced. The coupling strength $g$ is proportional to the field strength per photon $E_0$ and, using the dipole operator matrix element $d$ and the mode volume $V$, can be written as

$$g = \frac{E_0}{\hbar}d = \sqrt{\frac{\omega_L}{\hbar\epsilon_0 V}}d \,, \tag{2.15}$$

where $\epsilon_0$ is the dielectric constant. Already at this point it becomes clear that microresonators, which inherently have a small mode volume V, are well suited for applications that require high interaction strength between light and matter. The total Hamiltonian of the composite atom-light system thus reads

$$\hat{H}/\hbar = \omega_L \hat{a}^\dagger \hat{a} + \frac{1}{2}\omega_A \hat{\sigma}_3 + g\,(\hat{a}^\dagger \hat{\sigma}_- + \hat{a}\hat{\sigma}_+) \,. \tag{2.16}$$
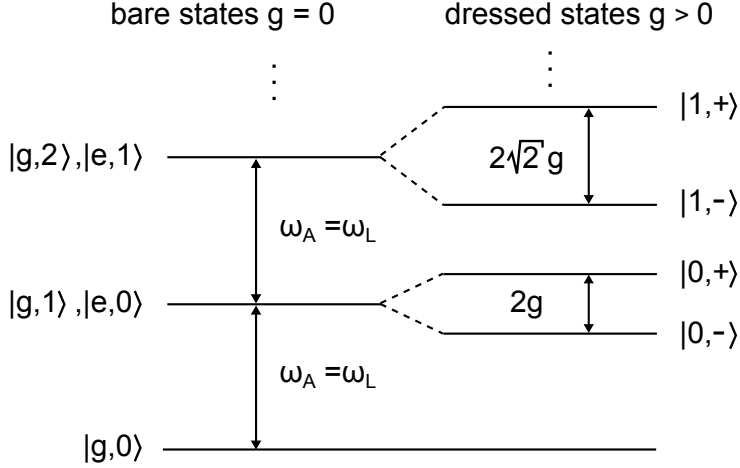
**Figure 2.8:** Jaynes-Cummings ladder of states for $\Delta_{AL} = 0$.

This Hamiltonian only causes transitions between the so-called "bare states" $|e, n\rangle \leftrightarrow |g, n + 1\rangle$. Using them as our basis, the Hamiltonian given by Eq. (2.16) can easily be diagonalized, yielding the following eigenenergies

$$E_{\pm,n} = \frac{\hbar}{2}\Big((2n + 1)\omega_A \pm \Omega_n\Big) , \tag{2.17}$$

where we have introduced the quantum Rabi frequency $\Omega_n = \sqrt{4g^2(n + 1) + \Delta_{AL}^2}$, with the detuning between the atomic transition and the light field $\Delta_{AL} = \omega_A - \omega_L$ . The eigenstates associated with the energy eigenvalues, which are often referred to as "dressed state", are

$$|n, +\rangle = \quad \cos(\phi_n/2)\,|g\rangle\,|n + 1\rangle + \sin(\phi_n/2)\,|e\rangle\,|n\rangle \tag{2.18}$$

$$|n, -\rangle = \quad -\sin(\phi_n/2)\,|g\rangle\,|n + 1\rangle + \cos(\phi_n/2)\,|e\rangle\,|n\rangle \ , \tag{2.19}$$

where $\phi_n$ is defined through $\tan\phi_n = 2g\sqrt{n + 1}/\Delta_{AL}$. If the light field is tuned to the atomic resonance $\omega_L = \omega_A$, so that $\Delta_{AL} = 0$, the eigenenergies and eigenstates reduce to

$$E_{\pm,n} = \quad \frac{\hbar}{2}\Big((2n + 1)\omega_A \pm 2g\sqrt{n + 1}\Big) \tag{2.20}$$

$$|n, \pm\rangle = \quad \frac{1}{\sqrt{2}}(|g\rangle\,|n + 1\rangle \pm |e\rangle\,|n\rangle) \ , \tag{2.21}$$

which yields the anharmonic Jaynes-Cummings ladder shown in Fig. 2.8. If we limit ourselves to the first excitation of the coupled system, the energy splitting between the dressed states is $2g$, often referred to as vacuum-Rabi splitting.

## 2.2.2 Description for dissipative systems

Let us now apply the idealized theory on a more realistic problem, such as a Fabry-Perot resonator with a single field mode $a$, by adding several dissipative channels. A real resonator will inevitably introduce losses, which cause a finite lifetime $\tau$ of a photon inside the resonator, represented by the cavity decay rate $\kappa = 1/\tau$. Furthermore, the excited atomic state will spontaneously decay into free space with rate $\gamma$. In order to observe coherent interaction in such a cavity quantum electrodynamics (CQED) experiment, all dissipative processes have to be slower than the coherent dynamics. This parameter regime is known as strong coupling and can be summarized as

$$g \gg \kappa, \gamma \ . \tag{2.22}$$

If we now also drive our system with strength $\epsilon = \langle a_{in} \rangle$, where we have introduced the expectation value of the amplitude of the incident light $a_{in}$ (see Fig. 2.9a), we have to add a driving term to our Jaynes-Cummings Hamiltonian (Eq. (2.16))

$$\hat{H}/\hbar = \Delta_{CL}\hat{a}^{\dagger}\hat{a} + \Delta_{AL}\hat{\sigma}_{+}\hat{\sigma}_{-} + g\,(\hat{a}^{\dagger}\hat{\sigma}_{-} + \hat{a}\hat{\sigma}_{+}) + \sqrt{\kappa_e}(\epsilon\hat{a}^{\dagger} + \epsilon^{*}\hat{a}) \ . \tag{2.23}$$

Here, we have also performed the rotating frame transformation where the system is transformed into a frame that rotates with the frequency of the light field $\omega_L$. Therefore, one has to replace the frequency $\omega_L$ by the detuning between the atom and the laser $\Delta_{AL} = \omega_A - \omega_L$ and $\omega_C$ by the detuning between the cavity and laser field $\Delta_{CL} = \omega_C - \omega_L$. As before, the first two terms in Eq. (2.23) correspond to the free field and atom. The third represents their interaction and the last term incorporates the driving of the cavity field.

In order to take into account the losses, the evolution is described by the master equation [37]

$$\frac{d\hat{\rho}}{dt} = -i[\hat{H}, \hat{\rho}] + \kappa(2\hat{a}\hat{\rho}\hat{a}^{\dagger} - \hat{a}^{\dagger}\hat{a}\hat{\rho} - \hat{\rho}\hat{a}^{\dagger}\hat{a}) + \gamma(2\hat{\sigma}_{-}\hat{\rho}\hat{\sigma}_{+} - \hat{\sigma}_{+}\hat{\sigma}_{-}\hat{\rho} - \hat{\rho}\hat{\sigma}_{+}\hat{\sigma}_{-}) \ , \tag{2.24}$$

where $\hat{\rho}$ is the density matrix of the coupled atom-resonator system. In the weak driving limit, we can truncate the state space for a two level atom to $\{|g,0\rangle, |g,1\rangle, |e,0\rangle\}$ and we can obtain a analytic steady-state solution. The expectation value of the cavity field mode is

$$\langle \hat{a} \rangle_{FP} = \frac{-i\epsilon(\gamma + i\Delta_{AL})}{g^2 + (\gamma + i\Delta_{AL})(\kappa_0 + \kappa_e + i\Delta_{CL})} \ . \tag{2.25}$$

The transmission of a Fabry-Perot resonator can be calculated from the cavity field by using $T_{FP} = \frac{\langle \hat{a}^{\dagger}\hat{a} \rangle}{|\epsilon|^2}$. When the cavity is tuned to the atomic resonance ($\Delta_{CA} = \Delta_{CL} - \Delta_{AL} = 0$), the transmission spectrum without an atom present ($g = 0$) will give a Lorentzian,
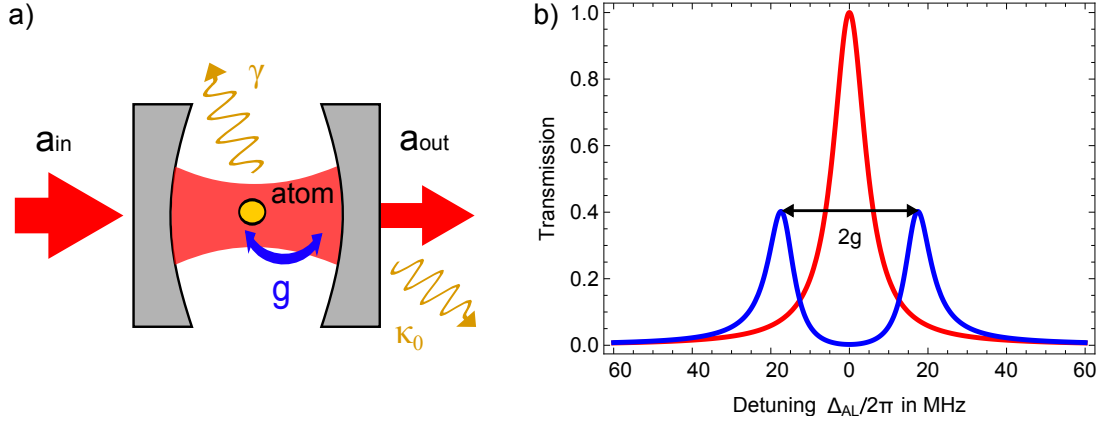
**Figure 2.9:** a) Schematic of the Fabry-Perot setting. b) Transmission spectrum for a Fabry-Perot cavity with (blue) and without (red) atom, as a function of the laser-atom detuning, for $(g, \gamma, \kappa, \Delta_{AC}) = 2\pi(20,3,5,0)$ MHz.

centered at the cavity resonance frequency. Adding an atom that couples to the resonator mode ($g \neq 0$) will cause a vacuum-Rabi splitting, yielding a two peak spectrum, with peak separation $2g$, as depicted in Fig. 2.9. The fact that we can resolve two separate peaks demonstrates that the system is in the strong coupling regime.

### 2.2.3 Coupling whispering-gallery modes to single atoms

Now we want to consider a whispering-gallery mode resonator, as shown in Fig. 2.10. As we have seen in section 2.1.4, the properties of whispering gallery modes fundamentally depend on the polarization. Thus, the atom-light interaction changes significantly, compared to the case discussed before. The resonator guides orthogonally circularly polarized modes $\sigma_\pm$ (TM$^\pm$) as well as linearly polarized modes $\pi$ (TE$^\pm$), where the quantization axis is aligned along the resonator axis. Since these modes correspond to three different orthogonal polarizations, they drive transition between different Zeemann sublevels. Thus, the multilevel structure of the atom has to be taken into account. Form now on,
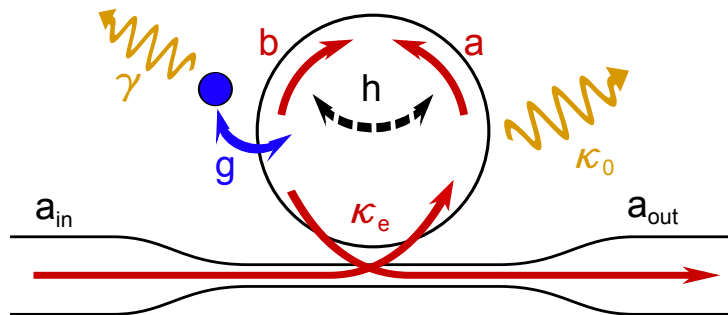


**Figure 2.10:** Schematic of the considered system. Same as Fig. 2.3a, but now including a second counterpropagating resonator mode $b$ and a single atom that couples to the resonator modes with strength $g$.

18
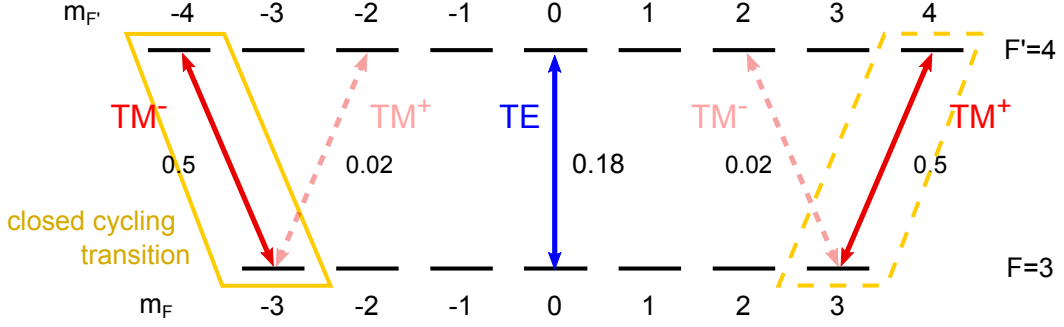
**Figure 2.11:** Relevant atomic levels for $^{85}$Rb. Due to the strong overlap with $\sigma_\pm$ polarization, TM modes drive $\Delta m_F = \pm 1$ transitions, while the $\pi$-polarized TE modes drive $\Delta m_F = 0$ transitions. When probing with TM$^+$(TM$^-$) light, the atom will be pumped into the $m_F = +3$ ($m_F = -3$) state. Form this state the atom can only be excited into the $m_{F'} = +4$ ($m_{F'} = -4$) level, from where it can only decay back into the state it came from. Thus a closed cycling transition is formed.

we therefore consider atoms with a level structure as depicted in Fig. 2.11. For an exact solution, we would have to extend our Hamiltonian by taking into account the different polarizations of the modes and the different transitions they drive. In the following, we will try to find simplifying conditions, which occur when only driving our system with a single mode and try to derive a steady state solution.

**TE mode**

Let us first consider an atom coupling to a TE-polarized mode. As we have seen in section 2.1, the resonator supports two degenerate counterpropagating linearly polarized TE modes. Thus, an atom will interact in the same way with both traveling wave modes. If we only apply one $\pi$-polarized TE mode, which only drives $\Delta_{m_F} = 0$ transitions, the atom will, in steady-state, predominately populate the $m_F = 0$ level[1]. Thus, we can treat the system using an effective two-level Hamiltonian such as

$$
\begin{aligned}
\hat{H}/\hbar = \ & \Delta_{AL}\hat{\sigma}_+\hat{\sigma}_- \\
& + \Delta_{CL}(\hat{a}^\dagger\hat{a} + \hat{b}^\dagger\hat{b}) + h(\hat{a}^\dagger\hat{b} + \hat{b}^\dagger\hat{a}) \\
& + (g_t^{(a)}\hat{a}^\dagger\hat{\sigma}_- + g_t^{*(a)}\hat{a}\hat{\sigma}_+) + (g_t^{(b)}\hat{b}^\dagger\hat{\sigma}_- + g_t^{*(b)}\hat{b}\hat{\sigma}_+) \\
& + \sqrt{2\kappa_e}(\epsilon\hat{a}^\dagger + \epsilon^*\hat{a}) \ .
\end{aligned}
\tag{2.26}
$$

The first term corresponds to the free atom. The second line describes the two counter-propagating modes $a$ and $b$, and the coupling between these two modes at rate $h$, e.g.

---

[1]This follows directly from numerical calculations of the steady state, when taking into account all possible transitions between the different Zeeman sublevels.

due to surface scatterers. The next line gives the atom-light interaction, where we have introduced mode-dependent coupling strengths. The final term includes the driving of mode $a$, where in contrast to the Fabry-Perot case, the factor $\sqrt{2}$ has to be added, to take into account that for bottle resonators we only have one interface through which the light can couple in and out.

We can now rewrite Eq. (2.26) in a standing wave basis, using the normal modes $\hat{A} = (\hat{a} + \hat{b})/\sqrt{2}$ and $\hat{B} = (\hat{a} - \hat{b})/\sqrt{2}$ [38, 39],

$$
\begin{aligned}
\hat{H}'/\hbar = \ & \Delta_{AL}\hat{\sigma}_+\hat{\sigma}_- \\
& + (\Delta_{CL} + h)\hat{A}^\dagger\hat{A} + (\Delta_{CL} - h)\hat{B}^\dagger\hat{B} \\
& + g_s^{(A)}(\hat{A}^\dagger\hat{\sigma}_- + \hat{A}\hat{\sigma}_+) - g_s^{(B)}(\hat{B}^\dagger\hat{\sigma}_- - \hat{B}\hat{\sigma}_+) \\
& + \sqrt{\kappa_e}(\epsilon\hat{A} + \epsilon^*\hat{A}^\dagger) + \sqrt{\kappa_e}(\epsilon\hat{B} + \epsilon^*\hat{B}^\dagger) \,,
\end{aligned}
\tag{2.27}
$$

where we have introduced the standing wave coupling strengths $g_s^{(A)} = g_0 \cos\theta$ and $g_s^{(B)} = g_0 \sin\theta$, which directly depend on the azimuthal position. For an atom at a certain position, the coupling can predominantly occur to one of the two normal modes. Since the choice of A and B is arbitrary, we can define them such that $g_s^{(B)} = 0$. Diagonalizing the Hamiltonian yields three eigenstates with associated eigenenergies $\hbar(\omega_C \pm g)$ and $\hbar\omega_C$. While the first two correspond to the atom coupling to the standing wave mode A, the latter is caused by the uncoupled standing wave mode mode B.

In our experiment, the resonator field is not directly accessible and we have to infer the dynamics of the system from analyzing the light in the coupling fiber. The transmission through the coupling fiber can be approximated using (see Fig. 2.10)

$$
T = |\langle\hat{a}_{out}\rangle|^2 = |\epsilon - i\sqrt{2\kappa_e}\langle\hat{a}\rangle|^2 \,,
\tag{2.28}
$$

where the expectation value of amplitude of the running wave mode $a$ is calculated using the master equation ansatz. When probing the coupling fiber transmission as a function of the laser frequency, gives a spectrum with three resonances at $\omega_C \pm g$ and $\omega_C$, as depicted in Fig. 2.12b. Due to the additional peak the transmission at resonance only rises to 25%. This can be explained when taking a closer look at the interaction between the different modes and the atom. Since the atom exclusively couples to the standing wave mode A, only 50% of the light of the incoupled running wave mode $a$ interacts with the atom. While the light in the standing wave mode B is dissipated. When decomposing A again into two counterpropagating running waves, only half of the light will contribute to the output field mode in forward direction, $a_{out}$. In total, maximally 25% of the light is transmitted on resonance, when an atom couples to the resonator. This fundamentally limits the performance of TE modes for coupling light and matter.

**TM mode**

A basically different situation is encountered when considering the atom interacting with a TM mode. In this case, we have two almost perfectly orthogonal, counterpropagating, circularly polarized traveling waves. Thus, a superposition of two counterpropagating waves will not form a standing wave with intensity nodes, but a polarization gradient, where each point of the circumference has a well defined linear polarization. This rules out the existence of uncoupled standing wave modes that occur for TE modes. Thus, an atom couples to both modes independent of its azimuthal position. Furthermore, the two counterpropagating circularly polarized modes drive transitions between different Zeeman states $\Delta m_F = \pm 1$. Hence, it is not straightforward to consider the atom as an easy-to-handle two-level system.

Nevertheless, when only one running wave mode is probed , e.g. TM$^+$ (TM$^-$), the atom will be pumped into the outermost $m_F = 3$ ($m_F = -3$) state. From there, the atom can only be excited into the $m_{F'} = 4$ ($m_{F'} = -4$) state. Now the atom can only decay back into the state, from which it came from, thus forming a so-called closed cycling transition (see Fig.2.11) and the atom only interacts with the probed resonator mode. When neglecting the direct coupling between the two counterpropagating modes, this system resembles the ideal case of an effective two-level atom that only couples to a single resonator modes and thus can be described by the master equation approach, using the simplified Hamiltonian

$$
\begin{aligned}
\hat{H}/\hbar = \ & \Delta_{AL}\hat{\sigma}_+\hat{\sigma}_- + \Delta_{CL}\hat{a}^\dagger\hat{a} \\
& + (g_t^{(a)}\hat{a}^\dagger\hat{\sigma}_- + g_t^{*(a)}\hat{a}\hat{\sigma}_+) \\
& + \sqrt{2\kappa_e}(\epsilon\hat{a}^\dagger + \epsilon^*\hat{a}) \ .
\end{aligned}
\tag{2.29}
$$

Again, the first line describes the free atom and light field, the second the atom-light interaction and the last includes the driving of the resonator mode $a$. The resonator field mode can now be approximated in the weak driving limit as

$$
\langle\hat{a}\rangle = \frac{-i\sqrt{2\kappa_e}\epsilon(\gamma + i\Delta_{AL})}{g^2 + (\gamma + i\Delta_{AL})(\kappa_0 + \kappa_e + i\Delta_{CL})} \ .
\tag{2.30}
$$

This yields an output field mode in the fiber

$$
\langle\hat{a}_{out}\rangle = \epsilon - i\sqrt{2\kappa}\,\langle\hat{a}\rangle = \frac{\epsilon(g^2 + (\gamma + i\Delta_{AL})(i\Delta_{CL} + \kappa_0 - \kappa_e))}{g^2 + (\gamma + i\Delta_{AL})(i\Delta_{CL} + \kappa_0 + \kappa_e)} \ .
\tag{2.31}
$$

Probing the fiber coupler transmission, for an atom trapped in the closed cycling transition, the spectrum of the coupled atom-resonator system exhibits the two dip vacuum-Rabi splitting (see Fig. 2.12), in analogy to what one would expect for a conventional Fabry-Perot cavity.
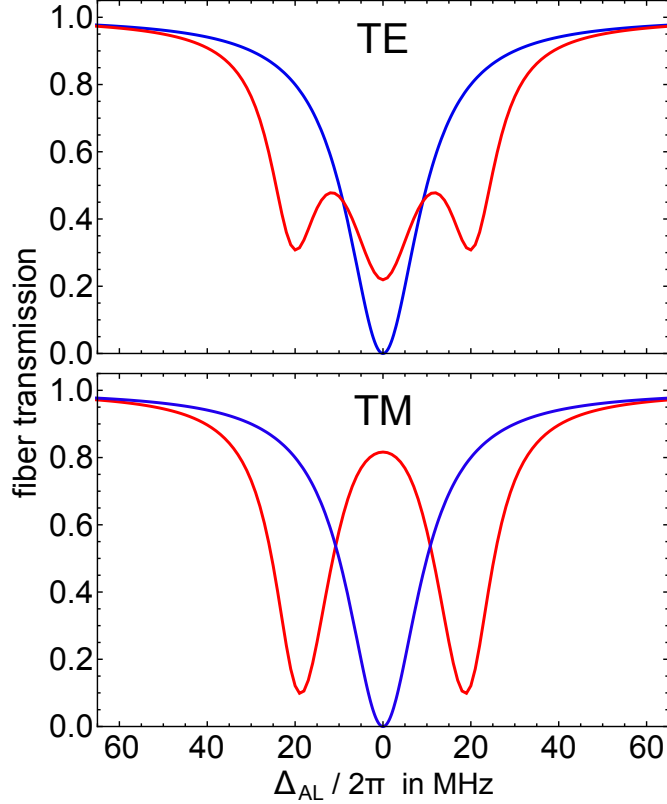
**Figure 2.12:** Theoretical predictions of the fiber transmission for TE and TM modes. The plots show the transmission as a function of the atom-light detuning, with (red) and without an atom (blue) coupled to the resonator, calculated for $(g, \Delta_{CA}, \gamma, \kappa_0, \kappa_e) = 2\pi \cdot (20, 0, 3, 10, 10)$ MHz. For the TE mode we see a vacuum-Rabi splitting with three peaks and for the TM mode we only see two peaks.

Thus, using WGM resonators, it is possible to realize a system close to the ideal case of a two-level atom that strongly interacts with a single mode. But we have to keep in mind that the polarization of the TM modes are not perfectly circularly polarized and thus will cause some excitation of unwanted states. However, these undesired transitions are strongly suppressed by the Clebsch-Gordan coefficients. Furthermore, the strong interaction of the atom with the $TM^+$ ($TM^-$) on the $F$=3, $m_F$=1 $\to$ $F'$=4, $m_{F'}$=2 ($F$=3, $m_F$=−1 $\to$ $F'$=4, $m_{F'}$=−2) transition leads to a Rabi splitting and thus detunes the transition for the orthogonally polarized, unwanted polarization component.

# Chapter 3

# Brief overview of the experimental setup

Our experiment is a complex apparatus built during the last 4 years. The design and assembly of all the parts required for studying the interaction between single atoms and light, covered several master's and PhD thesis. The heart of this experimental apparatus is a high-Q bottle microresonator, which is placed inside a ultra high vacuum chamber, with two coupling fibers. The laser-cooled cloud of atoms is prepared in a second vacuum
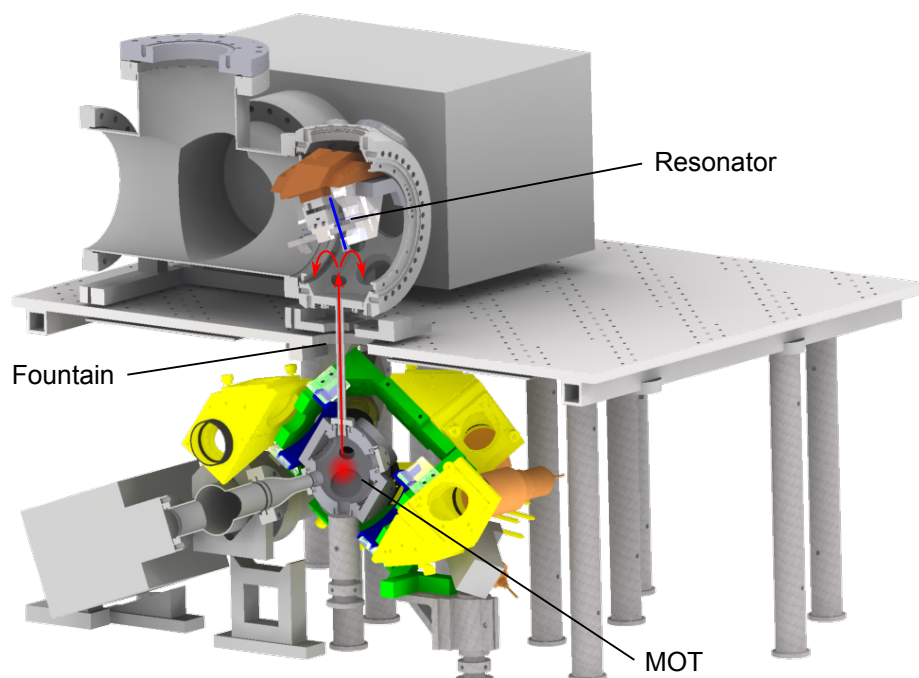


**Figure 3.1:** Cross-section through the vacuum chamber setup. The atoms are trapped and cooled in the lower vacuum chamber. Then they are launched toward the upper chamber, where the resonator and the coupling fibers are mounted. Adapted from [40].

chamber using a magneto optical trap (MOT) and is launched toward the resonator via an atomic fountain.

The actual experiments involve several steps, such as atom preparation, delivery and detection, which will be discussed in the following.

## 3.1 Atom delivery system

This section deals with the task of delivering laser-cooled rubidium atoms to the evanescent field of the resonator. The magneto optical trap required for this purpose cannot be operated in the same chamber as the resonator, because this would involve an enhanced background pressure of rubidium vapor. This would lead to a contamination of the resonator surface, introducing additional losses. Thus, a two-chamber design was chosen (see Fig. 3.1). The upper chamber, called science chamber contains the resonator and coupling fibers, including all the positioning hardware, while the lower, so-called MOT chamber contains the rubidium dispensers and the magneto optical trapping setup. The two vacuum chambers are connected via a narrow tube, which keeps up the required pressure gradient and serves as a feed-through for the cooled atom cloud.

Before the atoms are launched toward the resonator, they are captured and cooled with a MOT. This commonly used technique employs six pairwise counterpropagating laser beams of orthogonal circular polarization in combination with a magnetic field produced by an anti-Helmholtz coil configuration. After additional polarization gradient cooling, the atoms reach a temperature of 5-6 $\mu$K, corresponding to an rms velocity of 50 mm/s. This guarantees that the cloud does not expand excessively before reaching the resonator. In order to overcome the 30 cm distance between the center of the MOT and the resonator, the MOT magnetic field is switched off and the three upper laser beams are red-detuned against the lower ones. This results in a so-called optical molasses and accelerates the atoms toward the science chamber, until they have reached a specific velocity, where the upper and lower beam triplets have the same frequency in the moving reference frame of the atoms. By choosing the right detuning, the launch velocity and thus the turning point of the atom cloud can be placed precisely at the position of the resonator. Even though the atom clouds that arrive at the resonator contain $\sim 10^8$ atoms, only several atoms per launch will get close enough to the resonator to couple to the evanescent field. In order to maximize the interaction cross section between the cloud and the resonator, the latter was tilted about 20° with respect to the line of sight between the MOT and resonator (see Fig. 3.1).

The fact that the atoms are not trapped near the resonator surface but pass by in free fall limits this experiment. As we will see later, atoms couple strongly to the evanescent field for only a few $\mu$s. This gives the time frame in which detection, atomic state preparation

and manipulation have to take place.

## 3.2   Laser system and fiber network

The experiment employs several laser systems, two providing the laser light for the MOT including the repump laser, while the third is used for frequency and distance stabilization of the resonator as well as detection and probing. Since they are set up on a different optical table as the vacuum chamber, these laser beams are coupled into polarization maintaining fibers and then guided to the experiment. In this section, I will focus on the detection and probing part, since the MOT is already working properly and is not subject to any modification. In the current setup, the light from the laser table, which is locked to the specific rubidium absorption line, is injected into a fiber network. This network provides a highly flexible distribution of the laser light and seems to be the natural choice for our fiber-based resonator system. A schematic of the fiber network, used for this experiment, is shown in Fig. 3.2. Four laser beams enter the network, which is connected to one of the two coupling fibers. Two of these beams are responsible for locking the resonator to the frequency of the desired rubidium transition and stabilize the fiber-to-resonator distance. After passing a fiber bench (FB) to adjust the polarization, the light is sent onto the resonator and the remaining transmission is monitored using an avalanche photo diode (APD). A MEM switch is used to prevent the quite intense stabilization light to hit the single photon counting modules (SPCM), to avoid any damage of the SPCMs during the stabilization sequence. These SPCMs are avalanche photo diodes in Geiger mode and are used to monitor the atom-resonator system on a single atom level. The light for detecting the presence of atoms and the light for performing experiment with the coupled atom-resonator system have to be attenuated by several 99/1 beam splitters. Since they have to be switched on and off very fast whenever an atom is detected, they are sent through a Mach-Zehnder modulator. These modulators provide ultra-fast switching, operating at a modulation rate of $\sim$20 GHz, with moderate optical extinction of 30 dB. The polarization in both arms is matched using fiber polarization controllers (FPC). After combining the two beams, an additional polarization filter and two wave plates, placed in the FB, can be used to simultaneously adjust both polarizations, before they are sent onto the resonator. During the experimental phase of the sequence, the detection and probe light that passes the resonator is directed to the SPCMs. In addition to the first, a second coupling fiber is mounted inside the vacuum chamber. A similar setting, including a polarization controller, an APD and a SPCM pair, enables us to perform experiments with two fibers coupled to the resonator.
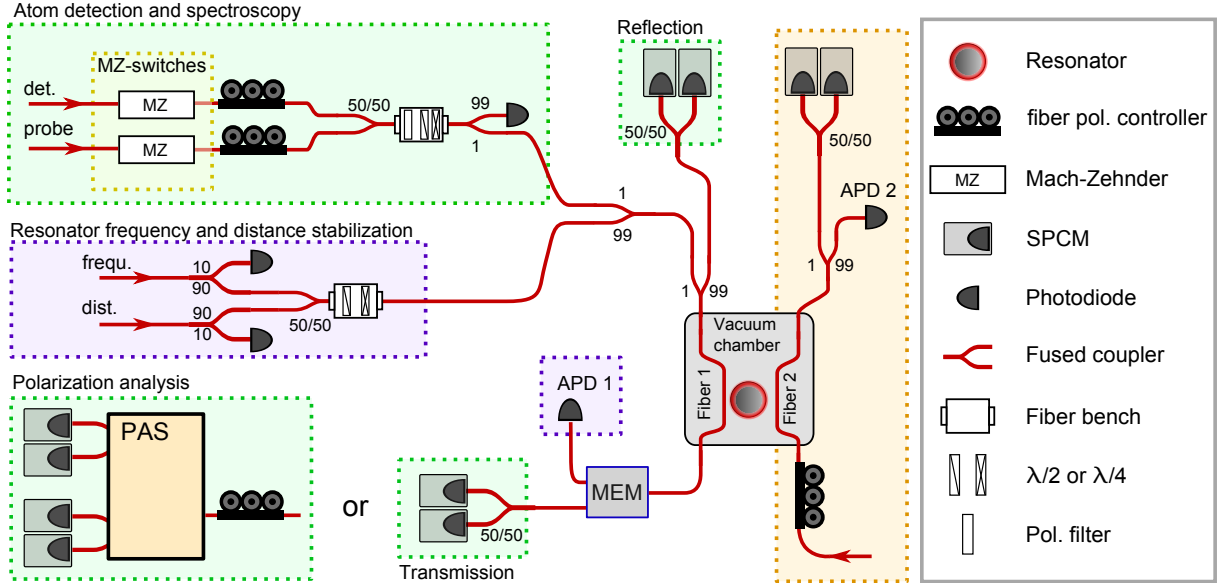
**Figure 3.2:** Optical fiber network: The colored boxes indicate the task, which is performed by the respective components. The purple box marks the setup employed for distance and frequency stabilization of the resonator. Green indicates the components involved in the atom detection and probing scheme. The Mach-Zehnder modulators (yellow), which are used for fast switching, might be replaced by the AOM setup, as discussed in chapter 5.2. For atom detection, the optical signal is either detected by two SPCMs in Hanbury-Brown and Twiss configuration or the polarization analysis setup (PAS) that is described in section 4.2. For certain measurements, a second fiber with its own polarization and detection units is employed (orange box) .

## 3.3   Atom detection and preparation

The atoms are delivered to the resonator by launching a cloud of cold atoms toward it. During the ~85 ms, in which the cloud is in the vicinity of the resonator, several atoms get close enough to couple for a few $\mu$s to the resonator mode. But, it is not possible to predict when a single atom arrives in the evanescent field. Thus, an active detection scheme is applied, capable of detecting the presence of an atom in real time. In this section, the standard detection scheme used for the previous experiments, is discussed. In chapter 4, a new scheme, based on the change the of light's polarization that occurs when light couples into and out of the resonator, will be introduced. Nevertheless, most techniques introduced here can be adapted for the new scheme.

The standard detection scheme works at critical coupling, where, on resonance, all the light send through the coupling fiber is coupled into the resonator and is dissipated therein. Thus, the single photon counters, that continuously monitor the transmission of the coupling fiber, detect no light (0.1 photon /$\mu$s). As we have seen in section 2.2, the presence of an atom drastically increases the fiber transmission. If the number of photons, detected by the SPCMs within a time window of 1.2 $\mu$s, exceeds a certain threshold value $n_{1st}$ (7 photons per 1.2 $\mu$s), the field programmable gate array (FPGA) based control system gen-
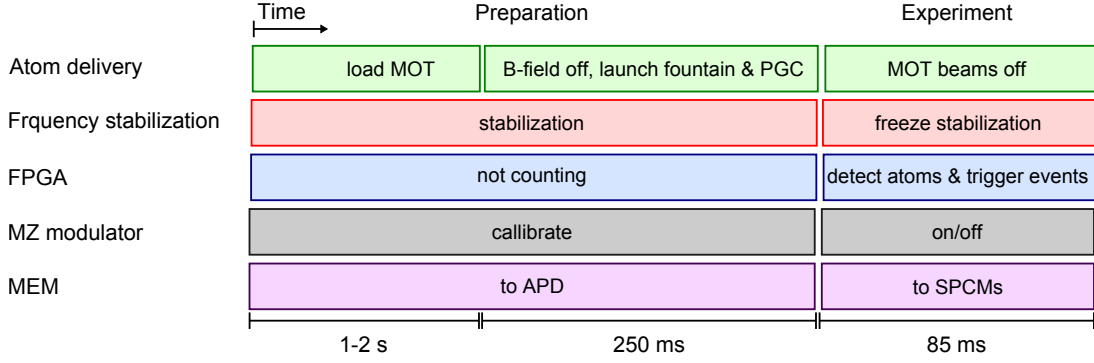
**Figure 3.3:** Time line of the experimental sequence. The sequence can be dividend into a preparation and experiment phase. First, all stabilization and characterization processes, as well as the atom preparation and delivery are performed. During the experiment phase, the cloud is in the immediate vicinity of the resonator and the FPGA scans for possible coupling events. This sequence can be repeated continuously for many hours.

erates a trigger, announcing a coupling event. Following this trigger, the Mach-Zehnder modulators are used to turn off the detection light and to switch on the probe light. To make sure that the atom was present during the whole probing phase, the detection light is turned on a second time after 1 $\mu$s. If the SPCMs do not detect a certain number of photons $n_{2nd}$ within the next $\mu$s, we conclude that the atom has left the evanescent field or that it crashed into the resonator during the probing time and the event is discarded. For those events kept, the detected photos are time tagged and the information is saved.

A nice side effect of the detection process occurs when we detect atoms using TM-polarized light. In section 2.2 we have learned that modes of certain polarization can drive transitions between different $m_F$ states, leading to optical pumping. When an atom absorbs a photon of TM$^-$ (TM$^+$) polarization it gets excited to a state with $\Delta m_F=-1$ ($\Delta m_F=1$). The excited atom might emit into the orthogonal TM$^+$ (TM$^-$) mode when decaying into its ground state. In such a process the atom changes its Zeeman sub-level by $\Delta m_F=-2$ ($\Delta m_F=2$). After undergoing a few such scattering events, even atoms initially in the opposite Zeeman state $m_F=3$ ($m_F=-3$) will end up in the outermost $m_F=-3$ ($m_F=3$) state. Thus, performing the detection with the right polarization already prepares the atom in a well-defined state.

## 3.4 Experimental sequence

The course of the experimental sequence is controlled by the control center software, triggering and operating most of the steps discussed before. One cycle of the control sequence is schematically shown in Fig. 3.3. Each cycle starts by performing all required stabilizations and calibrations. Simultaneously, the MOT is loaded. When the atomic fountain
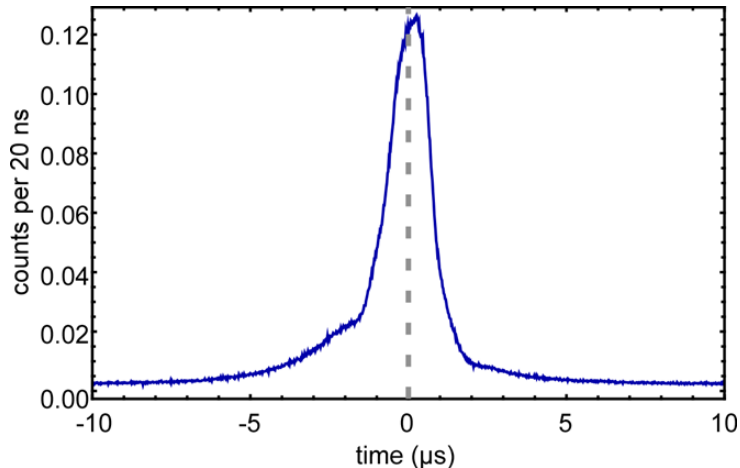
**Figure 3.4:** Continuous time-traces of 1,518,023 atom transits, where all traces are aligned so that the mean photon arrival time is at $t = 0$. The photon distribution has a FWHM of 1.6 $\mu$s. Adapted from [19].

is launched, the MOT coils are turned off. After the atoms have left the cooling beams, all lasers associated with the MOT are turned off using acousto optical modulators and mechanical shutters to prevent any stray light from disturbing the measurements. A few milliseconds before the atom cloud reaches the resonator, the frequency stabilization is frozen and the stabilization light is turned off. The frequency stabilization also includes a feed forward control to correct thermal drifts, which occur after turning off the stabilization light. Then, the MEM-switch is set to route the light that passes the resonator toward the SPCMs which are now gated. As the cloud reaches the resonator, the FPGA starts counting photons and searches for coupling events. When an atom is detected the FPGA triggers the probe sequence. After 85 ms, all atoms have left the interaction zone and the sequence can be started again. To assure a constant fiber-resonator coupling, the sequence is stopped every one hundred runs and a distance stabilization is performed. Afterward, the sequence is continued.

## 3.5 Recent experimental results

As we have seen in section 2.2, the transmission through the coupling fiber significantly changes when an atom couples to the resonator mode. This is realized by tuning the resonator and the light resonant with the $F{=}3{\rightarrow}F'{=}4$ transition of rubidium 85. When monitoring the fiber transmission, the presence of an atom in the evanescent field of a critically coupled resonator can be heralded. Figure 3.4 shows the detected photon distribution during the atomic transit. From this, we can infer an average atom-cavity interaction time, given by a FWHM of 1.6 $\mu$s. By actively detecting coupled atoms and carrying out spectroscopy on the coupled atom-resonator system, it is possible to measure
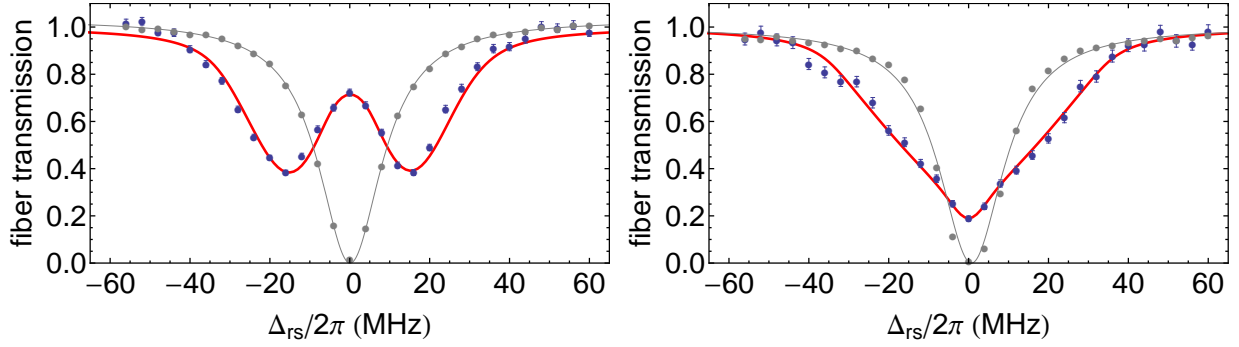
**Figure 3.5:** Measured fiber transmission spectrum for a TM and a TE mode coupled to a single atom (blue). The gray data shows the transmission of an empty resonator. For the TM mode the two peak splitting is well resolved, while the three peak spectrum for the TE mode is almost not visible, due to the broad distribution of coupling strength $g$. The red solid lines are theoretical fits, which are in excellent agreement with the measurements. Adapted from [18].

Rabi spectra. The well resolved peaks in Fig. 3.5 only occur in the regime where $g \gg \kappa, \gamma$, known as strong coupling. This finally proves that the experimental apparatus is capable of strongly coupling single atoms to a resonator mode. Furthermore, the different spectra taken for the two polarizations TE and TM, demonstrate the validity of the theory that was discussed in chapter 2.2. Comparing the measurement with the theoretical predictions allows to determine basic properties of our atom-resonator system, such as the coupling strength. Fitting the data yields an average coupling strength of $g/2\pi = 17$ MHz, with a standard deviation of $\sigma_g/2\pi = 6$ MHz for the TM-polarized mode [18].

**Fiber-optical switch**

Recently a "classical" optical switch operated by a single atom was realized with our experimental setup. For this purpose, the resonator was interfaced by two coupling fibers in add-drop configuration (see Fig. 3.6a). The so-called drop fiber introduces additional losses and, thus, the bus fiber has to be moved closer to the resonator to achieve critical-coupling, which is required for detecting coupling events. Nevertheless, the atom-resonator system still reaches the strong coupling regime. Initially, the distance between the two fibers and the resonator is adjusted such that all light sent into the bus-fiber couples into the resonator and a large fraction is transferred to the output port of a second fiber (drop-fiber), where it is detected by a single photon counter (SPCM). Now, if an atom couples to the evanescent field, it causes the resonance frequency of the coupled atom-resonator system to change and prevents the light from coupling into the resonator. The light thus stays in the bus-fiber where it is detected by an SPCM. The presence or absence of an atom thus regulates the flow of light between bus- and drop-fiber. In Fig. 3.6b the measured transmission through the two coupling fibers as a function of the cavity decay rate, which can be controlled by changing the distance between the resonator and the
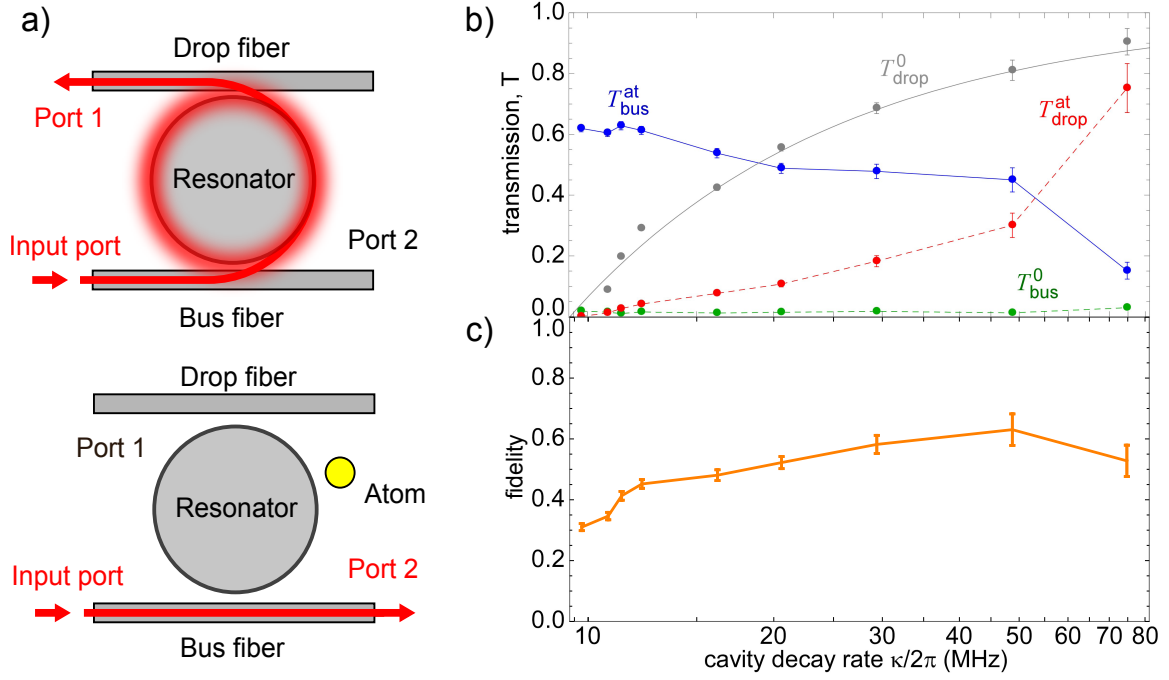
**Figure 3.6:** a) Simplified experimental setup of the four-port optical switch. The presence or absence of an atom coupled to the evanescent field regulates the flow of light between bus- and drop-fiber. b) The measured transmission of the bus- and drop-fiber with ($T_{bus}^0$ and $T_{drop}^0$) and without an atom present ($T_{bus}^{at}$ and $T_{drop}^{at}$), as a function of the cavity decay rate. c) Fidelity of the switch operation $\mathcal{F} = (T_{bus}^{at} + T_{drop}^0)/2$, calculated from the data shown in a). Adapted from [19].

drop fiber, is plotted. From this, the probability that a single input photon will be routed into the correct fiber port (including all possible loss channels) has been calculated, giving a fidelity of $\mathcal{F} = 0.62$ (see Fig. 3.6c). At the same time, there is a 79% probability to recover an incident photon after the switching operation.

This demonstration of highly efficient switching of an optical signal, mediated by the presence of a single atom, is an important result toward one of the main goals of this experiment: a macroscopic superposition states of the light fields in two different output ports. This is the quantum mechanical analogon to a fiber optical switch, a so-called quantum switch. Such a switch might be realized using the setup described before (see Fig. 3.7), by introducing an atomic state ($F{=}2$) that is off resonate with the cavity. As long as the atom is in the $F{=}3$ state, it couples to the resonator field and due to the shift of the resonance of the combined atom-resonator system, the light cannot enter the resonator and the optical signal is routed to output port 1. By transferring the atom into the $F{=}2$ state, the coupling between the atom and the resonator can be switched off. Thus, the light can enter the resonator and will then exit through the second fiber. This routes the photons to the other output port 2.

By preparing the atom in a coherent superposition, such as $\frac{1}{\sqrt{2}}(|F{=}3\rangle + |F{=}2\rangle)$ and
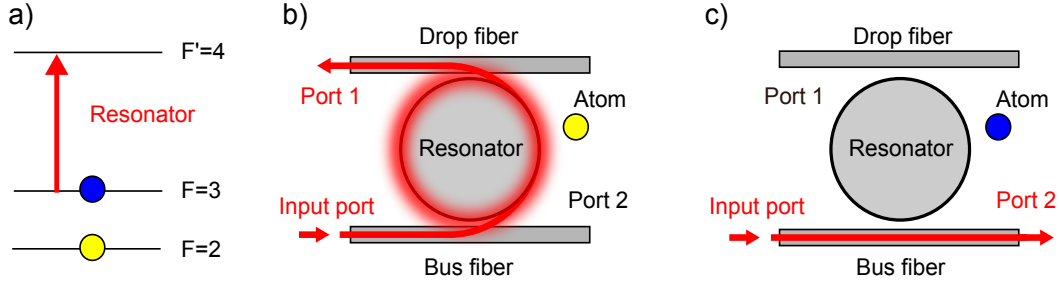
**Figure 3.7:** a) Simplified level scheme of $^{85}$Rb. The rubidium atom can be prepared in the $F=2$ or $F=3$ hyperfine ground states. The resonator is resonant to the $F=3 \to F'=4$ transition (red arrow). b) Possible realization of a quantum switch using a bottle microresonator in add-drop configuration. If the atom is in the $F=2$ ground state, the coupling rate between the atom and the resonator mode is zero. In this case, the input light couples into the resonator and is transferred to output port 1. c) If the atom is in the F=3 state, it strongly couples to the bottle mode. The resonance frequencies of the strongly coupled atom-resonator system changes, thus preventing the light from entering the resonator. Thus, all the light is transmitted to port 2.

sending light through the coupling fiber, will ideally generate an entangled superposition state

$$\frac{1}{\sqrt{2}}(|F{=}3\rangle\,|\alpha_1\rangle + |F{=}2\rangle\,|\alpha_2\rangle)\ , \tag{3.1}$$

where $|\alpha_1\rangle$ and $|\alpha_2\rangle$ denote the macroscopically distinct output fields. According to the famous gedankenexperiment by Erwin Schrödinger [21], states as Eq. (3.1), where a small quantum system (single atom) is entangled with a macroscopic system (light pulse containing a variable number of photons), are called Schrödinger cat states [21]. Such states have very different properties compared to classical mixtures, which makes them interesting for, e.g., quantum mechanical enhanced measurements [41], where quantum mechanical phenomena are employed to realize more precise measurements than can be achieved classically. In addition a switch that preserves the quantum state of an optical signal, might also be used for the realization of a future quantum network [42].

# Chapter 4

# Polarization detection and switching

One of the main goals of this experiment is to create a Schrödinger-cat-like state by entangling a two-level quantum system, realized using a single atom, with a "macroscopic" classical light pulse, consisting of a variable mean number of photons. A first step toward this goal is to generate entanglement between a single atom and a single photon. To verify the atom-photon entanglement, one has to show that the two particle quantum system cannot be in a classical mixture of separable states. This task is closely related to a violation of Bell's inequality [43] and requires correlated state measurements of the atom and the photon in complementary bases (as has been done in [44, 45]). For the present switching technique which employs two coupling fibers, this is not trivial since the switching process routes the light into two different fiber outputs. A possibility to simplify the verification of entanglement would be to switch the polarization of the light instead of its propagation direction. For polarization states, a change of basis can easily be achieved with wave plates. At the same time, a transformation between polarization and spatial degree of freedom can easily be realized using a polarizing beam splitter.

In the following, a new atom-resonator interrogation scheme, based on polarization change introduced by the resonator, is presented. This will enable us to perform conditional measurements without the effort of setting up an additional interferometer. Since the experiment discussed here only needs one coupling fiber, the spare one might be employed for other tasks, such as coupling manipulation or trap fields into the resonator.

## 4.1   Basic idea

According to Eq. (2.30), light coupled from the fiber into the resonator and then back into the fiber is phase-shifted by $\phi_{g=0} = \text{Arg}(\langle \hat{a}_{g=0} \rangle)$ with respect to the initial beam. On resonance and with no atom present $\phi_{g=0} = \pi$. This sign change of the field leads to destructive interference and thus reduces the transmission through the coupling fiber.

Thus, this phase shift of $\pi$ is also responsible for the zero transmission when the resonator is critically coupled to the coupling fiber. Adding an atom which is coupled to the evanescent field causes a significant change of the phase of the resonator field.

If we consider the case where the atom interacts exclusively with a single mode, which is a good approximation for the case when we drive TM modes, as we have seen in chapter 2.2, we can analytically calculate the corresponding phase of the resonator mode. However, in our experiment, we do not directly access the intraresonator light field, but we can examine the light in the coupling fiber. The field in the fiber is the sum of the original light field that stayed in the fiber and the light leaking out of the resonator and its complex amplitude is given by $\langle a_{out} \rangle = \epsilon - i\sqrt{2\kappa_e}\langle a \rangle$ (according to Eq. (2.30)). Thus, the phase can be written as

$$\tan\phi = \frac{2\kappa_b(\Delta_{LC}(\gamma^2 + \Delta_{LA}^2) - g^2\Delta_{LA})}{g^4 + 2g^2(\gamma\kappa_0 - \Delta_{LA}\Delta_{LC}) + (\gamma^2 + \Delta_{LA}^2)(\Delta_{LC}^2 + \kappa_0^2 - \kappa_e^2)} \ . \tag{4.1}$$

In Fig 4.1 the transmission and the phase as a function of the atom-light detuning is given for several coupling rates $\kappa_e$. In the under-coupled regime, where $\kappa_e < \kappa_0$, the effect of the resonator is weak, since only a small amount of light couples into the resonator. The field in the fiber is dominated by the incoming light and thus the phase difference on resonance is zero. This only changes when we over-couple our resonator ($\kappa_e > \kappa_0$), where on resonance and without an atom, the light that couples out of the resonator dominates, thus causing a phase of $\pi$. The presence of an atom prevents most of the light to couple into the resonator, which causes a phase difference of $\pi$, with respect to the case without atom. If we further over-couple the resonator, more light couples into the resonator, even though the atom is present and is dissipated by the coupled atom-resonator system. This can be seen by the continuous decrease of the on-resonant transmission (see Fig. 4.2), while the phase stays the same (see Fig. 4.3). At the same time, the transmission without an atom present increases. For

$$\kappa_c^{(a)} = \kappa_0 + \frac{g^2}{\gamma} \ , \tag{4.2}$$

we reach a point where the combined system of atom and resonator is critically coupled to the fiber. As a consequence, all light is coupled into the resonator and dissipated therein. Thus, the transmission in the presence of an atom becomes zero. The first term of Eq. (4.2) corresponds to the losses introduced by the resonator. The second describes the loss rate introduced by the atom, which is given by the product of the excited state population per intraresonator photon in the weak driving limit $g^2/\gamma^2$, multiplied by the atom decay rate $\gamma$. When neglecting the intrinsic resonator losses, this "critical atom coupling" occurs when the cooperativity $C = g^2/\kappa\gamma$ becomes one, meaning that for $\kappa_e > \kappa_c^{(a)}$ the effect
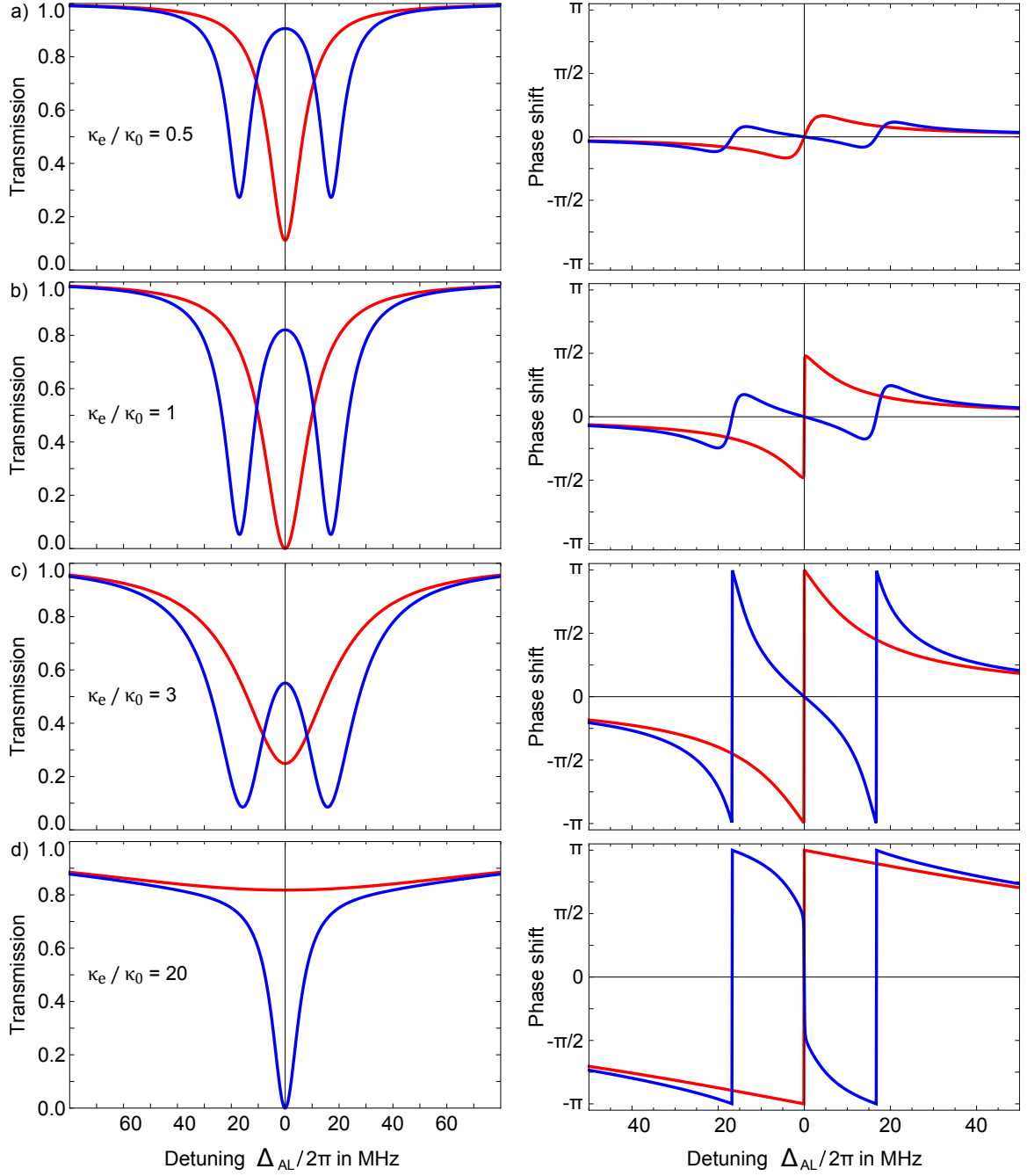
**Figure 4.1:** Normalized transmission $T = |\langle a_{out}\rangle|^2/|\epsilon|^2$ and phase shift of the light transmitted through the fiber, as a function of the laser-atom detuning $\Delta_{AL}$, for several coupling constants $\kappa_e$, ranging from the under-coupled (a), over critical coupled (b), to the over-coupled regime (c) and finally coming to the "critical atom coupling" in (d). The red curves correspond to the case when no atom couples to the resonator ($g = 0$) and the blue to the case with an atom coupled to the resonator ($g = 2\pi \cdot 17$ MHz). These plots have been calculated for $(\Delta_{AC}, \gamma, \kappa_0) = 2\pi(0, 3, 5)$ MHz and $\kappa_e/\kappa_0 = (0.5, 1, 3, 20)$. When using Eq. (4.1) for calculating the argument of the light amplitude, one has to take into account that the real part can get negative and extend the domain of definition of the arctangent.
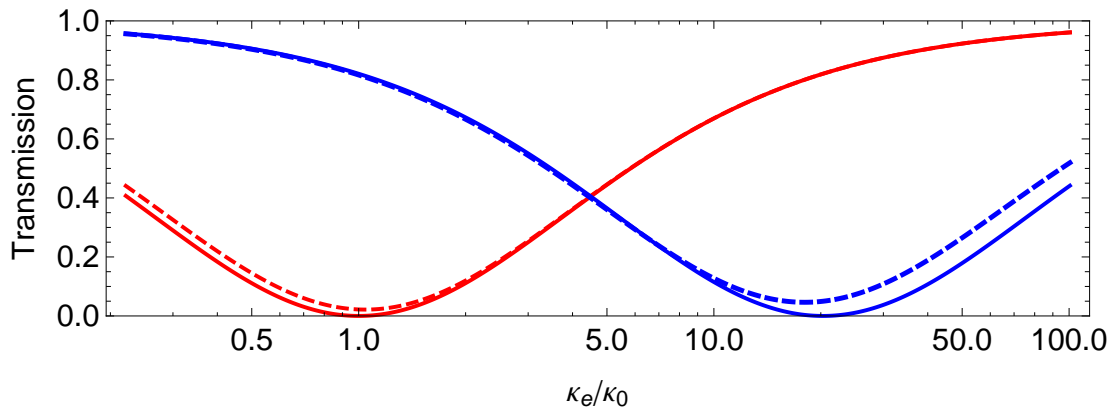
**Figure 4.2:** Coupling Fiber transmission, with (blue) and without (red) an atom coupling to the evanescent field of the resonator, as a function of the coupling rate $\kappa_e$, depicted with a logarithmic $x$-axis. The solid curves are calculated for $(g, \Delta, \gamma, \kappa_0) = 2\pi(17, 0, 3, 5)$ MHz. The transmission curve, without an atom present, becomes zero for critical coupling $\kappa_e/\kappa_0 = 1$, where all light that couples into the resonator is dissipated by the resonator losses. For the case when an atom couples to the resonator, the transmission becomes zero for $\kappa_e/\kappa_0 = g^2/\gamma\kappa_0 + 1 \approx 20$. At this point all the light is coupled into the resonator, even though the atom is present and dissipated due to the losses introduced by both, the atom and the resonator. If the laser is slightly detuned by $\gamma/2$ with respect to the cavity and the resonator, the transmission will not drop to exactly zero for the two critical couplings (dashed lines).

of the atom on the resonator becomes negligible. Up to this point, all the light that couples into the resonator is dissipated. For $\kappa_e > \kappa_c^{(a)}$ light that exits the resonator again dominates the field in the fiber. This light exhibits a phase of $\pi$ and thus the relative phase shift, with respect to the case without an atom, becomes zero. The behavior of the phase change between the case with and without atom as a function of $\kappa_e$ can be summarized as

$$\Delta\phi(\kappa_e) = \phi_{g=0} - \phi_{g\neq0} = \begin{cases} 0 & \kappa_e \leq \kappa_c^{(r)} = \kappa_0 \\ \pi & \kappa_e > \kappa_c^{(r)} \\ 0 & \kappa_e > \kappa_c^{(a)} \end{cases}$$

Slightly detuning the laser light with respect to both resonator and atom gives essentially the same behavior but with a more gradual change of phase at $\kappa_c^{(r)}$ and $\kappa_c^{(a)}$, as indicated in Fig. 4.2 and 4.3. We are interested in measuring the phase change $\Delta\phi$ in order to herald the presence of an atom coupled to the resonator. This should be possible in the intermediate region $\kappa_0 < \kappa_e < \kappa_c^{(a)} = g^2/\gamma + \kappa_0$.

In order to measure this phase shift one has to compare the light that probes the coupled atom-resonator system with a reference signal using homodyne detection. This can be realized by sending in a second polarization that does not couple to the resonator through
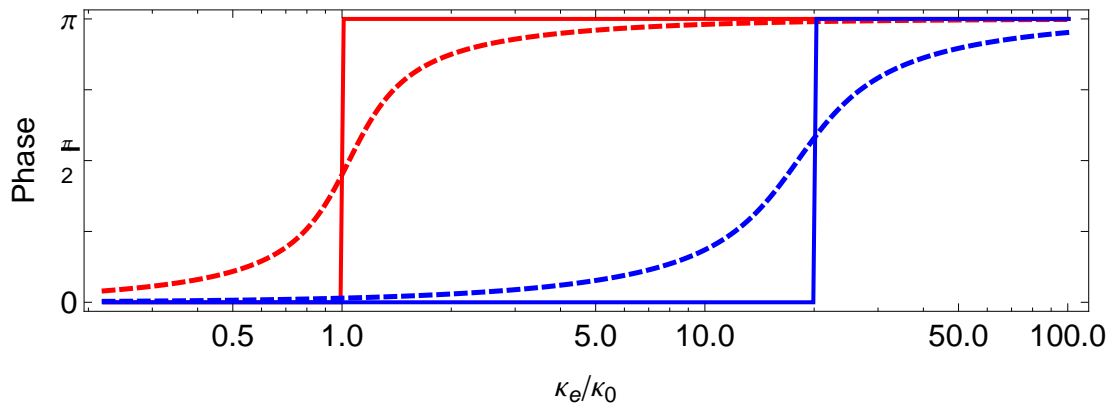
**Figure 4.3:** Phase of the transmitted field, with (blue) and without (red) an atom coupling to the evanescent field of the resonator, as a function of the coupling rate $\kappa_e$, plotted with a logarithmic $x$-axis, for the same parameters as Fig. 4.2. The phase difference with respect to the incoming light is introduced by coupling into and out of the resonator. If no atom is present, this effect can be observed for $\kappa_e > \kappa_0$. The presence of an atom prevents the light to efficiently couple into the resonator. Only if the linewidth of the resonator becomes very broad, i.e., if $\kappa_e$ is very large, more light couples into the resonator and, for $\kappa_e > g^2/\gamma + \kappa_0$, light also returns back into the coupling fiber, causing the phase to change. We are interested in the phase difference between the two cases in order to herald the presence of an atom coupled to the resonator via a phase measurement. This should work in the region $\kappa_0 < \kappa_e < g^2/\gamma + \kappa_0$. If the laser is slightly detuned by $\gamma/2$ with respect to the cavity and the resonator, the change of phase at $\kappa_c^{(r)}$ and $\kappa_c^{(a)}$ becomes more gradual (dashed lines).

the fiber. Since the bottle resonator is highly birefringent, the resonance frequencies for TM and TE modes differ by several GHz. Thus, only one polarization will be affected by the resonator, while the other can serve as a reference for the phase measurement. In our experiment, we want the TM mode of the resonator to interact with the atom and thus refer to the polarization component that couples to the resonator as $|\mathrm{TM}\rangle$, while the reference field that does not interact with the resonator will be refereed to as $|\mathrm{TE}\rangle$. When sending a superposition of both polarization components $|E_{in}\rangle = \alpha\,|\mathrm{TM}\rangle - \beta\,|\mathrm{TE}\rangle$ through the coupling fiber, the presence of an atom will only introduce a phase change in one component and thus cause a rotation of the total polarization vector of the light in the fiber, as schematically illustrated in Fig. 4.4. Such a rotation can easily be measured using a polarization analyzing setup consisting, e.g., of a polarizing beam splitter.

Before coming to the realization of the above scheme, I will now briefly discuss the modifications on the experimental apparatus that are required for such measurements.
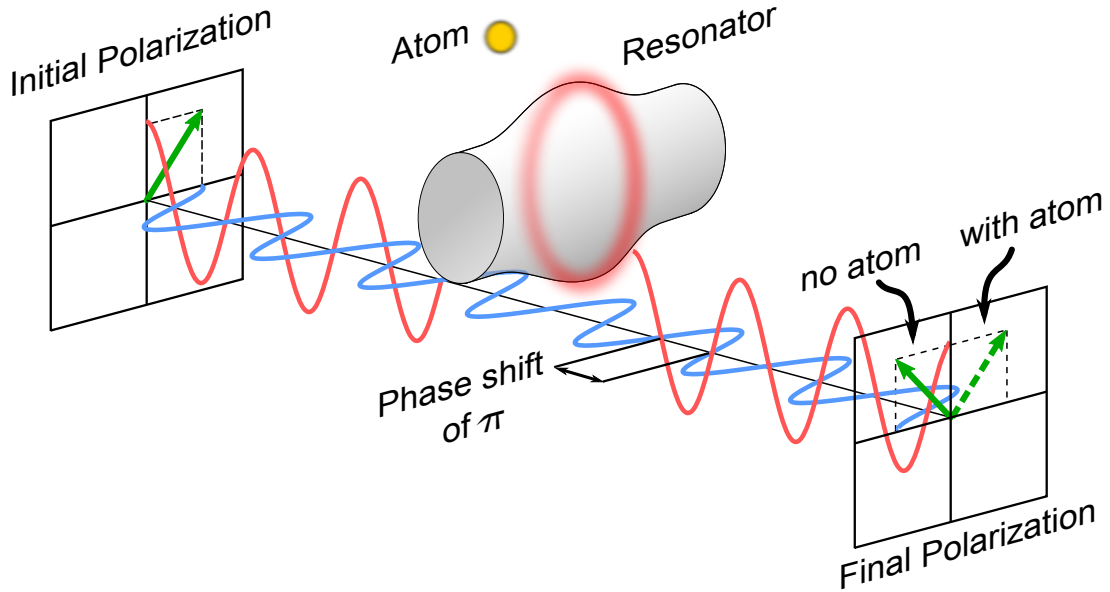
**Figure 4.4:** Visualization of the new atom-resonator interrogation scheme. The incoming light has two polarization components, a horizontal (blue) that does not couple to the resonator and a second vertical component that is resonant with the resonator (red). As long as no atom is present the resonator causes a phase shift of $\pi$ and, thus, a rotation of the polarization vector, compared to the initial polarization. When an atom enters the resonator mode, the light cannot enter the resonator and no phase shift occurs. By measuring the change of the final polarization, one can thus herald the presence of an atom in the evanescent field of the resonator.

## 4.2 Polarization analyzer setup

In our experiment, atoms are not trapped in the resonator field. They stochastically transit the evanescent field when a cloud of cold atoms reaches the resonator. Thus, we have to actively detect the presence of a strongly coupled atom. Up to now, this has been done by monitoring the transmission of the coupling fiber which was set to critical coupling. Now, we want to employ the new interrogation scheme introduced in the preceding section, where the presence of the atom coupled to an over-coupled resonator causes a change of phase of a certain polarization component. In combination with a second reference polarization, this phase shift becomes measurable as a rotation of the total polarization. Sending the output light onto a polarizing beam splitter (PBS) which separates two orthogonal linear polarizations will cause a redistribution of the light in the two outputs. But as we have seen for the previous detection scheme, a single atom transit causes the transmission of a few tens of photons. Photon statistics imposes fluctuations of the photon number that scale with the square root of the photon number, known as shot noise. In order to minimize false triggers due to photon noise, we need an initially dark port for detecting atoms that couple to the resonator. In the scheme considered here, a port with zero transmission can easily be realized by properly adjusting the polarization
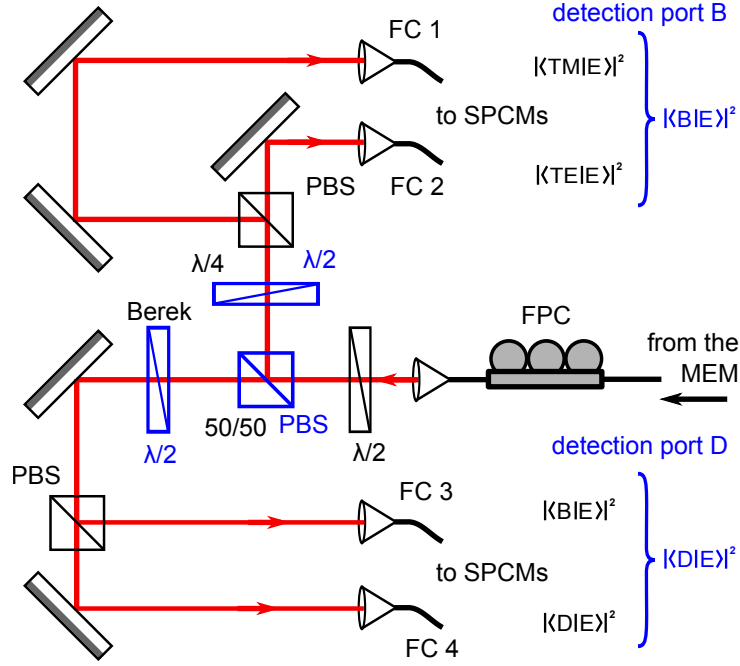
**Figure 4.5:** Schematic of the optical setup used as a polarization analyzer. In this illustration, two different settings used for measuring in one or two basis are shown. The components that have to be interchanged are marked in blue. For measuring in two basis simultaneously, the light is first split in two arms by 50/50 beam splitter. One arm is used to measure the $|D\rangle$ and $|B\rangle$ component, which are used for detecting atoms, while the other can be adjusted to measure, e.g. in the resonator basis $|TM\rangle$-$|TE\rangle$. For the measurements described in chapter 4, the components marked in blue are replaced with a PBS and two half wave plates. Thus, the polarization analysis is performed by the first PBS, while the other two in combination with half wave plates, are used as variable beam splitters. This is done to get an higher count rate for the first proof-of-principle measurements. The expressions right of the fiber couplers correspond to the polarization component measured by the respective SPCMs, after the incoming field $|E\rangle$ has passed the analyzer setup.

of the transmitted light that reaches the PBS. This is possible even for a non-critically coupled resonator.

For the experiment, we have designed a polarization analyzer setup capable of measuring the polarization of the transmitted light in two different bases, as illustrated in Fig 4.5. This setup is connected to one output of the MEM switch (see Fig. 3.2). First, the beam has to be divided by a 50/50 beam splitter. One branch can be used to monitor, for example, the projection of the transmitted field onto the resonator basis vectors $|TM\rangle$ and $|TE\rangle$. This can be achieved by proper adjustment of the fiber polarization controller (FPC) and quarter wave plate, while no atom is present. The other branch has to be used for detecting the presence of atoms, which requires an initially dark $|D\rangle$ port. The second port is accordingly referred to as bright port $|B\rangle$. When scanning the ratio of the incoming polarization components or the fiber-resonator distance, the detection basis will change as well. Thus the polarization encountering the PBS, in the branch used for

detection, has to be adapted to give a dark port. In order to avoid simultaneous read-justment of the second basis ($|TM\rangle$-$|TE\rangle$), a Berek compensator is placed in front of the PBS. Such a Berek compensator corresponds too a variable wave plate and can thus be used to transform any given input polarization into any desired output polarization. It can thus be used to get zero transmission in the detection port. Each branch (1,2,3,4) corresponds to the projection onto a certain base vector ($|TE\rangle$, $|TM\rangle$, $|B\rangle$, $|D\rangle$). After passing the PBS, all four beams are coupled into multimode fibers, which are connected to single photon counters (SPCM).

Due to the 50/50 beam splitter, only half of the light can be used to detect atoms. For our first measurements which should be used to characterize the new interrogation method, we have decided to use all the light by only measuring in a single basis. This is easily realized by replacing the 50/50 beam splitter by a PBS (see blue components in Fig. 4.5, which is used to separate the two polarization components $|D\rangle$ and $|B\rangle$. The FPC is now used to generate the dark output. The second PBS in each branch, in combination with a half wave plate, is employed as variable beam splitter, that routes the photons of the respective projection onto two SPCMs. Using detectors in such a Hanbury-Brown and Twiss configuration halves the detection dead time and doubles the maximum detectable power.

The total coupling efficiency, i.e., the fraction of the incoming light that is collected by the four fiber couplers, has been determined to be 85%.

## 4.3   Atom detection

For the current experimental apparatus it is critical to efficiently detect the presence of an atom. For this reason, it is of great interest to know whether this new interrogation scheme yields a detection signal comparable to what was achieved using the standard scheme.

For the atom detection process, the presence of an atom in the resonator field should cause a maximal signal in the initially dark output port. This can be realized by critically coupling the resonator and by measuring the transmission change when an atom couples, as done in the standard detection scheme (see section 3.3). In this case, all light that is sent through the coupling fiber is affected by the interaction with the atom-resonator system, yielding the signal used for detection. For the new polarization based detection scheme, the dark detection port can be realized by adjusting the polarization analyzing setup accordingly. To access the phase change introduced by an atom, a second light beam with a polarization that does not couple to the resonator is also sent through the fiber. This field component, referred to as $|TE\rangle$, is not involved in the interaction process,
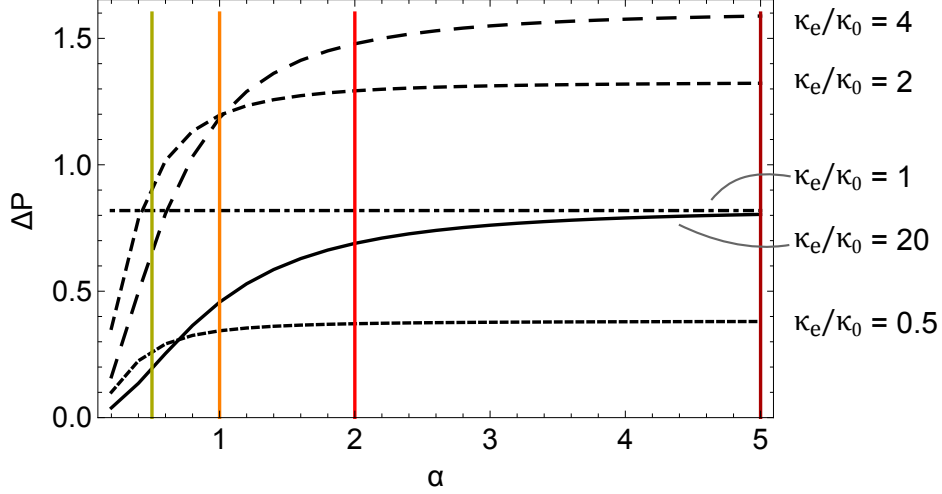
**Figure 4.6:** Detection signal, indicating the presence of an atom, as a function of the amplitude $\alpha$ of the non-coupling polarization component, normalized by the incoming light power, that has the right polarization to interact with the cavity. The different black lines correspond to different $\kappa_e/\kappa_0 = (0.5, 1, 2, 4, 20)$, while the global parameters were $(\Delta_{AC}, \gamma, \kappa_0) = 2\pi(0, 3, 5)$ MHz. The vertical lines indicate the correspondence to the curves in Fig. 4.7.
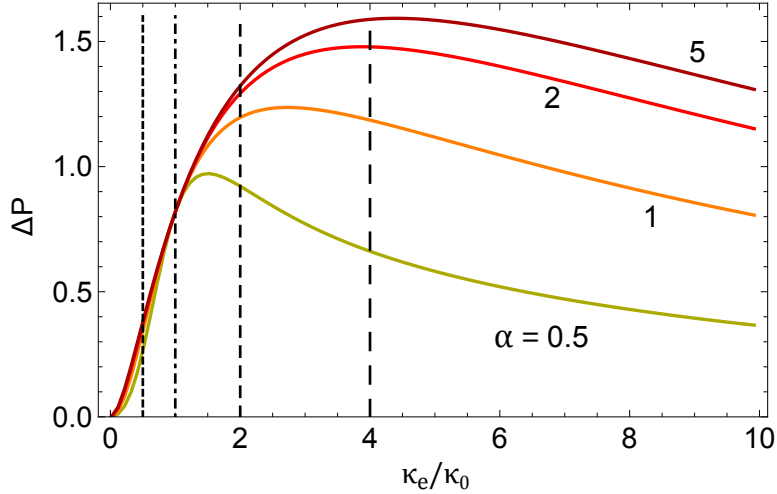


**Figure 4.7:** Detection signal, indicating the presence of an atom, as a function of the coupling rate $\kappa_e$, normalized by the incoming light power, that has the right polarization to interact with the cavity. The different curves correspond to different $\alpha = (0.5, 1, 2, 5)$, while the global parameters were $(\Delta_{AC}, \gamma, \kappa_0) = 2\pi(0, 3, 5)$ MHz. The vertical lines indicate the correspondence to the curves in Fig. 4.6.

but interferes with the $|\text{TM}\rangle$-light at the beam splitter and, thus, can be used to amplify of the detected signal. A larger signal per photon that interacts with the atom-resonator system would allow us to further reduce the intraresonator photon number or to detect the atoms earlier, leaving more time for probing and manipulation.

To get a quantitative predictions for the increase of the signal, we employ the theoretical model introduced in chapter 2.2. This can be used to calculate the light power $\Delta P$ at

the initially dark detection port for the case when an atom couples to the resonator as a function of the amplitude of the non-coupling polarization component $|\text{TE}\rangle$, while keeping the intraresonator photon number constant. The incoming field in the coupling fiber is given by the (non-normalized) vector

$$|E_{in}(\alpha)\rangle = \alpha\,|\text{TE}\rangle + |\text{TM}\rangle \ , \tag{4.3}$$

where we have introduced the amplitude $\alpha$ of the non-coupling polarization component, while the amplitude of the component that interacts with the resonator is set to one. The condition that one port of the polarization analyzer should receive zero power for an empty resonator, thus defines the detection basis as

$$|\text{B}\rangle = |E_{g=0}\rangle\,/|E_{g=0}| \quad \text{and} \quad |\text{D}\rangle \perp |\text{B}\rangle \ , \tag{4.4}$$

using the transmitted field without atom

$$|E_{g=0}\rangle = \alpha\,|\text{TE}\rangle + (1 + i\sqrt{2\kappa_e}\,\langle a\rangle_{g=0})\,|\text{TM}\rangle \ . \tag{4.5}$$

The detection power can be received by projecting the output field state, in the presence of an atom, $|E_{g\neq0}\rangle$, onto the dark basis $|\text{D}\rangle$ and then taking the modulus squared of the projection

$$\Delta P = \left| \langle\text{D}|\left(\alpha\,|\text{TE}\rangle + \left\{1 + i\sqrt{2\kappa_e}\,\langle a\rangle_{g\neq0}\right)\,|\text{TM}\rangle\right\}\right)\right|^2 . \tag{4.6}$$

On resonance ($\Delta_{LC} = \Delta_{AL} = 0$), this can be simplified to

$$\Delta P_{\Delta=0} = \frac{4g^4\kappa_e^2\alpha^2}{(\kappa_0 + \kappa_e)^2(g^2 + \gamma(\kappa_0 + \kappa_e))^2(\alpha^2 + ((\kappa_0 - \kappa_e)/(\kappa_0 + \kappa_e))^2} \tag{4.7}$$

In Fig. 4.6 $\Delta P_{\Delta=0}$ is plotted as a function of the non-coupling light amplitude $\alpha$, for different fiber-resonator coupling rates $\kappa_e$. In principle, we can identify four different cases: For a under-coupled resonator, even though no phase change occurs, the difference of the transmission with and without atom still gives a measurable signal on the detection port, which can be only slightly improved by increasing $\alpha$. For critical coupling, the dark state of the detection basis is always given by $|\text{TM}\rangle$ and the uncoupled component $|\text{TE}\rangle$ will not contribute to the signal, thus giving a constant value independent of $\alpha$. This case corresponds to the transmission change we would expect for the standard detection scheme and thus can be seen as a reference. When going into the over-coupled regime, the increase of $\alpha$ yields an amplification of the detection signal beyond the value at critical-coupling, which saturates for large $\alpha$. In Fig. 4.6, we can identify the maximum of $\Delta P_{\Delta=0}$

as the point where the transmission with and without an atom present is the same. The fiber-resonator coupling rate for this point is given by

$$\kappa_e = \sqrt{\kappa_0(g^2/\gamma + \kappa_0)} = \sqrt{\kappa_0 \kappa_c^{(a)}} \ . \tag{4.8}$$

When comparing this expression with Eq. (4.2), one finds that the point of equal transmission corresponds to the geometric mean of the coupling rates for critical resonator-coupling and the critical atom-coupling. For $\kappa_e > \kappa_c^{(a)}$ where the phase between the two polarization components becomes zero again, we only detect the change in transmission. Thus, even for large $\alpha$ the detection signal will not exceed the value at "normal" critical coupling. We can conclude that an amplification can only be achieved for $\kappa_c^{(r)} < \kappa_e < \kappa_c^{(a)}$. Nevertheless, this new scheme can also be applied for detecting atoms in a regime where no phase change and amplification occurs, albeit with low efficiency.

For parameters which are closer to the experiment, $(\Delta, g, \gamma, \kappa_0, \kappa_e) = 2\pi(0, 17, 3, 5, 15)$ MHz, already moderate power of $|\alpha|^2 \approx 4$ will increase the detection signal by a factor of 1.85, compared to the values received for the standard detection scheme.

As first prove-of-principles we chose a resonator mode that exhibits a linewidth of $\kappa_0/2\pi = 9$ MHz. The ratio of the light powers in the two polarization components before the resonator was coupled to the fiber was set to 2. This corresponds to $\alpha = \sqrt{2}$. The fiber-resonator distance is adjusted such that we are in the over-coupled regime and the remaining on-resonance transmission through the fiber without atom is 50%, corresponding to $\kappa_e/\kappa_0 = 1.7$. Using this setting promises a moderate amplification of the detection signal by a factor of $\sim 1.4$ without running the risk of saturating the single photon detectors. Finally, the detection port $|D\rangle$ of the PAS is minimized using the FPC (see Fig. 4.5).

For this detection scheme the standard FPGA-based detection sequence, described in chapter 3, can be employed (see also [46, 47] for a detailed discussion): In this scheme a double trigger method is used. The first trigger requires the number of detected photons within 1.2 $\mu$s to increase, from the background level of 0.1, to a value of $n_{1st} = 7$. When starting the sequence, we detect 10-20 of these events per launch, each corresponding to transmission traces, as shown in Fig. 4.8a. Averaging over many traces gives an averaged interaction time on the order of one microsecond (see in Fig. 4.8b). Even though this detection mechanism relies on polarization changes, Fig. 4.8b shows the same features that have been observed for the standard method (Fig. 3.4). When comparing the detection signal recorded here to an independent measurement on critical coupling (see [46]), we obtain an enhancement by a factor of 1.3, in good agreement with the theoretical predictions .
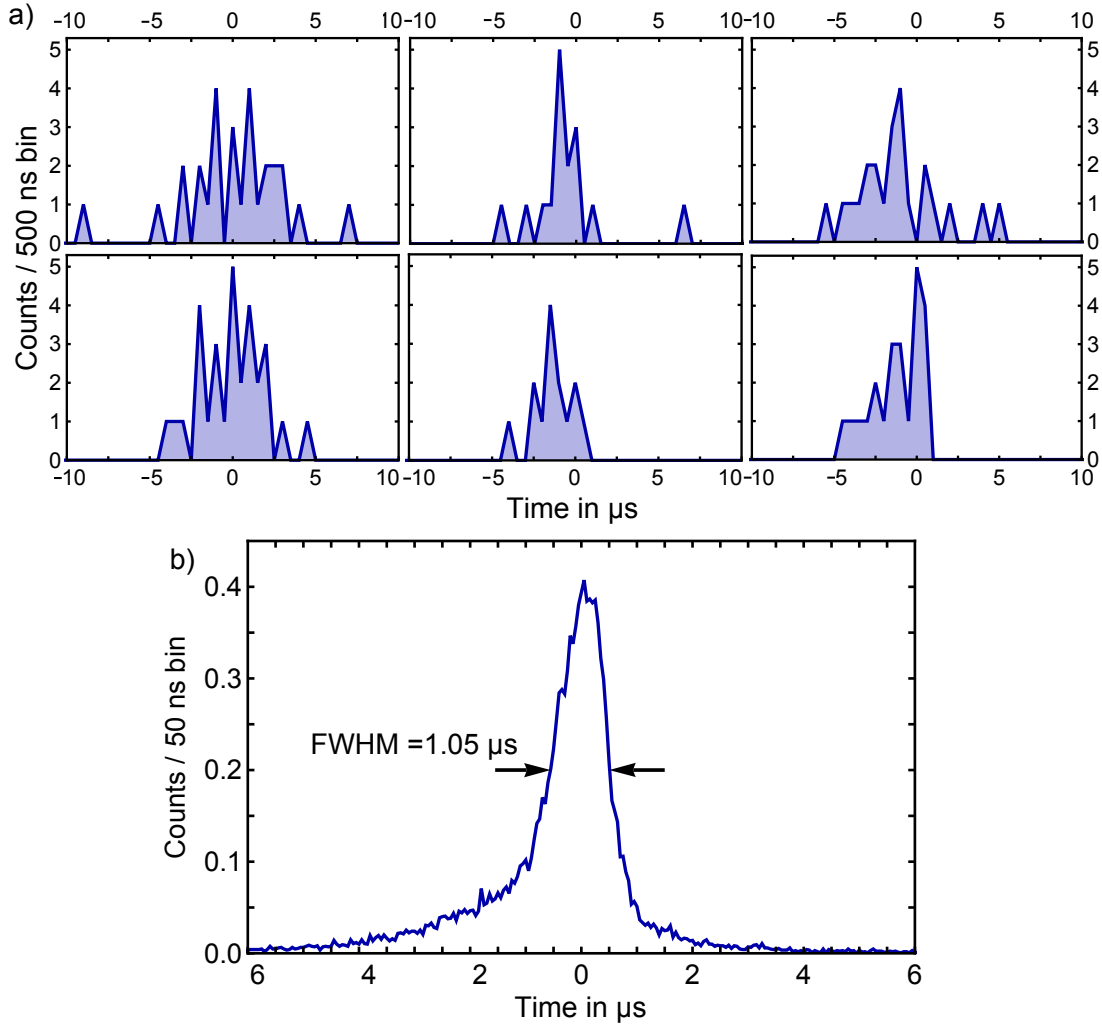
**Figure 4.8:** a) Typical transmission traces of single atom transits. b) Mean transmission averaged over 1699 atom transits such as depicted in a). The mean photon arrival time was shifted to be at t=0 for each atom transits. From this plot a mean atom life time of 1.05 $\mu$s can be deduced.

After successfully detecting a coupled atom, we might want to further probe the atom. However, as can be seen in Fig. 4.8, the interaction time is limited. For a given probing interval, there can be a large probability to loose the atom during the measurement, which could give rise to incorrect results. To ensure that we only take atoms into account that have stayed strongly coupled to the evanescent field over the whole probing time, we perform a second detection measurement after about one $\mu$s by launching the detection beam through the fiber for another microsecond. Only when the photons detected during the re-detection exceed a second threshold value $n_{2nd}$ the trace will be kept. In Fig. 4.9 the transmission is depicted as a function of time for different second threshold levels. The plots feature several prominent peaks that can be identified as detection artifacts, occurring because all measurements are aligned to the point in time when the first trigger criterium is fulfilled. Applying such a scheme yields a constant transmission during the
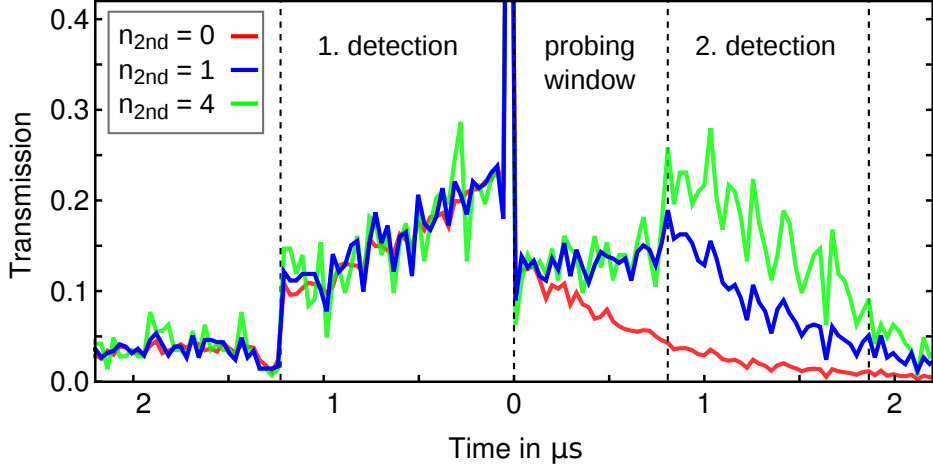
**Figure 4.9:** Normalized transmission for a typical detection sequence for varying threshold levels $n_{2nd}$. The prominent features of this plot can be identified as artifacts of the detection process. The significantly enhanced transmission at $t = 0$, is caused by the first trigger criterium. Since $t = 0$ marks the time when the seventh photon within 1.2 $\mu s$ was detected, there has to be a detection for each event. The sharp dip to almost zero transmission at $t = -1.2\,\mu s$ is there because, if a photon had been detected at this time, the FPGA would have triggered one time-bin earlier. As $n_{2nd}$ rises, a second peak follows at $t \sim 1\,\mu s$ caused by the re-detection. The second trigger ($n_{2nd} \geq 1$) produces an almost constant transmission during the measurement time window. The increase of $n_{2nd}$ has no effect on the transmission and only leads to an reduction of the valid traces, from 1699 (red) over 1145 (blue) to 431 (green).

two detections, independent of the second trigger value, as long as it is larger that one. This time interval will be referred to as probing window. Furthermore, using this double atom-detection scheme also drastically reduces the false first triggers, which can occur due to transmission noise.

This first measurements show that the new interrogation tool is also capable to actively detect single atoms coupling to the evanescent field of the resonator, which is crucial as long as we are not able to trap the atom in the vicinity of the resonator.

## 4.4 Switching and polarization rotation

As we have seen in the previous section, the new interrogation scheme is well suited for detecting single atoms that strongly couple to the resonator field. Since this scheme relies on rerouting the detection light onto a particular single photon counter, whenever an atom passes through the evanescent field, it can be seen as a light switching process, mediated by a single atom (see Fig. 4.10). This switching process has several advantages over the one using two coupling fibers that was previously performed (see section 3.5 and [19]): Correlation measurements between atom and photon quantum state, which are crucial for the verification of entanglement, could easily be realized without the need of an additional
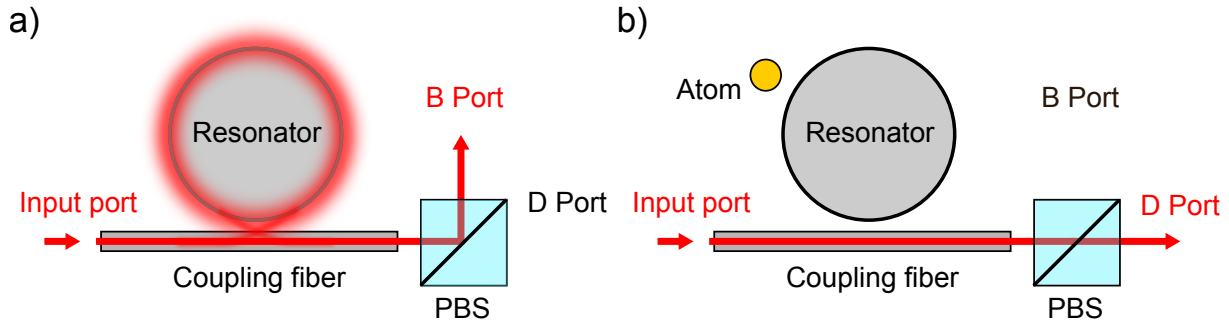
**Figure 4.10:** *Illustration of the new switching scheme, that uses the polarization change for light switching. Two polarization components have to be sent through the coupling fiber. When no atom is coupled to the evanescent field of the resonator, one polarization component will couple into and out of the resonator, acquiring a phase shift of $\pi$ with respect to the polarization component in the coupling fiber. The presence of an atom will prevent the light from coupling into the resonator and, hence, from being phase shifted. When superposed with the second polarization component, the light has changed its polarization by 90° and, thus, will be directed to the other port by the PBS.*

interferometer setup. Furthermore, the new scheme only requires one coupling fiber, thus the spare one could be used for coupling additional light into the resonator. In addition, it allows us to detect atoms even for a non-critically coupled resonator, thereby opening up a new regime for our experiment.

In the following I am going to discuss the realization of an optical switch based on polarization rotation. An ideal light switch should redirect all the light that was initially sent to port B to port D when an atom is present. While such a switch might introduce losses, they should be the same for both ports. In order to realize a high contrast switch using the polarization analysis setup, two requirements have to be fulfilled (see Fig. 4.11). First, the transmission through the coupling fiber of the polarization component coupling into the resonator has to be the same with and without an atom present. This is definitely not fulfilled for critical coupling, where the transmission for this polarization component is zero if no atom is present and rises to about 70% when a atom passes the evanescent field. However, by going into the over-coupled regime, where $\kappa_e = \sqrt{\kappa_0 \kappa_c^{(a)}}$ (see Eq. (4.8)), the case of equal amplitudes can be achieved. The second requirement for high contrast switching is that the other polarization component, which is not coupling to the resonator, must have the same amplitude as the other one, after passing the resonator. This automatically fixes our detection basis vectors to be $|D\rangle = \frac{1}{\sqrt{2}}(|TM\rangle + |TE\rangle)$ and $|B\rangle = \frac{1}{\sqrt{2}}(|TM\rangle - |TE\rangle)$. In our experiment, the distribution between the two polarization components is carried out by rotating the half wave plate in front of the fiber network. Thus, the total light power sent onto the resonator is fixed and the ratio of the non-coupling and coupling field amplitude is $\alpha = \sqrt{T}$, see Eq. (2.28).

45
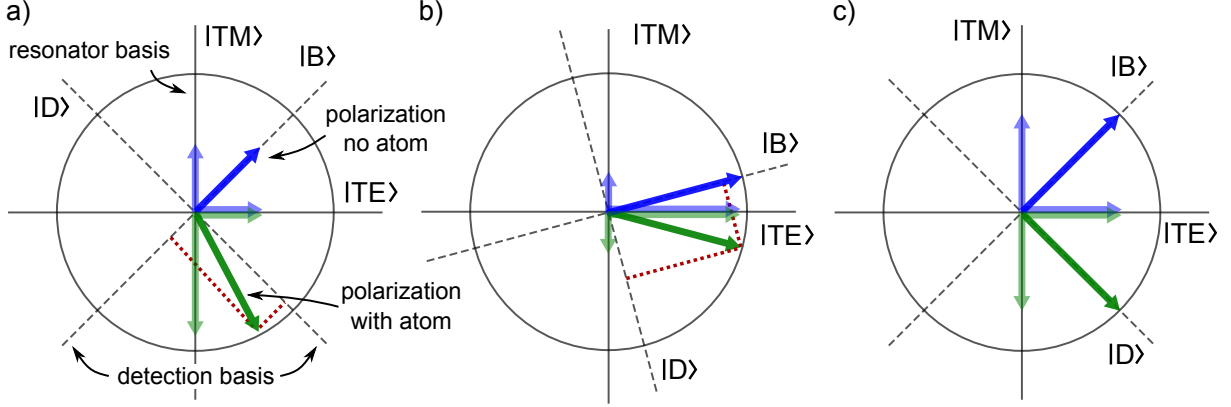
**Figure 4.11:** Projection of the total output field vector, onto the $|TM\rangle$-$|TE\rangle$-plane, without an atom (blue) and in the presence of an atom (green). Only the $|TM\rangle$-component couples to the resonator, while the $|TE\rangle$-component stays in the coupling fiber. The detection basis is always chosen such that the detection port $|D\rangle$ is dark when no atom couples to the resonator. The red dotted lines indicate the projection of the polarization vector with atom onto the detection basis $|D\rangle$ and $|B\rangle$. Due to the interaction with the resonator, the sign of the $|TM\rangle$-component changes. a) If the fiber transmission of the $|TM\rangle$-component is not the same with and without an atom present, it is not possible to redirect all light into the initially dark detection port $|D\rangle$. b) If the polarization component that does not couple to the resonator is smaller or larger than the other component, will neither yield high contrast switching. c) Only if the two components in $|TM\rangle$ and $|TE\rangle$ direction have equal size and the transmission of the $|TM\rangle$-component does not change its modulus when an atom couples, a perfect redirection of the light can be achieved.

In order to find the best light switching configuration for our experiment, the distance between the coupling fiber and the resonator was scanned from critical coupling ($\kappa_e/\kappa_0 = 1$) to the extremely over-coupled regime ($\kappa_e/\kappa_0 = 20$). From analyzing the temporal photon distribution of the coupling events for both polarization output ports $|D\rangle$ and $|B\rangle$, the detected signal with and without an atom present can be identified, as illustrated in Fig. 4.12. Figure 4.13 shows the fiber transmission for these cases as a function of $\kappa_e$. When no atom couples to the resonator, we see an increase of the signal in the $|B\rangle$-port as we move the fiber closer to the resonator. Since the light is now more efficiently coupled into and out of the resonator, it has less time to be dissipated and thus the losses are reduced. This behavior corresponds to Eq. (2.28). At the same time, the $|D\rangle$-port, which is used for detecting coupling events, stays dark for all $\kappa_e$ since we simultaneously change the detection basis. Now, when an atom couples to the resonator field, the signal detected by the two ports changes significantly. Starting from critical coupling, the number of photons detected at the $|D\rangle$-port rises while the number at the bright port $|B\rangle$ drops, reaching their maximal and minimal value for $\kappa_e/\kappa_0 \simeq 2.5$ respectively. Further decreasing the distance causes the polarization component sent to the $|D\rangle$-port to decrease and the other to increase. At approximately $\kappa_e/\kappa_0 = 8$ they cross. The solid lines in Fig. 4.13 are theoretical predictions, where the simplified model introduced in chapter 2.2 is applied. For
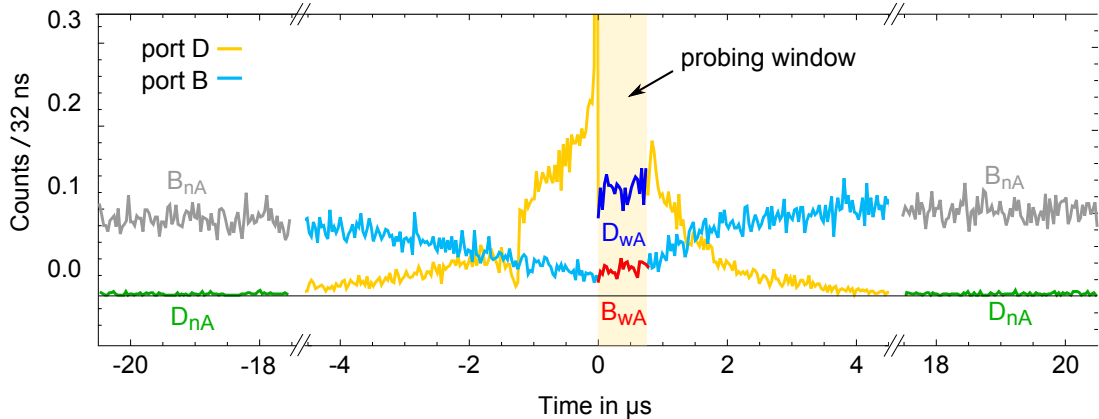
**Figure 4.12:** Histogram of the photons detected per 32 ns bin in the $|D\rangle$-port (yellow) and the $|B\rangle$-port (light blue) of the PAS, when $\kappa_e/\kappa_0$ was set to 2.5. The colored parts of the curves indicate the time windows used to deduce the values for Fig. 4.13. The actual time frame used to average the counts was 50 to 650 ns for the case with an atom present and 12000 to 24000 ns for the reference without an atom. For this measurement, a second detection threshold value $n_{2nd} = 1$ was used.

the coupling strength we assumed a Gaussian distribution centered at $\bar{g}/2\pi = 17$ MHz with a standard deviation of $\sigma_g/2\pi = 6$ MHz, obtained from measurements of the vacuum Rabi splitting (see section 3.5 and [18] for more details). The resonator mode we use has a decay rate of $\kappa_0/2\pi = 9$ MHz and the atomic decay rate corresponds to the HWHM of the natural line width and is given by $\gamma/2\pi = 3$ MHz for the rubidium 85 D$_2$ line [48]. The only free parameter for the curves was the detuning between the light and the atom $\Delta_{AL}$, which can be caused by a slight offset of the laser lock. The best agreement with the experimental data is obtained for a detuning of $\Delta_{LA}/2\pi = 3$ MHz, slightly larger than the expected 1.6 MHz, which could be explained by our bias magnetic field.

Since the switching is based on the fact that the presence of the atom causes a polarization rotation of the field sent through the coupling fiber, it is apparent to quantify the performance of the switching process by the magnitude of rotation of the polarization when an atom passes through the resonator field. Thus, we define the angle $\Theta = \arctan(\sqrt{D_{wA}/B_{wA}})$ as shown in Fig. 4.14. For an ideal switching, $\Theta$ should reach 90° at $\kappa_e = \sqrt{\kappa_0 \kappa_c^{(a)}}$. Using the data in Fig. 4.13, we can calculate this angle as a function of $\kappa_e$, which is plotted in Fig. 4.15. For critical coupling the angle is 45°. When further over-coupling the resonator we get a maximum rotation angle of 65° for $\kappa_e/\kappa_0 = 2.5$. By using the same experimentally obtained coupling parameters as before, it is possible to calculate a theory curve. In Fig. 4.15 we see that the theoretical predictions agree with the measured data. Thus, the deviation from the ideal 90° rotation is caused by the distribution of the coupling strengths $g$ and the slight detuning between atom and laser. Furthermore, the theory also coincides with the measured maximum angle at $\kappa_e/\kappa_0 = 2.5$,
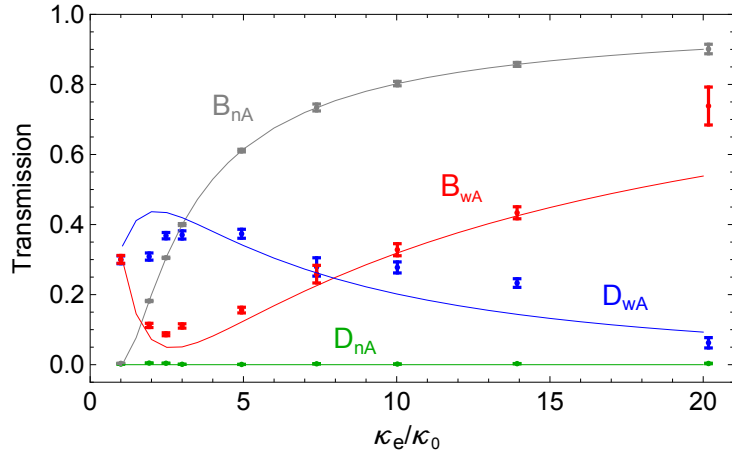
**Figure 4.13:** Results of the switching measurement: Detected photons in the two output ports of the polarization analyzer setup ($|D\rangle$ and $|B\rangle$) as a function of the coupling rate $\kappa_e$ in units of the internal loss rate $\kappa_0$, for the case when an atom is coupled to the evanescent field of the resonator (wA) and without an atom present (nA). The fiber transmission was normalized to the expected input power that is given by $\mathrm{B}_{nA}\left(1 + \frac{\kappa_0 + \kappa_e}{\kappa_e - \kappa_0}\right)/2$, where $\kappa_e/\kappa_0$ is known from setting the fiber transmission, see Eq. (2.28). The data points have been deduced from histograms like Fig. 4.12. The solid lines represent the theoretical predictions for $(\bar{g}, \sigma_g, \Delta_{AL}, \gamma, \kappa_0) = 2\pi \cdot (17, 6, 3, 3, 9)$ MHz. The error bars indicate the $\pm 1\sigma$ statistical error.
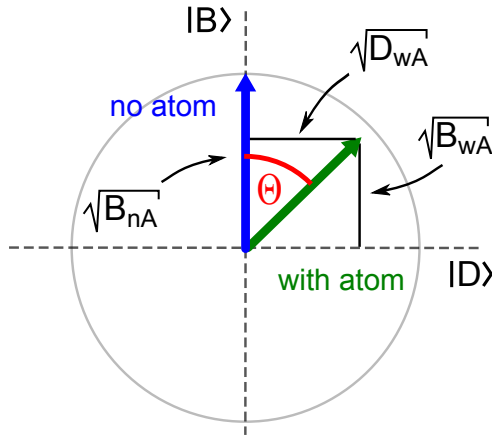


**Figure 4.14:** The definition of the rotation angle $\Theta = \arctan(\sqrt{\mathrm{D_{wA}}/\mathrm{B_{wA}}})$.

which differs from the initially predicted $\kappa_e/\kappa_0 = \sqrt{\kappa_c^{(a)}/\kappa_0} = 3.4$.

In order to get an idea of the losses introduced by the switching process, we calculate the photon survival probability from the measured data. This gives the probability to recover an incident photon after the switching process. We distinguish between the survival probability for the cases with and without an atom coupling to the resonator and the total survival probability as their mean. These quantities are illustrated in Fig. 4.16, as a function of $\kappa_e$. For maximum rotation angle, we find a survival probability, of around
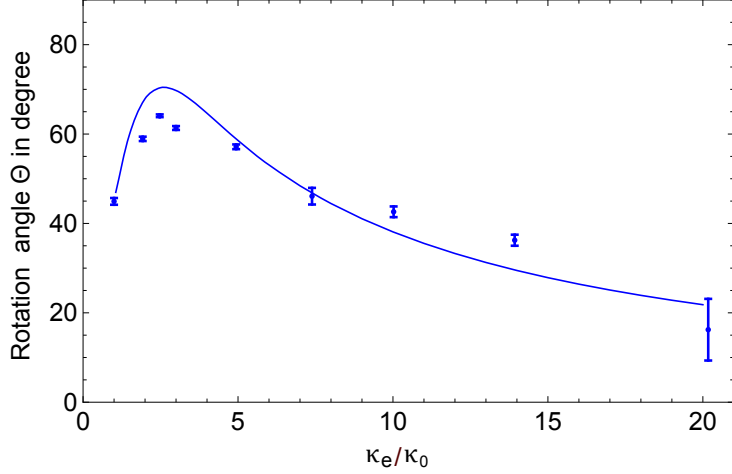
**Figure 4.15:** The rotation angle $\Theta$ as a function of $\kappa_e$. The theoretical prediction (solid line) for $(\bar{g}, \sigma_g, \Delta_{AL}, \gamma, \kappa_0) = 2\pi \cdot (17, 6, 3, 3, 9)$ MHz agrees with the measured data. The error bars indicate the $\pm 1\sigma$ statistical error.

40%, which increases with rising $\kappa_e$, e.g., for $\kappa_e/\kappa_0 = 5$ it reaches 60%, while we still observe a rotation by more than 55°. The survival probability can be enhanced by using a mode with a higher Q-factor, thus giving a higher transmission for $\kappa_e = \sqrt{\kappa_0 \kappa_c^{(a)}}$.

We note that we only analyzed the polarization rotation in one basis. While this is enough to obtain the average angle, it does not allow us to deduce the exact final polarization state and whether this state is a pure or a mixed state. But this was the first prove-of-principle measurement, demonstrating the ability to switch light using polarization rotations, introduced by a single atom. As a next step, the polarization analyzer will be set up to measure two bases simultaneously (see Fig. 4.5) and a full state tomography will be performed.

Another way to quantify the performance of the switching process, is to introduce the switching fidelity, which we define as the probability that the photon ends up in the correct port of the PAS, i.e the D-port, when an atom couples to the resonator and the B-port otherwise. Thus, the fidelity (including all losses) is given by $\mathcal{F} = (\mathrm{D}_{wA} + \mathrm{B}_{nA})/2$. Fig. 4.17 shows this fidelity as a function of $\kappa_e$. Although the resonator mode we used had a comparatively low Q-factor, we are able to observe a switching fidelity significantly higher that 50%.
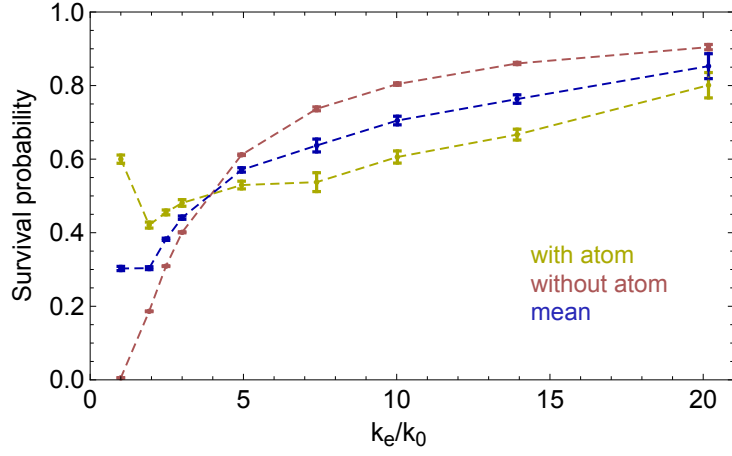
**Figure 4.16:** The probability to recover an incident photon after the switching process as a function of $\kappa_e$ for the case with an atom present, without atom and for the total switching process, are plotted. The dotted lines are a guide to the eye and the error bars indicate the $\pm 1\sigma$ statistical error.
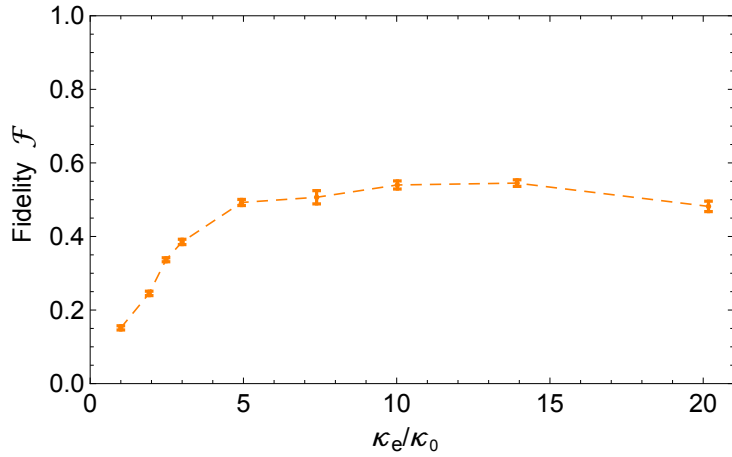


**Figure 4.17:** From the data shown in Fig. 4.13 the fidelity $\mathcal{F} = (\mathrm{D}_{wA} + \mathrm{B}_{nA})/2$ of the switching process can be calculated. The maximum fidelity is observed for $\kappa_e/\kappa_0 = 14$ and exceeds 54%. The dotted line is a guide to the eye and the error bars indicate the $\pm 1\sigma$ statistical error.

# Chapter 5

# Toward coherent state manipulations

## 5.1    General considerations

As has been discussed in section 3.5 and 4.4, our experimental apparatus is capable of performing classical switching operations, where light is routed between two different output ports, depending on the presence of a strongly coupled atom in the resonator mode. The next step toward a quantum switch is to realize an active switching scheme, where the atom can be transferred between two internal ground states, one resonant and the other off-resonant to the cavity. In this way, light can be routed between the two ports, depending on the internal state of the atom. In addition to this active switching, it is also possible to prepare a coherent superposition of the two atomic states. This would then allow us to generate a macroscopic superposition state of light, often referred to as Schrödinger cat state [22], or an all-optical deterministic quantum gate [49]. In our experiment we couple single rubidium 85 atoms to the resonator. The hyperfine level structure of the $D_2$ transition is schematically plotted in Fig. 5.1. The resonator is tuned to resonance with the F=3 → F'=4 transition. In order to implement switching, one has to be able to transfer the atom into a state that does not couple to the resonator mode. This can be achieved by transferring the atom into a state that is sufficiently far off resonance with respect to the resonator frequency. The frequency difference between the F=2 and F=3 hyperfine ground states of $5^2S_{1/2}$ is 3.036 GHz [48], which is much larger than the resonator line width $\kappa$ , the natural line width of the atom $\gamma$ and the coupling strength $g$. Thus, placing the atom in the F=2 state should suffice to suppress any interaction with the resonator. In principle, there are two ways of driving this transition: using optical or microwave fields. The possible implementation of these two options will be discussed in the following section.
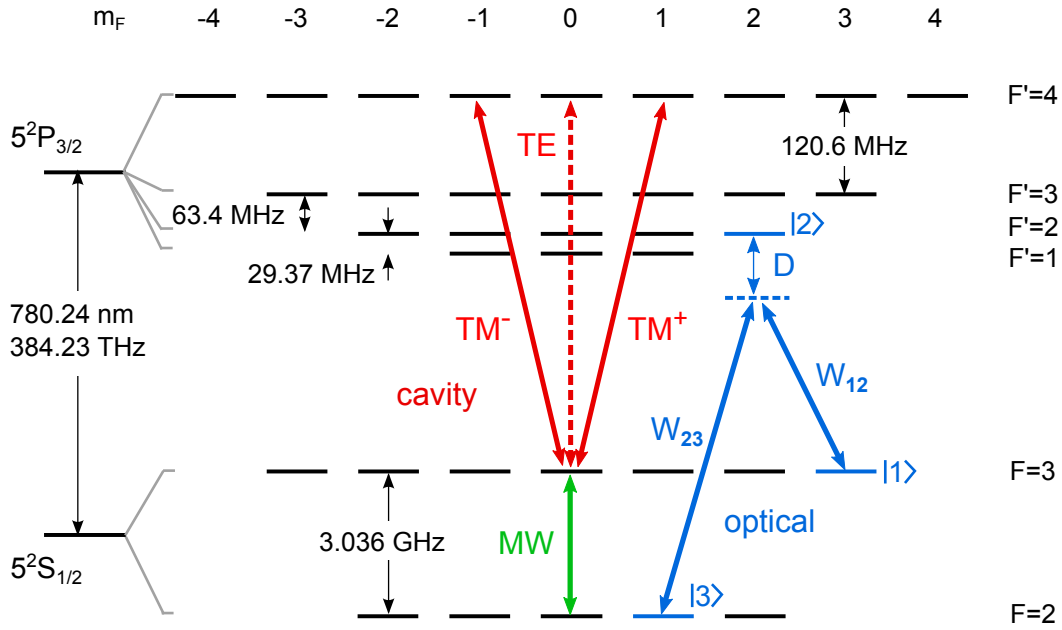
**Figure 5.1:** Level scheme of the rubidium 85 $D_2$ transition for zero magnetic field. The two fine-structure states $5^2S_{1/2}$ and $5^2P_{3/2}$ have an energy splitting corresponding to a transition wavelength of 780.24 nm. The first is divided into two hyperfine level F=2,3, forming internal ground states, while the latter splits into four levels with F'=1,2,3,4. Each of these states consist of (2F+1) Zeeman sub-levels, which are degenerate for zero magnetic field. The resonator is tuned to resonance with the F=3$\rightarrow$ F'=4 transition, where the different modes couple different $m_F$ states (red). A direct transition between the two ground states (F=2 $\rightarrow$ F=3) can be driven using a microwave pulse (green). It is also possibility realize a population transfer using optical fields that couple the two ground states via a so-called lambda scheme (blue).

**Microwave transition**

As shown in Fig. 5.1, direct transitions between the $F = 2$ and $F = 3$ hyperfine levels of $5^2S_{1/2}$ are driven by magnetic dipole interactions in the microwave regime. The time-scale for a population transfer is the inverse Rabi frequency $2\pi/\Omega$, which scales with the field strength. In our experiment, we require $2\pi/\Omega < 0.5$ $\mu$s or $\Omega > 2\pi \cdot 2$ MHz, due to the limited interaction time of the atom with the resonator field. Unfortunately, this cannot be realized using microwave antennas outside the vacuum chamber, where typical powers of 10 W yield Rabi frequencies of $\Omega \sim 2\pi \cdot 15$ kHz [50]. A possibility to speed up the dynamics is to use microwave near fields, generated by oscillating currents in close proximity of the resonator. Using integrated circuits in direct vicinity of trapped ions, coherent state manipulations on time-scales of 20 ns have been performed [51, 52]. However, implementing such a near field source would require major modifications on the experimental setup, which would involve opening the vacuum chamber. At the moment, this is not an option.

**Optical transition**

Using two photon processes in a Λ level scheme, such as shown is Fig. 5.1, it is possible to drive optical dipole transitions between the two hyperfine ground states without significantly populating the excited state. Due to the high local intensity which can be achieved using laser light, these transitions take place on a much shorter time scale. There exist different methods for driving two-photon transitions, such as Raman transitions or stimulated Raman adiabatic passages (STIRAP) [53, 54]. For both, two laser beams with an frequency difference of 3 GHz have to be applied. The corresponding Rabi frequencies are denoted $\Omega_{12}$ and $\Omega_{23}$, as illustrated in Fig. 5.1. Even though these processes can be performed when the laser beams are tuned away from their respective transition, the so-called two-photon resonance condition has to be fulfilled, i.e., the respective detunings $\Delta_{23}$ and $\Delta_{12}$ of both lasers have to be the same ($\Delta_{23} = \Delta_{12} = \Delta$). For a resonant Raman pulse, both lasers are applied simultaneously which causes coherent oscillations between the two ground states $|1\rangle$ and $|3\rangle$ with an effective Rabi frequency $\Omega_{eff} = \Omega_{12}\Omega_{23}/\Delta$. Resonant Raman pulses require a precise control of the experimental parameters, such as the Rabi frequencies, which are very sensitive to variations of the coupling strength. A more robust technique is the STIRAP. For this process, the intensities of the two laser beams are adiabatically turned on and off in a counter-intuitive pulse sequence, where the field that drives the transition between the initially populated state and the excited state is applied with a certain time delay, with respect the to other field. Using a suitable temporal evolution of the laser pulses, an adiabatic evolution of the dressed state can provide a very efficient population transfer. Since the adiabatic evolution of the so-called dark state only depends on $\Omega_{12}/\Omega_{23}$, such a scheme is insensitive to simultaneous changes of both Rabi frequencies. In order to prevent excitation of unwanted $m_F$-levels due to experimental imperfections such as residual field components with unwanted polarization, it is crucial for both processes to lift the $m_F$-degeneracy by applying a magnetic field (see section 5.3).

In order to perform well-controlled optical state transfers in our experiment, we would like to address all atoms that couple to our resonator in a similar manner, concerning both the intensity and polarization of the Raman light. The most straightforward approach would be to shine in a laser from outside onto the resonator. However, due to the presence of the resonator, the field will be strongly modified. In order to obtain an idea of the field distribution outside of the resonator in this situation, we consider a simplified model where our bottle-shaped resonator is approximated by an glass cylinder, with radius $a = 18$ $\mu$m and refractive index $n = 1.45$, illuminated perpendicular to its axis (see Fig. 5.2a). Assuming an incident plane wave, we distinguish between the two cases, where the electric field is polarized parallel or perpendicular to the resonator axis, which we refer

to as TM and TE polarized light, respectively (not to be confused with the polarizations introduced for the resonator modes). Following the routine described in [55], this light scattering problem can be solved by expanding the fields in terms of eigenfunctions of the electromagnetic wave equation and determining the coefficients by applying the boundary conditions for dielectric interfaces. The intensity distribution around the resonator for the two possible polarizations is depicted in Fig. 5.2b. For both polarizations, a strong modulation along the circumference of the resonator due to interference between the incoming and scattered field is visible. From measurements of the Rabi spectrum, we infer that the atoms that couple to our resonator are about 100 nm away from the resonator surface. The intensity of the light along half a circumference at a distance of 100 nm, is plotted in Fig. 5.2c. For both polarizations, strong oscillations occur along the whole circumference, ranging from 15 times the incoming intensity to zero. Since the exact position of the atoms that couple to the resonator is not known and varies from one experimental run to the next, it is not possible to uniformly act on all of them by just shining a laser onto the resonator.

This leaves only the possibility to directly use the resonator field to address the atoms. Since we use the same mode for detecting the presence of the atoms, we can be sure that the Raman light will interact with the atom as well, independently of their position along the circumference. Now, the evanescent field decays exponentially. Thus, the coupling strength and the Rabi frequency changes as the atom moves in radial direction. However, this should not be a problem for the robust STIRAP processes. As we have seen in section 2.1, the light confined in a WGM resonator is either linearly or circularly polarized, with respect to the resonator axis, depending on the input polarization. This enables us to drive coherent two-photon processes between distinct energy levels using the resonator modes (see Fig. 5.1). However, employing the resonator modes has one major drawback: In order to fulfill the two-photon resonance condition, required for Raman transitions, the two laser fields have to be detuned by about 3 GHz with respect to each another. As a consequence, at least one of them has to be far detuned from the cavity resonance. The power fraction coupled into the resonator as a function of the detuning $\delta$ to the resonator is given by a Lorentzian with a FWHM of two times the cavity decay rate $\kappa$. For frequencies far off resonance, the power fraction can be approximated by

$$\frac{P}{P_0} = \frac{\kappa}{2(\delta^2 + \kappa^2/4)} \approx \frac{\kappa}{2\delta^2} \, , \tag{5.1}$$

where $P_0$ is the power of the incident beam. The frequency shift between the F=3 and F=2 level requires a detuning $\delta = 2\pi \cdot 3$ GHz. For our high-Q WGM with decay rate
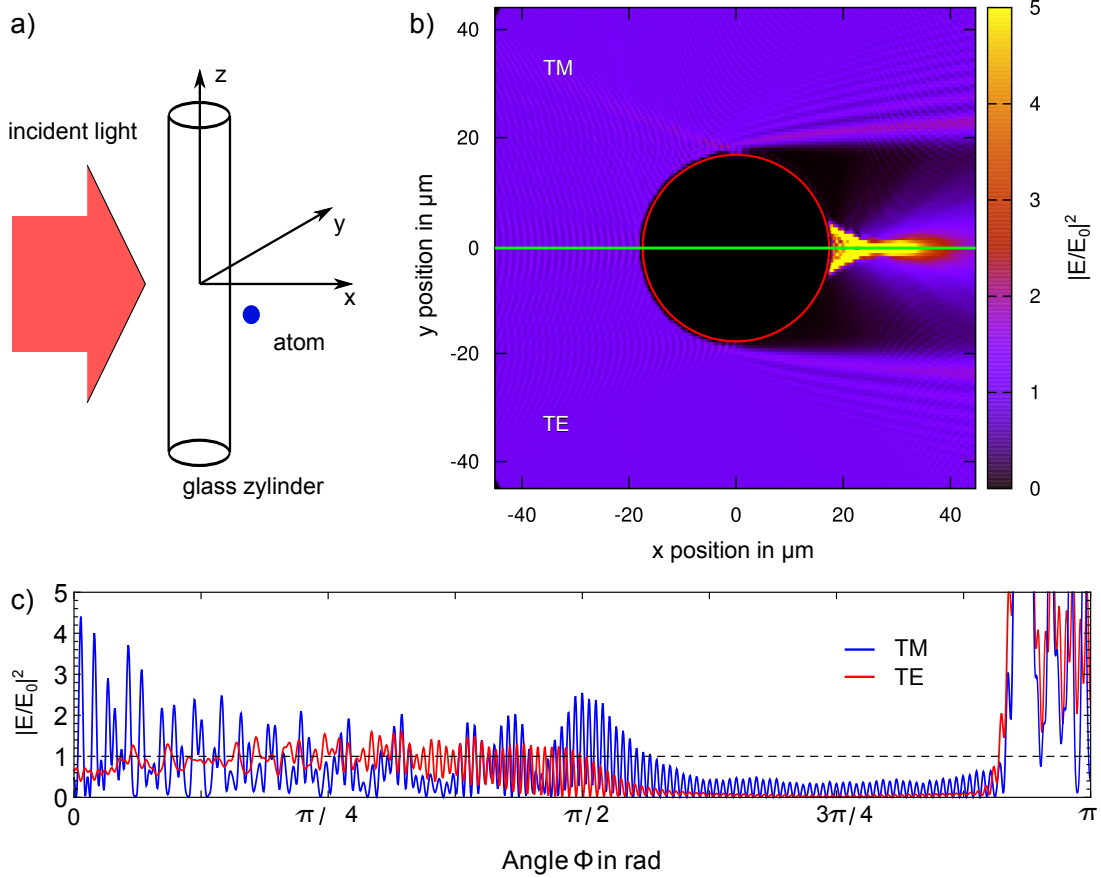
**Figure 5.2:** a) Schematic of an atom in the vicinity of a glass cylinder illuminated perpendicular to its axis. b) Intensity distribution around the cylinder with radius $a = 18\ \mu$m and refractive index $n = 1.45$, similar to our bottle resonator, for TE and TM polarization. c) Intensity along the circumference 100 nm away from the resonator surface. In both, b) and c) the intensity maximum of $15\ |E/E_0|^2$ in the caustic was cropped for better visibility of the modulation along the circumference.

$\kappa = \omega_0/2Q = 2\pi \cdot 10$ MHz, this yields an incoupling suppression of

$$\frac{P}{P_0} \sim 5 \cdot 10^{-7} \,\hat{=}\, -63\,\text{dB}\,,\tag{5.2}$$

i.e., we have to send in $10^7$ times more power than on resonance through the coupling fiber, to couple a comparable amount of light into the cavity. The light for driving Raman transition and for detection are delivered to the resonator via the same fiber. To ensure that the Raman light does not dominate over the weak signal during our detection phase, where we probe the system with light powers on the single photon level, we require a high suppression of the Raman light of $\gg 70$ dB.

Since the atoms only couple to the resonator for a few $\mu$s and at least 1.2 $\mu$s are required for detection, a sub $\mu$s state manipulation has to be implemented. Thus, the light switching setup should combining short switching times of below 100 ns, with a high extinction ratio

$\gg$ 70 dB. The Mach-Zehnder modulators which are currently used for fast switching have a specified extinction ratio of 30 dB and thus cannot be employed for this task. In the next chapter, I present a new AOM-based setup that fulfills these requirement.

## 5.2 AOM switching setup

In order to meet the requirements of sub-$\mu$s switching times and high extinction ratio, during this thesis, an acousto-optic modulator (AOM)-based setup has been designed. Optimizing the beam diameter and the alignment of the beam with the AOM, one can achieve switching times on the order of 10 ns. When an AOM is set up in a so-called double-pass configuration, where the light passes through the AOM twice, very high extinction can be obtained. This allows one to fulfill all requirements in an AOM based setup.

### 5.2.1 Experimental setup

The Working principle of an AOM is depicted in Fig. 5.3. In order to drive Raman transitions, we need two laser beams that can be independently switched. In order to avoid alignment problems when changing the AOM's frequency and to achieve higher on/off-switching ratios, we operate the AOMs in the so called double-pass configuration [56]. In this configuration, the AOM is placed in the joint focal point of two lenses. After passing the lenses and the AOM, the diffracted beam will be reflected back into the AOM using a mirror, causing a second frequency modulation. The undiffracted beam is blocked in front of the mirror. In order to separate the incident from the back reflected beam, a
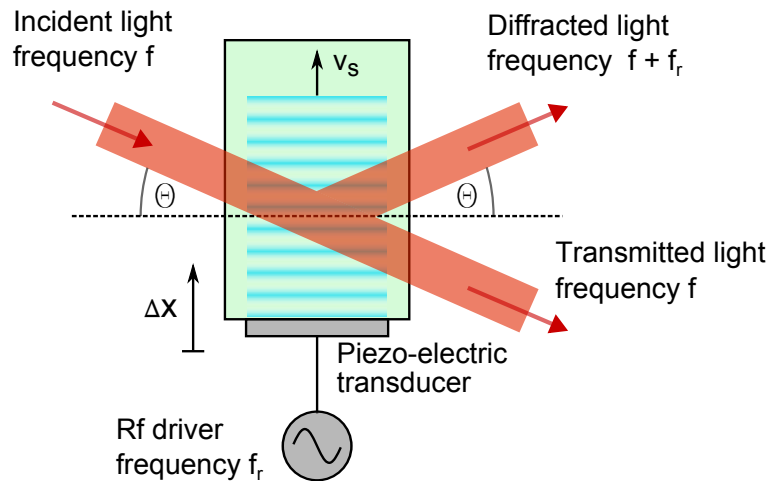


**Figure 5.3:** Simplified schematic of an AOM. Applying a RF-signal, with frequency $f_r$, to the AOM, will generate an acoustic wave traveling through the crystal, thereby causing a modulation of the refractive index. Light propagating through the crystal will be diffracted by this acoustic grating, according to Bragg's law. For the first order diffracted beam, the frequency of the light will change from $f$ to $f' = f + f_r$. Changing the modulation frequency inevitably causes a change of the diffraction angle. The delay, caused by the fact that the acoustic wave has to travel a certain distance before encountering the beam, is minimized by moving the piezo electric transducer closer to the laser beam. This is done by placing the AOM on a translation stage, that moves in x-direction.
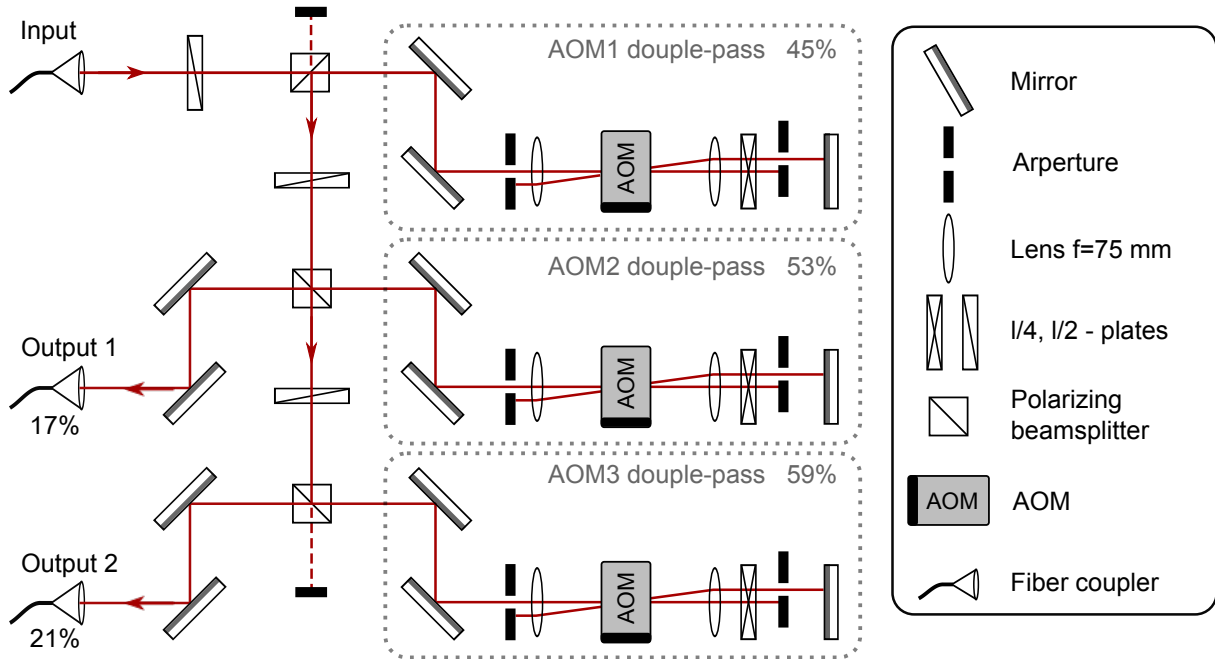
**Figure 5.4:** AOM setup for generating a pair of Raman beams. The setup consist of three AOMs in double-pass configurations. Three polarizing beam splitters (PBS) are used to separate the beams, after passing through the double-pass configuration and the half-wave plates are used to adjust the power in the different arms. The achieved diffraction efficiency, is indicated next to the respective AOM. The total efficiency, including the fiber-coupling efficiency, for each path is indicated next to the output couplers. In order to get the 3 GHz detuning of one beam, required for Raman transitions, one sideband of an electro-optic phase modulator can be used. The second sideband should be far off resonance.

quarter-wave plate is placed behind the AOM. Since the light passes the wave plate twice, its polarization be turned by 90° and the beam is then separated from the incident beam using a polarizing beam splitter.

The complete AOM-setup is shown in Fig. 5.4. In principle the setup consists of three AOMs in double-pass configuration. The incident beam enters the setup through the fiber coupler at the top. The following half-wave plate turns the polarization such that all the light is transmitted through the first polarizing beam splitter (PBS). After passing AOM1 twice, the beam gets redirected by the first PBS toward the other AOM branches. The first AOM is common to both Raman beams and is used to enhance the extinction ratio of our setup. Afterward, a second PBS distributes the light into two paths, each consisting of an additional acusto-optical modulator (AOM2 and AOM3) in double-pass configuration. In this way, we generate both laser beams form one laser source, which yields a well defined phase relation between them. Using a half-wave plate, the splitting ratio of the two beams can be adjusted. In this configuration, each beam passes four times through an AOM, which is necessary to achieve the desired on/off switching ration. The RF-signal which drives the AOMs is provided by the RF-circuit that is schematically
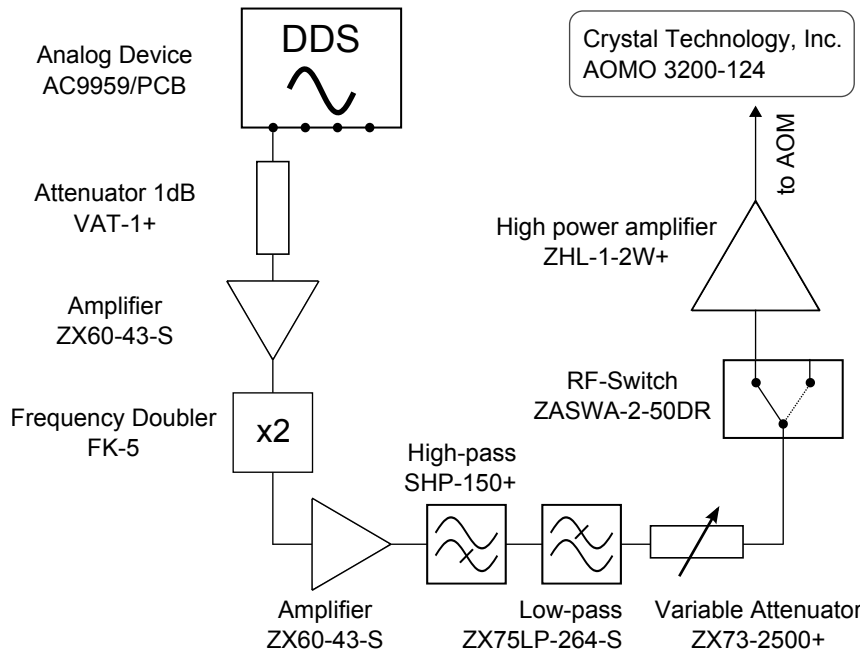
**Figure 5.5:** Schematic of the AOM driver setup. The initial signal provided by a direct digital synthesizer (DDS) is first frequency doubled, preamplified and filtered. Then the amplitude of the signal is adjusted by a variable attenuator and after passing a RF-switch, it is sent to the high power amplifier.

shown in Fig. 5.5. A direct digital synthesizer (DDS) provides up to four phase coherent outputs. Three of them are used to drive the AOMs. Using a 100 MHz external clock oscillator, the DDS can generate a maximal frequency of 150 MHz. Since the drive frequency of the AOMs lies in the range of 150-250 MHz the signal has to be frequency doubled. Due to the high losses introduced by the frequency doubler, the signal has to be preamplified before being connected to the high power amplifier, that generates the 2 W RF-signal for the AOMs. To filter unwanted harmonics a high and a low pass are implemented in the circuit. The driving signal can be turned on and off within 5 ns, using high speed RF-switches. At the same time, these switches provide a high isolation of typically 82 dB, which is crucial for the extinction ratio of our setup. Furthermore, a voltage controlled attenuator (VCA) provides the possibility to adjust the RF-power, which can be used to stabilize the laser intensity or to drive smooth intensity pulses (see Fig. 5.6).
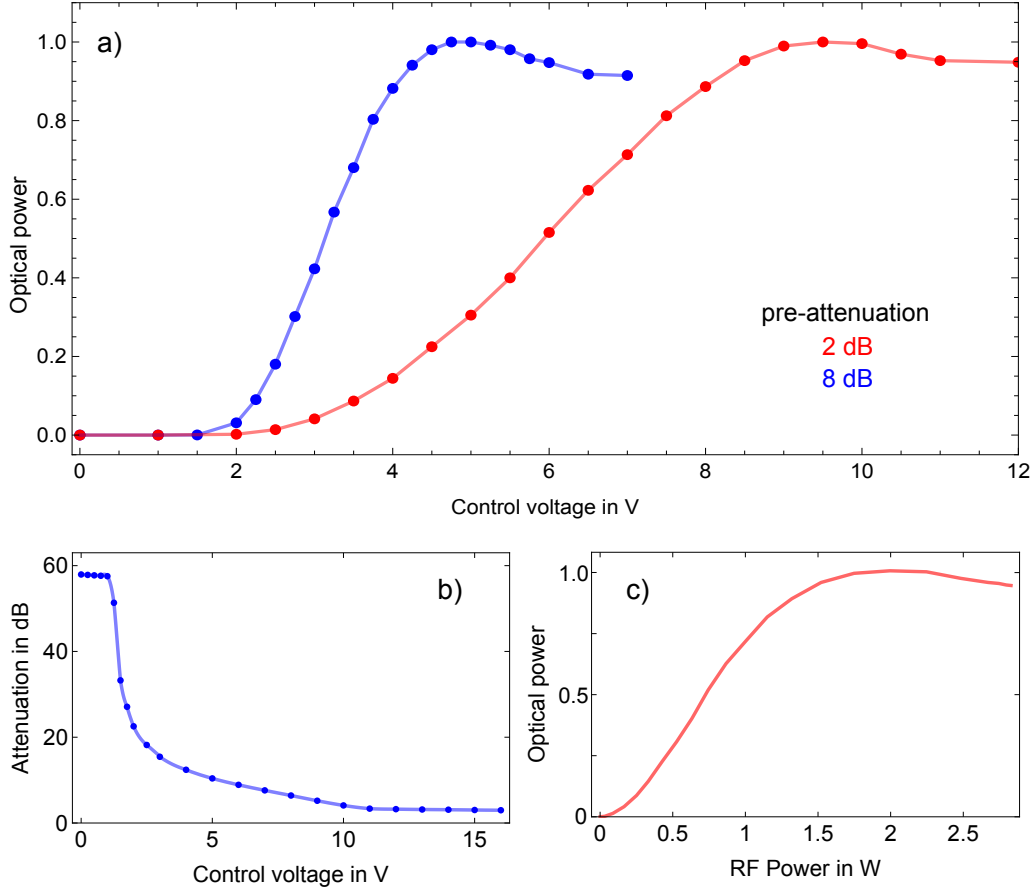
**Figure 5.6:** a) Normalized light power in the first diffraction order which is coupled into a single mode fiber, as a function of the voltage applied to the voltage controlled attenuator (VCA). Placing a fixed attenuator in front of the variable attenuator changes the operating point of the VCA and thus the slope can be changed. b) The attenuation of the variable attenuator as a function of applied voltage. c) The power-dependency of the normalized light power, which corresponds to the AOM's diffraction efficiency. Figure c) was deduced from measuring a) and b).

## 5.2.2 Performance

In the following the basic properties of the AOM setup are summarized.

**Frequency tuning bandwidth**

The control of the experimental apparatus is highly automated and can perform parameter scans without manual readjustment. When scanning the modulation frequency of the AOMs, the optical power provided by the AOM setup should not vary significantly. But the diffraction angle crucially depends on the modulation frequency. Thus, varying the modulation frequency changes the fiber coupling, even when the AOM is set up in double-pass configuration. In order to quantify this effect, we determine the frequency tuning bandwidth, which we define as the frequency range over which the AOM frequency can be shifted, before the fiber coupled light power drops to half its maximum value. The
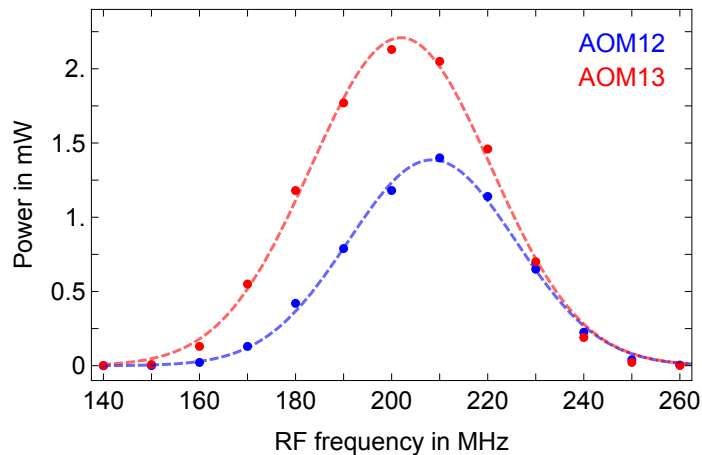
**Figure 5.7:** Laser power coupled into the single mode fiber as a function of the driving frequency for both AOM branches. The measured points have been fitted with a Gaussian, giving a FWHM for the respective AOM path of $\Delta\omega_{\mathrm{AOM12}} = 41\,\mathrm{MHz}$ and $\Delta\omega_{\mathrm{AOM13}} = 44\,\mathrm{MHz}$ and central frequency of about 200 MHz.

power coupled into the single mode fiber as a function of the driving frequency, for both branches, is shown in Fig.5.7. For technical reasons the modulation frequency of AOM1 and AOM2 (AOM1 and AOM3) has been changed simultaneously. From fitting this data the tuning bandwidth can be determined:

$$\Delta\omega_{\mathrm{AOM12}} = 41\,\mathrm{MHz} \qquad \Delta\omega_{\mathrm{AOM13}} = 44\,\mathrm{MHz}\,. \tag{5.3}$$

We have to keep in mind that both beams pass four times through an AOM crystal and thus acquires a frequency shift of four times the applied RF-signals. The total modulation frequency, within the tuning bandwidth, corresponds to about 15 times the line width of a typical resonator mode, which is about 10 MHz.

**Extinction**

The experiments that we perform work on the single photon level. But if we want to drive Raman transitions by coupling off-resonant light into the resonator, we have to send a large amount of optical power ($\sim \mu\mathrm{W}$) through the coupling fiber. This light should only be turned on for the duration of the Raman pulse, while for the rest of the experimental sequence no light should leak to our detectors and perturb the experiment and detection process. Thus, one of the key parameters of the setup is the extinction ratio, which is commonly used to qualify the performance of a switch. It is defined as the negative logarithm of the ratio between the optical power at maximum (turned on) and minimum (off) transmission.

$$ER = -10\log_{10}\frac{\mathrm{P_{off}}}{\mathrm{P_{on}}} \tag{5.4}$$

To measure this quantity, all AOMs are turned off using the RF-switches and the photon number that still leaks through the setup is measured with a single photon counter. This value is compared to the maximum power, when all AOMs are turned on, which is measured with an optical power meter. For the two branches we measure a total extinction ratios of $ER_{12} = 110$ dB and $ER_{13} = 126$ dB, largely outperforming the Mach-Zehnder switches ($ER_{MZ} = 24$ dB [47]), which are currently used in our experiment for switching between detection and probe light fields. Furthermore, the measured extinction clearly fulfills the requirement stated in the beginning of this chapter ($\gg 70$ dB).

**Delay and switching times**

The atoms couple to the resonator at random times. Thus, in order to optimally exploit the limited measurement time, all possible retardation and delays in the switching processes have to be minimized. The main contributions of the AOM setup are the fall/rise time and the delay of the optical signal with respect to the RF-signal. Both highly depend on the position and the size of the beam in the AOM crystal and are limited by the finite velocity of the traveling acoustic wave insight the $TeO_2$ crystal, which is specified as 4200 m/s.

The rise and fall time correspond to the time, the acoustic wave takes to cross the beam cross-section with diameter D, when the RF-signal is turned on and off and thus can be changed by varying the spot size of the beam. For a Gaussian beam, the focus size that results from focussing with a lens with focal length $f$ is given by [57]

$$D' = \frac{4\,\lambda\,f}{\pi D} \ .$$

(5.5)

However, the diffraction efficiency of the AOM drastically drops with decreasing the beam diameter. According to the AOM specifications, a diameter of 30 $\mu$m would provide a rise time of 13 ns and an diffraction efficiency of 60% . For our initial beam diameter of about 3 mm, this can be achieved by using a lens with focal length $f = 75$ mm.

The delay, introduced by the AOM, is due to the fact that the traveling sound wave, which originates from the piezo electric transducer has to travel a certain distance through the crystal before it reaches the light beam. For $TeO_2$, a displacement of 1 mm corresponds to 238 ns of additional delay. In order to minimize this delay, we mount the AOMs on translation stages, which make it possible to move the piezo with respect to the beam.

For optimizing the delay and switching times, we measure the light that passed through the AOM setup using a fast photodiode (Hamamatsu G4176-03). This signal was compared to the signal of the function generator, which triggers the RF-switch of the AOM driver setup. The signal after optimizing both quantities for all three AOMs is plotted in Fig. 5.8. The total values for the delay including the signal propagation ($\sim 20$ ns) and

the fall and rise times are summarize in the following table.

|  | AOM 1 | AOM 2 | AOM 3 |
|---|---|---|---|
| rise time $t_r$ in ns | 12 | 12 | 14 |
| fall time $t_f$ in ns | 10 | 18 | 12 |
| delay $\tau$ in ns | 71 | 127 | 107 |

It is important to note that in our experiment the delay $\tau$ only occurs once, when we have to react on the arrival of the atom. Afterwards we have a fixed pulse sequence that is only limited by the fall and rise time.

We also measured the minimum pulse length achievable with this setup, which defines the fastest time scale of our experiment. When switching the RF-switch on for a few nanoseconds, without any additional pulse shaping, the pulse width is only limited by the fall and rise time. Figure 5.9 shows the shortest pulses the setup can generate. Further shortening the time the RF-switch is turned on will cause the maximum power of the optical pulse to decreases significantly. The FWHM of 15 ns and 13 ns are in good agreement with the fall and rise time measured in Fig. 5.8. During the time window of $\sim$1 $\mu$s available for state manipulation, the setup can perform a whole sequence of such pulses.

In summary, the AOM setup developed in this work can generate two independent pulses with minimum duration of $\sim$ 20 ns and total delay of $\sim$ 100 ns, which are much shorter than the probing window of about one $\mu$s. In addition, it provides an extinction ratio of more than 110 dB. This is enough to reduce the residual light of the Raman beam below the dark count level of our detectors, when it is turned off.
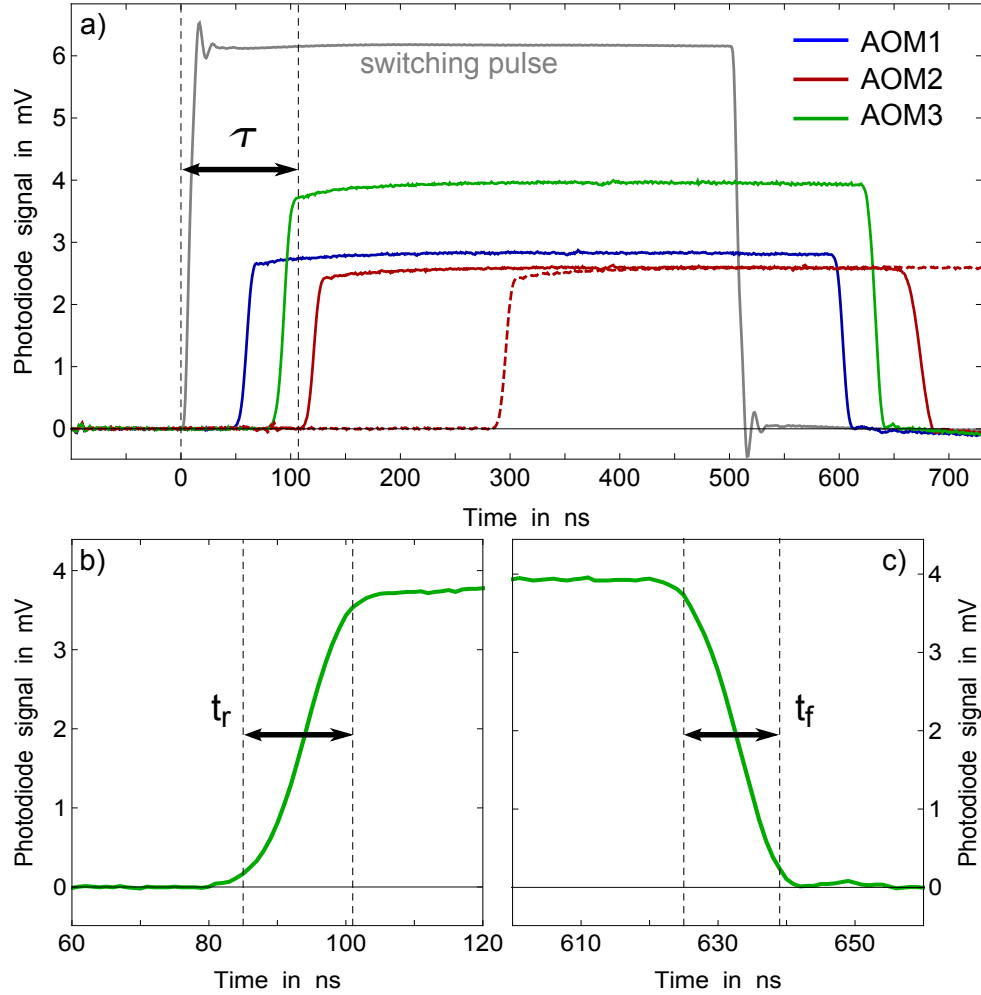
**Figure 5.8:** a) Optical signal detected by a fast photodiode for the different AOMs, when gating the RF-switch of the AOM driver with a pulse corresponding to the gray curve. The delay $\tau$ is defined as the time the light takes to reach its maximum intensity, measured from the moment the switch gets the signal to turn on. In figure a) the delay for AOM3 is marked by the two vertical dashed lines. The different levels of the photo diode signals reflects the diversity in the total efficiencies of the respective paths. To illustrate the impact of the alignment of the piezo and the beam passing the AOM, the dashed red line shows the signal before fine-adjustment and the solid red line after moving the beam about 1 mm closer to the piezo. For better estimation of the the rise and fall time, d) and c) show a magnified view of the AOM3 signal.
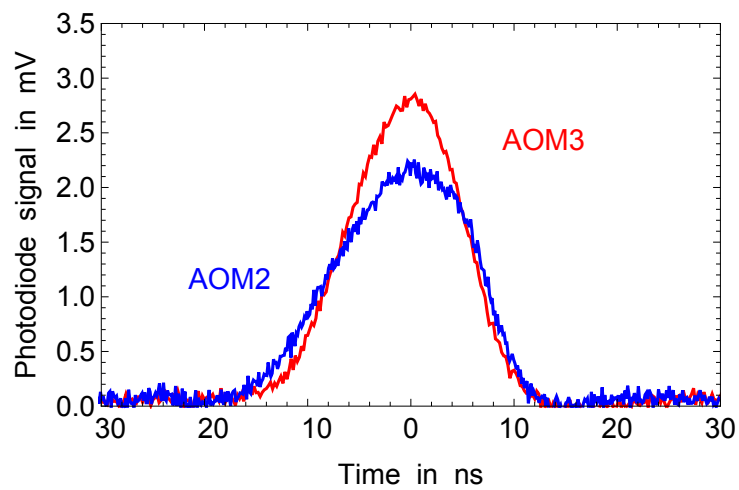
**Figure 5.9:** Shortest optical pulses that can be generated by the AOM setup. The pulses have been aligned with respect to their maxima. The asymmetry is caused by the difference between fall and rise time.

## 5.3 Magnetic bias fields

### 5.3.1 Zeeman splitting

As pointed out in the previous chapter, we are going to drive optical Raman transitions of the atom. Under ideal conditions, it is possible, even for zero magnetic field, to transfer an atom into a certain state just by using the right polarization of the pump light. Due to experimental imperfections or limitations by the applied technique, such as the imperfect circular polarization of the TM resonator modes, this would, however, not sufficiently suppress unwanted transitions in our case. Thus, a small fraction of the atoms would always be excited into an undesired state. Instead of just relying on the polarization, one can also exclude unwanted excitation by shifting the corresponding energy levels far away from the driving frequency. This can be done with external magnetic fields that will cause a so-called Zeeman energy splitting. In order to infer what field strength has to be applied, the following considerations are made.

Each of the hyperfine energy levels contains $2F+1$ magnetic sublevels. In the absence of external magnetic fields, these sublevels are degenerate. However, when an external magnetic field is applied, it couples to the magnetic dipole associated with the atom's angular momentum and the degeneracy is broken. If the energy shift caused by the magnetic field is small compared to the hyperfine splitting, $F$ can be regarded as a good quantum number and, thus, the interaction Hamiltonian becomes

$$\hat{H}_{Zeeman} = \mu_B \, g_F \frac{\vec{F}}{\hbar} \cdot \vec{B} \, , \tag{5.6}$$

where $\mu_B$ is the Bohr magneton, $g_F$ the Lande factor and $\vec{F}$ the total angular momentum operator, which combines the angular momentum of the electron and the nucleus.

For small magnetic fields along the atomic quantization axis $z$, the energy levels split linearly, causing a frequency shift according to

$$\Delta f_{m_F} = \frac{\Delta E_{m_F}}{h} = \frac{\mu_B}{h} g_F \, m_F \, B_z \, , \tag{5.7}$$

called the Zeeman splitting. For the rubidium 85 D$_2$ transition the frequency shifts per magnetic field strength are summarized in Table 5.1.

|  | $5^2S_{1/2}$ | | $5^2P_{3/2}$ | | | |
|---|---|---|---|---|---|---|
| $F$ | 2 | 3 | 1 | 2 | 3 | 4 |
| $\Delta f/(B\,m_F)$ in MHz/G | -0.47 | 0.47 | -1.4 | 0.16 | 0.54 | 0.70 |

**Table 5.1:** Frequency splitting per Gauss for the corresponding hyperfine levels of the rubidium 85 D$_2$ transition [48].

In order to resolve distinct $m_F$ states when addressing them with short laser pulses, Heisenberg's uncertainty principle has to be taken into account: Off-resonant transitions can be driven accidentally as long as the frequency uncertainty is larger than the detuning. In order to prevent this, an energy splitting of

$$\Delta E = h\,\Delta f \gg \frac{\hbar}{2\,\Delta t}\;,\qquad(5.8)$$

is required. The optical Raman transition we want to drive should take place on a timescale of about 100 nanoseconds. The energy difference to the next possible transition of the ground state is $h\Delta f = h\,0.47$ MHz per Gauss. To fulfill Eq. (5.8) we aim for a magnetic field of $B \approx 50$ Gauss, along the quantization axes, such that $\Delta f = 24$ MHz $\gg$ 1 MHz.

## 5.3.2 Magnetic field coils for the CQED experiment

In order to allpy a homogenous field along a certain axis, a pair of coils can be used and should ideally be in Helmholtz configuration. However, this configuration requires the distance between the coils to be the same as the coil radius. Due to the restricted space around the existing experimental setup (see Fig. 3.1), this is impossible to fulfill in our setup. The coil configuration should be able to apply a strong field along the resonator axis, which will be used as quantization axis and is tilted with respect to the $z$ axis by 20°. In addition, we want to compensate any magnetic stray fields. Thus, we require coil pairs for all three dimensions. Due to the geometry of the science chamber, only two pairs of these can be arranged symmetrically with respect to the resonator position. The other two coils have been designed such that an asymmetric number of windings, diameter, and distance to the resonator yields zero field gradient at the position of the resonator. Since we do not intend to open the chamber to place the coils, two of them have to be spooled in vivo, i.e., around flanges of the chamber and not in free space. In order to facilitate the spooling procedure, we have decided to use a wire with large cross section that supports high currents. Thus, only a few windings are necessary for reaching the desired field strength. We have chosen an enameled copper wire with 1x11 mm cross section. In order to keep the multiple layers of wire in place, they are embedded in aluminum mountings. The final coil configuration is depicted in Fig. 5.10 and its specification summarized in the following table:

| Coil | Dimensions / mm | | | | Windings | | Electrical properties @ 20°C | |
|---|---|---|---|---|---|---|---|---|
| | $r_1$ | $r_2$ | $d$ | $L/m$ | $n$ | $N$ | $R$ / $\Omega$ | $P$ @ $I$=60 A |
| $x$ | 85 | 128 | 111 | 20.07 | 1 | 30 | 0.03248 | 117 W |
| $y$ | 60 | 84 | 135 | 14.95 | 2 | 34 | 0.024198 | 87 W |
| $z_{top}$* | 115 | 191 | 222 | 57.68 | 2 | 60 | 0.04668 | 168 W |
| $z_{bottom}$ | 185 | 240 | 189 | 54.74 | 1 | 41 | 0.08858 | 318 W |

*The two separate rows of the winding are connected in parallel, inn order to reduce the resistance.

The parameters $r_1$, $r_2$ and $d$ are specified in Fig. 5.10 and $L$ corresponds to the total wire length, $N$ to the number of windings, which are divided in $n$ columns. Using the cross section and the specific resistance of copper at 20°C, specified as 0.178 $\Omega$mm²/m, the total resistance $R$ and the power load $P$ for $I = 60$ A is calculated.

The resulting field distribution is calculated using the free Wolfram Mathematica add-on Radia [58, 59]. For a maximum current of 60 A, the configuration yields a magnetic field
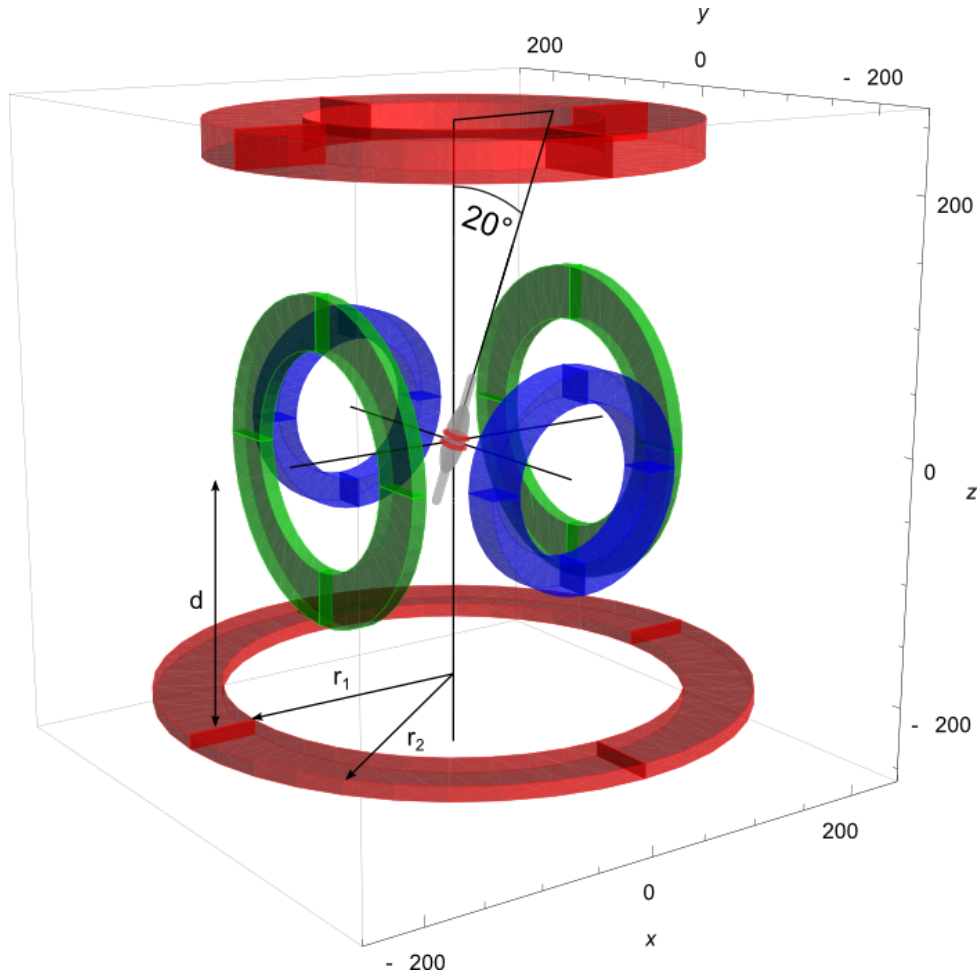


**Figure 5.10:** Sketch of the coil configuration, showing two symmetric coil pairs in $x$ (green) and $y$ (blue) direction, and the asymmetric coils along the $z$-axis (red). The schematic of the resonator has been enlarged for pictorial clarity of the 20° angle between the resonator and the $z$-axis.
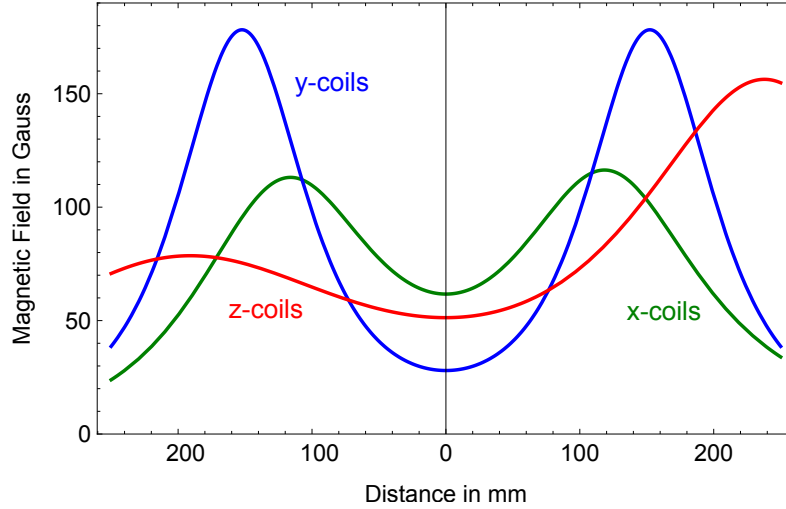
**Figure 5.11:** Magnetic field calculated for the setting shown in Fig. 5.10, along the axial direction of the respective coil pair.

in the respective axial direction at the position of the resonator (0,0,0) of

$$B_x = 61.7 \text{ Gauss} \qquad B_y = 28.0 \text{ Gauss} \qquad B_z = 51.3 \text{ Gauss} \tag{5.9}$$

Even though we are using an asymmetric configuration, all coils show a minimum at the position of the resonator (see Fig. 5.11). This makes the setup less susceptible to small displacements of the coils.

The maximum field should be applied in direction of the resonator, which is tilted by 20° with respect to the $z$-axis in the $xz$-plane. For $I_x = 18.16$ A and $I_z = 60$ A, we obtain the maximum magnetic field which can be applied along the resonator axis of

$$B_{res} = 54.6 \text{ Gauss} \tag{5.10}$$

Due to ongoing measurements, only the coil pair which requires no access to the existing setup has been spooled. For one $y$-coil, the field along the axis has been measured and compared to the calculations (see Fig. 5.12). The good agreement allows us to rule out any unintended short-circuit, caused by damaging of the insulation of the wire during the spooling process.

As soon as possible, the remaining coils will be spooled and integrated into the setup.
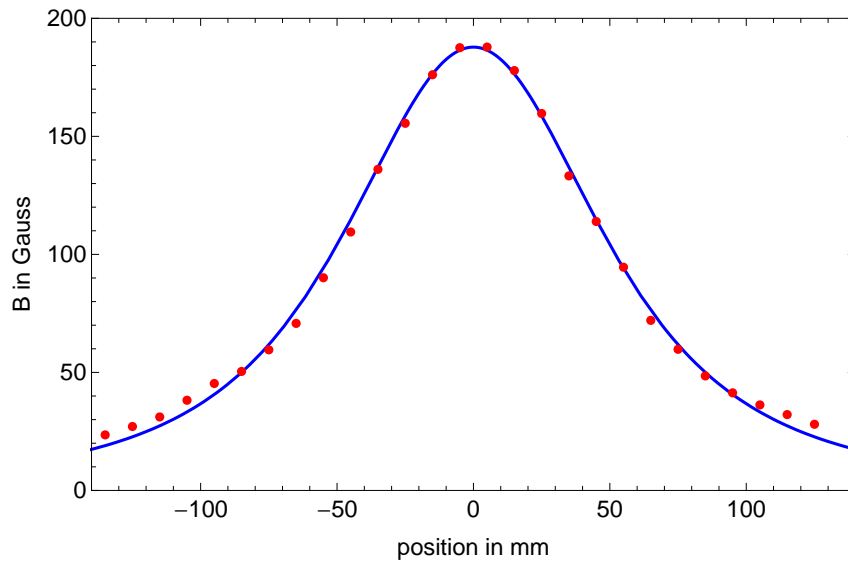
**Figure 5.12:** The measured magnetic field along the coil axis (red points), compared with the prediction based on the calculations (blue line).

# Chapter 6

# Summary and outlook

This thesis describes the steps that were taken toward the realization of a quantum switch for light, based on a bottle microresonator strongly coupled to a single rubidium atom.

In the first experimental part of this thesis, a new atom-resonator interrogation scheme has been developed. It uses the fact that an atom coupled to the resonator mode significantly changes the phase of the light that is transmitted through the coupling fiber. In order to measure this phase shift, we send light through the coupling fiber which has a polarization that does not interact with the resonator. By interference, the phase then becomes measurable as a polarization rotation. We successfully applied this new method for detecting atoms that couple to the evanescent field of our bottle microresonator. This scheme has the advantage that it enhances the measured signal and that it allows us to implement our detection scheme under conditions other than critical coupling. Furthermore, the performance of this new technique as a light switch, operated by a single atom, has been investigated. First measurements have shown that the presence of the atom rotates the polarization of the light in the coupling fiber by up to 65° compared to the case when no atom couples. For this setting, a photon had a 40% probability to still be present after the switching process. The experimental results are in agreement with our theoretical model. This allows us to identify one main constraint of this technique, which is the limited control of the atom-resonator coupling strength due to the movement of the atom. By trapping the atom or by using a mode with higher Q-factor, we expect an even better switching contrast with higher photon survival probability.

While the first part dealt with the realization of a new interrogation scheme which can be used to implement passive switching, the second part of this thesis discusses the required modifications, that have been implemented in the setup in order to enable active switching. For this purpose, the internal atomic state has to be coherently manipulated while the atom is coupled to the resonator mode. This can be achieved by driving optical Raman transitions of the atom via the resonator modes, thereby guaranteeing that we act uniformly on the atoms independently of their positions. To this end, an ultrafast

atomic state manipulation setup, based on acousto-optical modulators, was designed and characterized. This setup is capable of creating light pulses with a delay of approximately 100 ns and a rise and fall time of around 15 ns, which is short compared to the interaction time of the atom with the resonator mode of a few $\mu$s. At the same time, this setup provides an on/off extinction ratio of almost ten orders of magnitude. When turned off, this is enough to reduce the residual light level of the laser beam below the dark count level of our detectors. Additionally, a magnetic field coil configuration has been designed that will provide a strong magnetic bias field which is also essential for coherent state manipulation. Up to now only one coil pair has been spooled for testing purposes. The coils still have to be integrated into the setup.

Future steps will involve the implementation of efficient state manipulation protocols, which should then allow us to prepare arbitrary superpositions of the internal atomic states, where only one of them couples to the resonator and the other one does not. When preparing the atom in an equal superposition state, entanglement between the light field exiting the resonator and the atom can be generated. In order to verify the entanglement, correlation measurements between the internal state of the atom and the state of the light field have to be performed. This will be straightforward using the new polarization measurement setup. The detection of the atom requires an atom state manipulation, followed by an sub-$\mu$s measurement of the fiber transmission. This would be the first realization of deterministic atom-photon entanglement between two initially uncorrelated particles, in the optical domain.

Once this has been realized, the next step would be to extend this scheme to more than one photon in order to deterministically generate small Schrödinger cat states, where the number of entangled particles, i.e., the number of photons, can be controlled. Such states might be used to study decoherence or to perform quantum mechanically enhanced measurement protocols.

# Bibliography

[1] E. M. Purcell. Spontaneous emission probabilities at radio frequencies. *Physical Review*, 69:681–681, 1946.

[2] E. T. Jaynes and F. W. Cummings. Comparison of Quantum and Semiclassical Radioation Theories with Application to the Beam Maser. *Proceedings of the IEEE*, 51:89–109, 1963.

[3] D. Meschede and H. Walther. One-Atom Maser. *Physical Review Letters*, 54:551–554, 1985.

[4] P. R. Berman. *Cavity Quantum Electrodynamics*. Advances in Atomic, Molecular and Optical Physics. Academic Press, New York, 1994.

[5] K. J. Vahala. Optical microcavities. *Nature*, 424(6950):839–46, 2003.

[6] J. McKeever, A. Boca, A. Boozer, J. Buck, and J. Kimble. Experimental realization of a one-atom laser in the regime of strong coupling. *Nature*, 425:268–271, 2003.

[7] J. Volz, R. Gehr, G. Dubois, J. Esteve, and J. Reichel. Measurement of the internal state of a single atom without energy exchange. *Nature*, 475:210–213, 2011.

[8] S. Ritter, C. Nölleke, C. Hahn, A. Reiserer, A. Neuzner, M. Uphoff, M. Mücke, E. Figueroa, J. Bochmann, and G. Rempe. An elementary quantum network of single atoms in optical cavities. *Nature*, 484:195, 2008.

[9] K. Birnbaum, A. Boca, R. Miller, A. Boozer, T Northup, and J. Kimble. Photon blockade in an optical cavity with one trapped atom. *Nature*, 436:87–90, 2005.

[10] W. Chen, K. Beck, R. Bücker, M. Gullans, M. Lukin, H. Tanji-Suzuki, and V. Vuletic. All-Optical Switch and Transistor Gated by One Stored Photon. *Science*, 341:768–770, 2013.

[11] G. Knight, G. Cheung, F. Jacques, and T. Birks. Phase-matched excitation of whispering-gallery-mode resonances by a fiber taper. *Optics Letters*, 22:1129, 1997.

[12] V. Braginsky, M. Gorodetsky, and V. Ilchenko. Quality-factor and nonlinear properties of optical whispering-gallery modes. *Physics Letters A*, 137:393–397, 1989.

[13] D. Armani, T. Kippenberg, S. Spillane, and K. Vahala. Ultra-high-Q toroid microcavity on a chip. *Nature*, 421:925–928, 2003.

[14] M. Pöllinger, D. O'Shea, F. Warken, and A. Rauschenbeutel. Ultrahigh-Q Tunable Whispering-Gallery-Mode Microresonator. *Physical Review Letters*, 103:053901, 2009.

[15] C. Junge, S. Nickel, D. O'Shea, and A. Rauschenbeutel. Bottle microresonator with actively stabilized evanescent coupling. *Optics letters*, 36(17):3488–90, September 2011.

[16] D. O'Shea, A. Rettenmaier, and A. Rauschenbeutel. Active frequency stabilization of an ultra-high Q whispering-gallery-mode microresonator. *Applied Physics B*, 99(4):623–627, April 2010.

[17] D. O'Shea, C. Junge, M. Pöllinger, A. Vogler, and A. Rauschenbeutel. All-optical switching and strong coupling using tunable whispering-gallery-mode microresonators. *Applied Physics B*, 105(1):129–148, 2011.

[18] C. Junge, D. O'Shea, J. Volz, and A. Rauschenbeutel. Strong Coupling between Single Atoms and Nontransversal Photons. *Physical Review Letters*, 110(21):213604, 2013.

[19] D. O'Shea, C. Junge, J. Volz, and A. Rauschenbeutel. Fiber-optical switch controlled by a single atom. *arXive*, 1306.1357, 2013.

[20] L. Davidovich, A. Maali, M. Brune, J.M. Raimond, and S. Haroche. Quantum switches and nonlocal microwave fields. *Physical Review Letters*, 71(15):2360–2363, October 1993.

[21] E. Schrödinger. Die gegenwärtige Situation in der Quantenmechanik. *Die Naturwissenschaften*, 23(48), 1935.

[22] C. Monroe, D. M. Meekhof, B. E. King, and D. J. Wineland. A "Schrödinger Cat" Superposition State of an Atom. *Science*, 272:1131–1136, 1996.

[23] E. Hagley, X. Maître, G. Nogues, C. Wunderlich, M. Brune, J. M. Raimond, and S. Haroche. Generation of Einstein-Podolsky-Rosen Pairs of Atoms. *Physical Review Letters*, 99:1–5, 1997.

[24] G. Kirchmair, B. Vlastakis, Z. Leghtas, S. E. Nigg, H. Paik, E. Ginossar, M. Mirrahimi, L. Frunzio, S. M. Girvin, and R. J. Schoelkopf. Observation of quantum state collapse and revival due to the single-photon Kerr effect. *Nature*, 495:205–209, 2013.

[25] S. Chu, B. Little, B. Pan, T. Kaneko, S. Sato, and Y. Kokubun. Filter synthesis for periodically coupled microring resonators. *IEEE Photonics Technology Letters*, 11:691, 1999.

[26] F. Vollmer, D. Braun, A. Libchaber, M. Khoshsima, I. Teraoka, and S. Arnold. Protein detection by optical shift of a resonant microcavity . *Appl. Phys. Lett.*, 80:4057–4059, 2002.

[27] C. J. Hood, T. W. Lynn, A. C. Doherty, A. S. Parkins, and Kimble H. J. The Atom-Cavity Microscope: Single Atoms Bound in Orbit by Single Photons. *Science*, 287:1447–1453, 2000.

[28] K. Srinivasan, P. E. Barclay, O. Painter, J. Chen, A. Y. Cho, and C. Gmachl. Experimental demonstration of a high quality factor photonic crystal microcavity . *Appl. Phys. Lett.*, 83:1915, 2002.

[29] Y. Louyer, D. Meschede, and A. Rauschenbeutel. Tunable whispering-gallery-mode resonators for cavity quantum electrodynamics. *Physical Review A*, 72(3):031801, 2005.

[30] M. Pöllinger. *Bottle microresonators for applications in quantum optics and all-optical signal processing*. PhD thesis, Johannes Gutenberg Universität, Mainz, Germany, 2010.

[31] M. Cai, O. Painter, and K. Vahala. Observation of critical coupling in a fiber taper to a silica-microsphere whispering-gallery mode system. *Physical Review Letters*, (85):74, 2000.

[32] S. Spillane, T. Kippenberg, O. Painter, and K. Vahala. Ideality in a Fiber-Taper-Coupled Microresonator System for Application to Cavity Quantum Electrodynamics. *Physical Review Letters*, 91:043902, 2003.

[33] D. Armani, B. Min, A. Martin, and K. Vahala. Electrical thermo-optic tuning of ultrahigh-Q microtoroid resonators. *Applied Physics Letters*, 85:5439–5441, 2004.

[34] W. v. Klitzing, V. Long, R. and. Ilchenko, J. Hare, and V. Lefevre-Seguin. Frequency tuning of the whispering-gallery modes of silica microspheres for cavity quantum electrodynamics and spectroscopy. *Optics Letters*, 26:166–168, 2001.

[35] D. Axelrod, T. P. Burghardt, and N. L. Thompson. Total Internal Reflection Fluorescence. *Annual Review of Biophysics and Bioengineering*, 13:247–268, 1984.

[36] C. Gerry and P. Knight. *Introductory Quantum Optics*. Cambridge University Press, 2005.

[37] H. J. Carmichael. *An Open Systems Approach to Quantum Optics*. Springer-Verlag, 1991.

[38] D. Alton, N. Stern, T. Aoki, H. Lee, E. Ostby, K. Vahala, and J. Kimble. Strong interactions of single atoms and photons near a dielectric boundary. *Nature Physics*, 5(12):1–7, 2010.

[39] B. Dayan, S. Parkins, T. Aoki, E. Ostby, K. Vahala, and J. Kimble. A photon turnstile dynamically regulated by one atom. *Science*, 319(5866):1062–5, February 2008.

[40] C. Hauswald. *Aufbau und Charakterisierung eines Atom-Springbrunnens für ein Resonator-QED-Experiment mit Flüstergaleriemoden-Mikroresonatoren*. Master's thesis, Johannes Gutenberg Universität, Mainz, Germany, 2010.

[41] V. Giovannetti, S. Lloyd, and L. Maccone. Quantum-enhanced measurements: beating the standard quantum limit. *Science*, 306:1330, 2004.

[42] J. Kimble. The quantum internet. *Nature*, 453:1023–1030, 2008.

[43] J. S. Bell. On the Einstein Podolsky Rosen Paradox. *Physics*, 1:196–200, 1964.

[44] J. Volz, M. Weber, D. Schlenk, W. Rosenfeld, J. Vrana, S. Saucke, C. Kurtsiefer, and H. Weinfurter. Observation of Entanglement of a Single Photon with a Trapped Atom. *Physical Review Letters*, 96:030404, 2006.

[45] B. B. Blinov, D. L. Moehring, L.-M. Duan, and C. Monroe. Observation of entanglement between a single trapped atom and a single photon. *Nature*, 428:153–157, 2004.

[46] D. O'Shea. *Cavity QED experiments with a whispering-gallery-mode bottle resonator*. PhD thesis, Vienna University of Technology, 2013.

[47] K. Friebe. *Strong Coupling of Single Atoms to a Whispering-Gallery-Mode Resonator of Ultrahigh Quality*. Master's thesis, Johannes Gutenberg Universität, Mainz, Germany, 2011.

[48] D. A. Steck. Rubidium 85 D Line Data, University of Oregon, `http://steck.us/alkalidata/rubidium85numbers.pdf`, July 2013.

[49] T. Peyronel, O. Firstenberg, Q. Liang, A. Hofferberth, S.and Gorshkov, T. Pohl, M. Lukin, and V. Vuletic. Quantum nonlinear optics with single photons enabled by strongly interacting atoms. *Nature*, 488:57–60, 2012.

[50] D. Reitz, C. Sayrin, R. Mitsch, P. Schneeweiss, and A. Rauschenbeutel. Coherence Properties of Nanofiber-Trapped Cesium Atoms. *Physical Review Letters*, 110(24):243603, June 2013.

[51] C. Ospelkaus, C. Langer, J. Amini, K. Brown, D. Leibfried, and D. Wineland. Trapped-Ion Quantum Logic Gates Based on Oscillating Magnetic Fields. *Physical Review Letters*, 101(9):090502, August 2008.

[52] C. Ospelkaus, U. Warring, Y. Colombe, K. R. Brown, J. M. Amini, D. Leibfried, and D. J. Wineland. Microwave quantum logic gates for trapped ions. *Nature*, 476(7359):181–4, August 2011.

[53] K. Bergmann, H. Theuer, and B. W. Shore. Coherent population transfer among quantum states of atoms and molecules. *Review of Modern Physics*, 70:1003–1025, 1998.

[54] J. R. Kuklinski, U. Gaubatz, F. T. Hioe, and K. Bergmann. Adiabatic population transfer in a three-level system driven by delayed laser pulses. *Physical Review A*, 40:11, 1989.

[55] P. W. Barber and J. Z. Hill. *Light Scattering by Particles: Computational Methods*. World Scientific, 1990.

[56] E. A. Donley, T. P. Heavner, F. Levi, M. O. Tataw, and S. R. Jefferts. Double-pass acousto-optic modulator system. *Review of Scientific Instruments*, 76(6):063112, 2005.

[57] B. E. A. Saheh and M. C. Teich. *Fundamentals of Photonics*. Wiley, 2007.

[58] Radia, Scientific Software Developed by the ID Group at ESRF. `http://www.esrf.eu/Accelerators/Groups/InsertionDevices/Software/Radia`, July 2013.

[59] C. Chubar, P. Elleaume, and J. Chavanne. A 3D Magnetostatics Computer Code for Insertion Devices. *J. Synchrotron Rad.*, 5:481–484, 1998.

# Acknowledgements

Ich bedanke mich bei allen, die mich während meines Studiums begleitet und unterstützt haben.

Mein Dank gilt insbesondere Arno Rauschenbeutel, der mir die Gelegenheit gegeben hat meine Diplomarbeit an diesem Experiment zu schreiben. Ich danke auch meinen Kollegen des CQED-Experiments, Christian und Jürgen, ohne deren hervorragende Betreuung diese Arbeit nicht zustande gekommen wäre. Meinem Tischnachbarn Bernhard, der mir bei elektrotechnischen Problemen immer zur Seite stand, bin ich auch zu Dank verpflichtet. Danke auch an alle anderen Rauschis für das hervorragende Gruppenklima.

Darüber hinaus möchte ich noch meinen Studienkollegen (in alphabetischer Reihenfolge: Ali, Berni, Daniel, Lorenz, Lukas, Martin, Tobi und Wolfi) dafür danken, die Studienzeit zu einer sowohl äußerst unterhaltsamen als auch erfolgreichen Zeit gemacht zu haben. Ebenso danke ich meinen Freunden für die schöne außeruniversitäre Zeit. Besonders großer Dank an Catherina für ihre Hilfe und ihr Verständnis in den letzten Wochen und die schönen gemeinsamen Jahre.

Schließlich bedanke ich mich noch bei meiner Familie, ganz besonders bei meinen Eltern, die mir durch ihre Unterstützung das Studium ermöglicht haben.